

Mechanistic insights into the large-scale dynamics underlying different brain states

Beatrice M. Jobst

TESI DOCTORAL UPF / 2018

Director de la tesi

Prof. Dr. Gustavo Deco,
Department of Information and Communication Technologies





To Tommaso, Serena and Chiara.



Acknowledgements

First of all I would like to thank my supervisor and mentor, Gustavo Deco. Thank you for your guidance, your help whenever needed, your endless support, your open-mindedness, thank you for all the freedom you gave me during my PhD and the possibilities you opened up for me to work with really great data. You are really the best mentor a PhD student could hope for, I will never forget this wonderful period of my life which you made possible, thank you for that!

An enormous thank you also goes to all my wonderful colleagues and co-workers I got to know during my years at the UPF: a special thanks to the post-docs who co-supervised me, who I worked with, who taught me how to do science and who invested a valuable amount of their time in guiding and helping me: Rikkert Hindriks, Adrián Ponce-Alvarez, Selen Atasoy, Matthieu Gilson, Gorka Zamora, Ana Sanjuán, Gerald Hahn, Andrea Insabato, Mario Pannunzi, Raphael Kaplan and Mohit Adhikari, without all of you this work would have never been possible. But I also need to thank my co-PhD colleagues, who I had lots of discussions with, who all helped me at some point and who, most importantly, were in the same situation as I was and were thus the only persons who you could truly talk about the problems you were having: Katharina Glomb, Tristan Nakagawa, Ruggero Bettinardi, Victor Saenger, Murat Demirtaş, Vicente Pallarés, and Josefina Cruzat, thank you all.

I furthermore would like to thank my external collaborators Morten Kringelbach, Enzo Tagliazucchi, Helmut Laufs and Robin Carhart-Harris, who let me use their excellent fMRI data and who gave me valuable inputs on my work.

Next, I would like to thank the people who have made my stay at the Shanghai Computational and Cognitive Neuroscience Summer School such a great experience, which I will remember all my life: thank you Eric Dewitt, John Murray and Michael Breakspear, for your fruitful discussions and help.

At this point my gratitude also goes to the administrative staff at the CBC: Florencia, Xavi, Silvia and Cristina and also the staff from the DTIC secretary's office: Lydia, Jana and Vanessa. You have all made my life as a PhD student so much easier!

During my time as a doctoral student I have made some wonderful friends here in Barcelona, who have become my best friends during these last years: thank you Alice Del Genovese, Itziar Ramirez, Roberta Coda, Ruggero Bettinardi, Victor Saenger, Andrea Insabato, Vicente Pallarés, Josefina Cruzat and also Patricio Donnelly, who I got to know only during a short period of time, but who became a great friend during his stay.

A special thanks also goes to my friend and ex-colleague Markus Waser, without whom I would probably not be where I am today. An exceptional thank you goes as well to my best friend from home, Christine Hansmann, thank you for all your mental support and your eternal phone calls during my whole PhD and my pregnancies.

A very important thank you goes to both of my parents, who have supported me mentally and financially throughout my whole life and especially during all of my studies, without both of you all of this would have never been possible. You have always believed in me no matter what and you have supported me in all my decisions, thank you for that. I would like to thank my father, without whom I would have probably never took on the adventure of studying mathematics in the first place and would have therefore never found my way of interest in computational neuroscience; but also my mother, who would always talk to me and lend me her ear, whatever problem I had, and who came several times to visit me in order to help me out and take care of my daughter when I needed to work. I also want to thank my whole family who has always been there for me, especially my cousins Carolin and Sarah who came to babysit in order for me to be able to work. An exceptional thank you also goes to both my parents in law, who could always come to give us a hand when we and especially I needed them, without their help it would have been impossible to finish this PhD. Thanks also to my fantastic sister in law and her family

who we could always count on.

The most special thank you of all goes to my husband, Tommaso, who became my husband during my PhD studies, who I had my beautiful daughter Serena Alice during my PhD studies with, and whom I am expecting another baby girl with right now. All of this would not have been possible without you. You were always there for me when I needed you, I could always count on you lending me an ear when things almost got too rough for me, you would always be my calm constant, you helped me in any possible way to take off as much work as possible of my shoulders, so that I could finish this PhD, even under the tough circumstances. You know I love you, always have and always will, thank you for being you. I also need to thank my little daughter Serena at this point for being such a nice, well-behaved and quite easy-to-handle baby, who would allow me to work next to her even when she was only a few months old. Only this made it possible for me to continue.

I want to thank all of you, all the people in my life, who I have met and who I have shared parts of my life with, you all shaped me into the person I am today, a person who could do such a crazy thing as to finish a PhD with a little baby and another one on the way.



Abstract

Brain activity during rest exhibits a robust intrinsic spatio-temporal structure characterized by correlated patterns of neural activity. The study of the brain in altered states of vigilance or drug-induced brain states has revealed a number of local and global alterations of this activity and changes in the spatio-temporal correlation patterns. Yet, we are still missing a mechanistic explanation of the dynamics underlying these experimentally observed phenomena. In this thesis we will use whole-brain computational modeling to try to elucidate the dynamical processes governing these distinct brain states. We will show how models of whole-brain activity and dynamical alterations thereof on a local level can be applied to efficiently dissociate between different brain states by their dynamical properties and how they therefore provide a mechanistic characterization of each state. We will demonstrate that one unified framework can account for an effective description and identification of several entirely distinct brain states.

Resumen

La actividad cerebral en reposo presenta una estructura espacio-temporal intrínseca robusta caracterizada por patrones de actividad neuronal correlacionados. El estudio del cerebro en estados alterados de conciencia o estados bajo influencia de drogas ha revelado alteraciones locales y globales de esta actividad así como cambios en los patrones de correlación. Sin embargo, los mecanismos de la dinámica subyacente no han sido revelados del todo. En esta disertación se aplicarán modelos computacionales de actividad cerebral a gran escala para intentar a esclarecer los procesos dinámicos que dominan dichos estados cerebrales. Se mostrará cómo las alteraciones de las dinámicas locales pueden ser aplicadas para diferenciar estados cerebrales distintos así como para proporcionar una caracterización mecánica de cada estado. Finalmente, se revelará cómo un único marco teórico puede ser utilizado para describir e identificar de manera efectiva estados cerebrales completamente diferentes.

Preface

Understanding the functioning of the brain has intrigued numerous thinkers, philosophers and scientists throughout the past few thousand years. The study of the brain and the nervous system requires a multi-disciplinary approach, which is why originally researchers from different fields, such as philosophy, psychology, medicine, biology, chemistry and physics, dedicated themselves to the understanding of brain function. It was not until recently in the 20th century that neuroscience became a unified academic discipline. In the past decades neuroscientific research has revealed a lot about brain function and the structure it is based on extending from a molecular point of view to a whole-brain level. Albeit the enormous amount of information we have at hand nowadays, there still remains much to be discovered. Recent advances in technology have had a huge impact on the better understanding of brain functioning, such as measuring the nervous system's electrical activity or advanced functional neuroimaging methods like magnetoencephalography (MEG) or functional magnetic resonance imaging (fMRI). With these techniques we have gained a huge amount of valuable knowledge especially on meso- and macroscopic brain functioning and organization. One of the most fascinating discoveries of the last decades has probably been the finding that the brain manifests correlated activity patterns even in the absence of any kind of task or stimulus – a feature which was formerly thought to be inherent to task activated brain activity only. This discovery changed the rationale about how the brain works as a complex system entirely. Perhaps an even more fascinating question to investigate though is, what happens in the brain during altered states of consciousness or vigilance, distinct from the before

mentioned resting-state. A lot of research has been performed in recent years trying to answer this question mainly focusing on experimentally identifiable changes such as alterations in neuronal activity or correlation patterns. Yet, there still exist no clear mechanistic explanations of these experimental observations. To understand the underlying processes causing these specific alterations from a dynamical point of view, one has to go beyond the pure analysis of experimental data. Computational models of brain activity are one way of exploring the dynamical principles that govern local and global brain function and changes thereof in different brain states. This dissertation is dedicated to the deeper understanding of the mechanisms and dynamical processes underlying the changes in neural activity and functional correlation patterns in distinct states of the brain.

In Chapter 1 we will introduce the characteristics of the brain states we will work with in this thesis, namely resting-state, states of reduced vigilance such as sleep and anesthesia and the psychedelic brain state. We will discuss previous findings in these different fields and introduce computational brain models as imperative for the deeper understanding of the experimental results. To this aim, we will introduce a specific whole-brain computational model which will be used as a global framework to explore the underlying brain dynamics in different states throughout the whole thesis. Additionally we will talk about the characterization of global brain dynamics through external brain perturbation, an approach we will focus on in Chapters 3 and 4.

Chapters 2 and 3 of this thesis are dedicated to elucidating the underlying mechanisms governing brain activity during deep sleep, where we will show how computational brain modeling can provide new insights into the global differences between a state of low vigilance and wakeful rest from a dynamical systems point of view. In Chapter 3 we will introduce a novel methodology for investigating the dynamical stability and complexity of distinct brain states by applying a perturbative approach based on a whole-brain computational model simulating external perturbations of local brain activity.

This concept will be further applied to elucidate the inherent processes and mechanisms dominating the psychedelic brain state after the intake of hallucinogenic drugs, which will be explored in detail in Chapter 4.

In Chapter 5 we will finally discuss all the results obtained in the previous chapters in detail and try to put them into a global unifying perspective. We will furthermore consider the limitations of the studies presented in this dissertation, but as well underline the contributions to the understanding of global and local brain function in different brain states obtained through the work in this thesis.



Contents

Acknowledgements	v
Abstract	ix
Resumen	x
Preface	xi
List of Figures	xix
List of Tables	xxi
1 Introduction	1
1.1 The brain at rest	2
1.2 Deep sleep and anesthesia	7
1.3 The psychedelic state.....	14
1.4 The need for computational brain models	20
1.4.1 The Kuramoto model of coupled phase oscillators..	23
1.4.2 The Hopf model	24
1.5 Perturbative studies on the brain	27
2 The underlying brain dynamics of slow-wave sleep	33
2.1 Introduction.....	34
2.2 Methods	36
2.2.1 Experimental data.....	36
2.2.1.1 Participants	36

2.2.1.2	fMRI and EEG data collection	37
2.2.1.3	fMRI pre-processing	37
2.2.2	DTI data collection and processing	38
2.2.3	Construction of surrogate data	39
2.2.4	Group averaged functional connectivity matrices ...	40
2.2.5	Brain state classification with Gaussian classifier ...	40
2.2.6	Phase synchrony and metastability	42
2.2.7	Hopf computational whole-brain model	43
2.2.8	Model fitting	43
2.2.9	Effective connectivity analysis	45
2.2.10	Effective connectivity model validation	47
2.3	Results	48
2.3.1	Lowering of functional connectivity, phase syn- chrony and metastability in deep sleep	48
2.3.2	Classification of consciousness state with Gaussian classifier	49
2.3.3	Shift of the dynamic working point during sleep ...	49
2.3.4	Lowering of the effective connectivity during sleep .	51
2.3.5	Validation of the effective connectivity modeling procedure	53
2.3.6	Theoretical model response to external stimulus ...	55
2.4	Discussion	58
2.5	Conclusion	63
3	Perturbation of whole-brain dynamics in different brain states	65
3.1	Introduction	66
3.2	Methods	69
3.2.1	Overview of perturbative approach	69
3.2.2	Experimental data	69
3.2.2.1	Frankfurt dataset	69
3.2.2.2	Liège dataset	69
3.2.3	Structural connectivity	72
3.2.4	Group averaged functional connectivity matrices ...	72
3.2.5	Whole-brain computational model	73
3.2.6	Fitting the model to empirical data	73
3.2.7	Offline perturbation protocols	74
3.2.8	Integration over time	76
3.2.9	Perturbative Integration Latency Index	77
3.3	Results	79

3.3.1	Optimal working point	79
3.3.2	Perturbation of whole-brain dynamics	79
3.3.3	Higher latencies after perturbation during wake- fulness	80
3.4	Discussion	82
3.5	Conclusion	85
4	Characterizing the psychedelic state through pertur- bation of whole-brain dynamics	87
4.1	Introduction	88
4.2	Methods	91
4.2.1	fMRI data	91
4.2.2	Anatomical connectivity	92
4.2.3	Hopf computational whole-brain model	92
4.2.4	Functional connectivity estimation	92
4.2.5	Fitting the model to experimental data	93
4.2.6	Model perturbation protocols	93
4.2.7	Integration measure	94
4.2.8	Perturbative Integration Latency Index (PILI)	94
4.2.9	Region-wise and resting-state network analysis	95
4.2.10	Hierarchy index	97
4.3	Results	98
4.3.1	Functional connectivity and optimal working point	98
4.3.2	Global differences in integration	100
4.3.3	Global and local differences in Perturbative Inte- gration Latency Index	101
4.3.4	Relationship of PILI to resting-state networks	102
4.3.5	Increased hierarchy in LSD condition	105
4.4	Discussion	107
4.5	Conclusion	112
5	General Discussion	113
5.1	Study limitations and general research contributions	119
5.2	Conclusion	122
A	Appendix Chapter 2	123
B	Appendix Chapter 3	127
C	Appendix Chapter 4	131

Bibliography

137

List of Figures

1.1	Spontaneous fluctuations resemble task activity.....	3
1.2	Resting-state functional correlations between a seed region in the posterior cingulate cortex (PCC) and all other voxels in the brain (single subject).	5
1.3	Comparison of the DMN in different mammals (rats, monkeys and humans).	6
1.4	Major resting-state networks (RSNs).	7
1.5	Whole-brain functional connectivity patterns for awake and all 3 NREM sleep stages.	9
1.6	Increased similarity between functional and anatomical connectivity in deep sleep.	10
1.7	RSN topographies are preserved during NREM sleep.	11
1.8	Functional connectivity for different vigilance states.	13
1.9	Coherent spontaneous BOLD fluctuations resemble task-evoked responses and anatomical connectivity.	13
1.10	Maps of whole-brain cerebral blood flow in LSD and Placebo conditions.	16
1.11	LSD provoked changes in resting-state network integrity, cerebral blood flow, signal variance and segregation.	17
1.12	FC increases under LSD.....	18
1.13	Between-network FC increases under LSD.	19
1.14	Construction of the Hopf whole-brain model.	26
2.1	Whole-brain model linking anatomical connections and FC. ..	44
2.2	Data Analysis.	50

2.3	Whole-brain model parameter space exploration and fitting. . .	52
2.4	Effective connectivity in awake and sleep.	54
2.5	Effective connectivity procedure validation.	55
2.6	Single node response to external stimulus for two different dynamic working regimes.	57
3.1	Procedure for computing the Perturbative Integration La- tency Index (PILI).	70
3.2	Adjusting the Hopf whole-brain model to the basal brain ac- tivity of wakefulness and deep sleep.	75
3.3	Response to perturbation in silico for wakefulness and deep sleep.	78
3.4	Slower recoveries in the Awake model compared to the Sleep model following systematic perturbation reveal critical slow- ing down of the network dynamics.	81
4.1	Calculation of the Perturbative Integration Latency Index (PILI).	96
4.2	Empirical functional connectivity and model fitting.	99
4.3	Mean integration.	101
4.4	PILI – Node level analysis.	103
4.5	PILI – RSN analysis.	105
4.6	Hierarchy.	106
A.1	Subject-specific SC analysis.	124
A.2	Subject level data analysis.	125
A.3	Global FC fitting with same node strength.	126
B.1	Distribution of peak frequencies in the band-passed BOLD signals in all brain areas during wakefulness and deep sleep. . .	128
B.2	Distribution of peak frequencies in the band-passed BOLD signals in all brain areas during wakefulness and deep sleep. . .	129
C.1	PILI – Node level analysis for noise protocol.	132

List of Tables

4.1	Node level PILI differences.....	104
C.1	Node level PILI differences – synchronization protocol.	133
C.2	Node level PILI differences – noise protocol.	135



Introduction – The brain in different states

Whether we are performing a specific task, or whether we are resting and thus not doing anything in particular, whether we are asleep or even anesthetized, or whether we are under the influence of intoxicating substances such as alcohol or drugs, our brain is always active. It is always active, no matter what state the brain is in. What will change though, are the spatio-temporal patterns of brain activity and the local or global dynamics underlying this activity.

Since the beginning of the recording of electrical brain activity introduced by Richard Caton in 1875 and later made famous with the electroencephalogram (EEG) by Hans Berger in 1929 (Haas, 2003), it has been demonstrated many times that the brain is continuously active, producing a rich pattern of spontaneous activity (Biswal et al., 1995; Arieli et al., 1996; Raichle et al., 2001; Laufs et al., 2003; Leopold et al., 2003; de Pasquale et al., 2010; Brookes et al., 2011), which changes depending on the state the brain is in (Alkire and Miller, 2005; Vincent et al., 2007; Horowitz et al., 2009; Sämann et al., 2011; Boly et al., 2012; Carhart-Harris et al., 2012; Tagliazucchi et al., 2012a; Carhart-Harris et al., 2014; Tagliazucchi and Laufs, 2014; Tagliazucchi et al., 2014; Barttfeld et al., 2015; Carhart-Harris et al., 2016a,b; Tagliazucchi et al., 2016c). These behaviorally different brain states must also reflect distinct underlying dynamics shaping the observed changes in measurable brain activity (Hill and Tononi, 2005; Molae-Ardekani et al., 2007; Esser et al., 2009; Deco et al., 2011; Cabral

et al., 2014a; Ching and Brown, 2014; Atasoy et al., 2017b). The question is though, how can these dynamical differences be characterized? How can we access them? The mere observation of empirically observable alterations in brain activity in different states does not answer the question of what is causing these changes.

In this thesis we will present a collection of studies aiming at understanding the underlying mechanisms and whole-brain dynamics generating these known modifications in the spatio-temporal patterns of brain activity. We will show how computational whole-brain modeling can be applied to explore these underlying dynamics and provide possible mechanistic explanations of what is causing the activity patterns to change. We will furthermore introduce a novel framework of *in silico* model perturbation of whole-brain dynamics which gives us important new insights into the characterization of different brain states merely identified by their dynamical changes.

Before explaining these studies in detail, we will first review the most important concepts relevant for understanding the various approaches applied in each of the main chapters.

1.1 The brain at rest

The classic focus of cognitive neuroscience studies has for a long time been the measurement and localization of brain activity while performing a certain task (Friston et al., 1998; Cabeza and Nyberg, 2000). The study of the spontaneous activity of the brain while it is at rest, i.e. not performing any specific task, not obtaining any visual inputs and not being asleep, has gained importance only during the past two decades. In 1995 Biswal et al. (Biswal et al., 1995) laid the ground for the – what could almost be called – avalanche of studies on the resting-state of the brain that followed (Raichle et al., 2001; Greicius et al., 2003; Fox et al., 2005; Damoiseaux et al., 2006; Fox and Raichle, 2007; Mantini et al., 2007; Greicius et al., 2009; Honey et al., 2009; Van Den Heuvel et al., 2009; Brookes et al., 2011), by showing that the specific brain areas activated during a certain task also exhibited correlated fMRI BOLD (blood-oxygen-level dependent) activity while not performing any task, i.e. during rest (Biswal et al., 1995) (see Fig. 1.1). With this finding the previously practiced approach

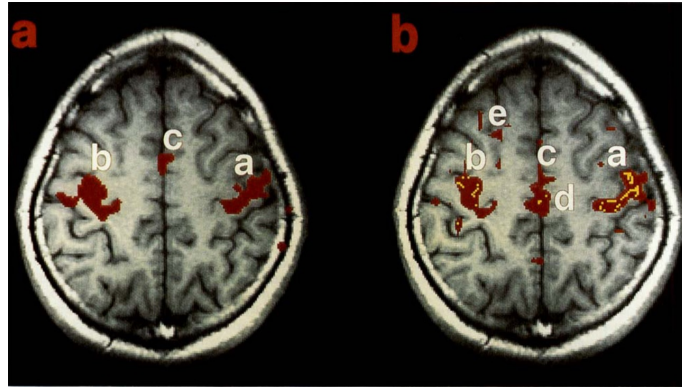


Figure 1.1: **Spontaneous fluctuations resemble task activity.** Left: Activated brain areas in response to a bilateral finger movement task. Right: Spontaneous BOLD fluctuations during rest. a, b and c were the statistically similar regions in both brain states, whereas d and e were present only during rest. Figure reproduced from Biswal et al. (1995).

to take the resting activity as baseline activity or background noise when analyzing task-induced activations needed to be changed radically (Raichle, 2009b). The observed activity during rest reflects the brain's global intrinsic characteristics (Deco et al., 2011) by not being externally driven or influenced by any kind of task and makes therefore an ideal candidate to study large-scale brain mechanisms.

The vast majority of resting-state studies in humans have been and are still performed using non-invasive recording techniques such as fMRI (Raichle et al., 2001; Fox et al., 2005; Greicius et al., 2009), MEG (Brookes et al., 2011) and EEG (Mantini et al., 2007). Due to its excellent spatial resolution and the fact that it primarily represents the activity of the neural populations of the brain region where it is measured from (Rees et al., 2000; Logothetis et al., 2001; Attwell and Iadecola, 2002; Shmuel and Leopold, 2008; Schölvinck et al., 2010), fMRI represents an optimal technique for studying global and local brain activity and especially correlations thereof. This, on the other hand, is not the case for MEG or EEG, where source modeling needs to be applied to localize the origins of the measured brain activity (Baillet and Garnero, 1997; Wolters et al., 2004; Grech et al., 2008).

One of the main tools to investigate resting-state brain dynamics is deter-

mining the functional connectivity (FC) between distinct brain regions. FC is defined as the statistical dependence between the time courses of brain signals originating from different voxels or brain areas. This can be determined by Pearson correlations, phase synchronizations, covariance, mutual information or causality measures (Friston et al., 1993). This definition is based on the assumption that if two separate brain regions show correlated activity it is very likely that they integrate information together and are thus participating in the same function or process. This makes it possible to construct whole-brain networks, also called functional connectomes, and analyze their topological properties in order to understand connections between distinct brain areas not only anatomically but also functionally (Bullmore and Sporns, 2009). For these types of analyses it is convenient to apply graph theoretical and complex networks tools, representing the brain architecture as vertices and edges (Sporns et al., 2004; Rubinov and Sporns, 2010). These methodologies yield important insights about how distributed networks integrate information in order to be able to execute complex cognitive functions and processes and furthermore how these properties change under different brain states or diseases (Sporns, 2013).

One of the main findings in resting-state fMRI research is the spatial organization of the BOLD signal fluctuations into large-scale networks. These networks were termed resting-state networks (RSNs) (Fox et al., 2005; Damoiseaux et al., 2006) and consist of groups of brain regions, which display correlated spontaneous activity, i.e. which are functionally connected, during rest. The organization of the brain into distinct networks allows for the functional integration of spatially segregated information making it possible to perceive external stimuli, respond to cognitive demands and produce coordinated movement (Tononi et al., 1992, 1994; Jirsa and Kelso, 2000; Sporns, 2000). One of the most striking properties of RSNs is the observation that specific tasks evoke brain activity patterns which resemble the RSNs (De Luca et al., 2005; Cole et al., 2014; Glasser et al., 2016), thus making it possible to study the same connectivity patterns without having to apply costly task protocols. Furthermore it has been observed by Fox et al. (2005) that sets of brain areas which showed correlated activity patterns between each other, anticorrelated with other networks (see Fig. 1.2).

This finding paved the way for the discovery of several functionally relevant RSNs measured principally with fMRI (Fox et al., 2005; Damoiseaux et al., 2006; De Luca et al., 2006; Van Den Heuvel et al., 2009), but also MEG/EEG (Laufs et al., 2003; Mantini et al., 2007; de Pasquale et al., 2010; Brookes

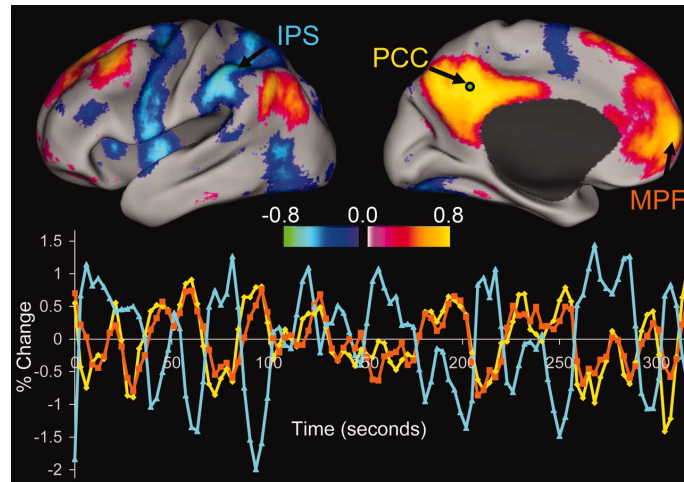


Figure 1.2: **Resting-state functional correlations between a seed region in the posterior cingulate cortex (PCC) and all other voxels in the brain (single subject).** Both positive and negative correlations can be observed in the upper panel (threshold at $R = 0.3$). In the lower panel the BOLD time courses of the seed region (PCC, yellow), of a positively correlated region in the medial prefrontal cortex (MPF, orange) and a negatively correlated region in the intraparietal sulcus (IPS, blue) is shown. Figure reproduced from Fox et al. (2005).

et al., 2011). The most famous RSN is probably the default mode network (DMN), a set of regions comprising the bilateral medial and lateral parietal cortices, the bilateral medial prefrontal cortex, and the bilateral medial and lateral temporal cortices, which show correlated activity between each other during rest in the absence of any task, which is why this network is also called task-negative network (Raichle et al., 2001; Raichle, 2015). The DMN has been consistently found in humans (Raichle et al., 2001; Damoiseaux et al., 2006), in non-human primates (Vincent et al., 2007) and also in rats (Lu et al., 2012; Bettinardi et al., 2015) (see Fig. 1.3).

Other common RSNs, which have been robustly found in several studies, are the visual, auditory, sensorimotor, salience, attention and executive control network (Beckmann et al., 2005; Damoiseaux et al., 2006; De Luca et al., 2006; Mantini et al., 2007; Brookes et al., 2011; Raichle, 2011; Moussa et al., 2012) (see Fig. 1.4). Especially the DMN has been extensively studied and seems to be involved in many different processes such as different self-referential operations (Fransson, 2005; Mason et al., 2007), consciousness of the environment (Fernández-Espejo et al., 2012)

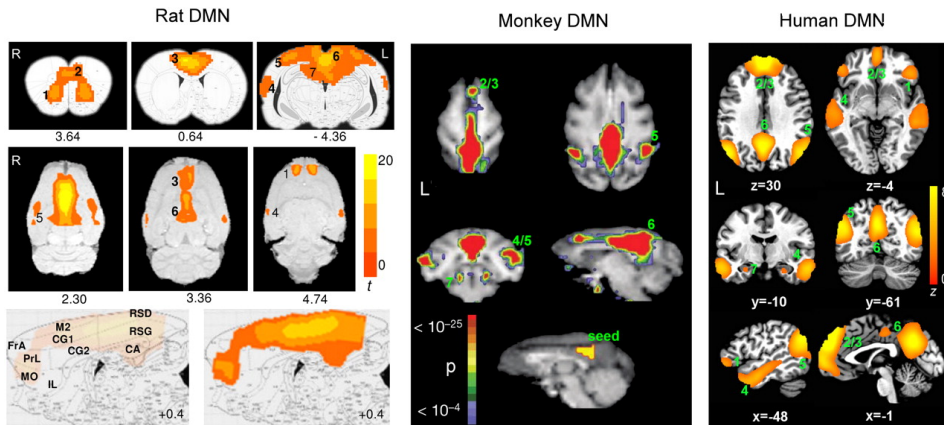


Figure 1.3: **Comparison of the DMN in different mammals (rats, monkeys and humans).** In the three panels the brain regions with increased activity during rest and light sedation are shown. Figure reproduced from Lu et al. (2012).

and of the self (Spreng and Grady, 2010; Qin and Northoff, 2011), episodic memory (Desgranges et al., 1998; Cabeza et al., 2002) and information retrieval (Desgranges et al., 1998; Maguire and Mummery, 1999; Cabeza et al., 2002). Additionally it seems to play an important role in mental disorders such as Alzheimer’s disease, autism, schizophrenia, and depression (Buckner et al., 2008). Furthermore the DMN has been shown to be modulated in form of within- or between-network changes in correlation during sleep (Horowitz et al., 2009; Sämann et al., 2011; Tagliazucchi et al., 2013) and the psychedelic experience provoked by psychedelic drugs such as psilocybin or LSD (Carhart-Harris et al., 2013; Tagliazucchi et al., 2014; Carhart-Harris et al., 2016b).

In the next two sections we will introduce the experimentally observable changes characterizing brain states altered through sleep, anesthesia and psychedelic drugs, which can be determined using the above described methods, such as changes in the functional connectome, altered blood flow in certain brain regions as measured with fMRI and consequently changes in the neuronal activity (Rees et al., 2000; Logothetis et al., 2001; Attwell and Iadecola, 2002; Shmuel and Leopold, 2008; Schölvinck et al., 2010), or variations of the connectivity strength in or between RSNs, just to name a few.

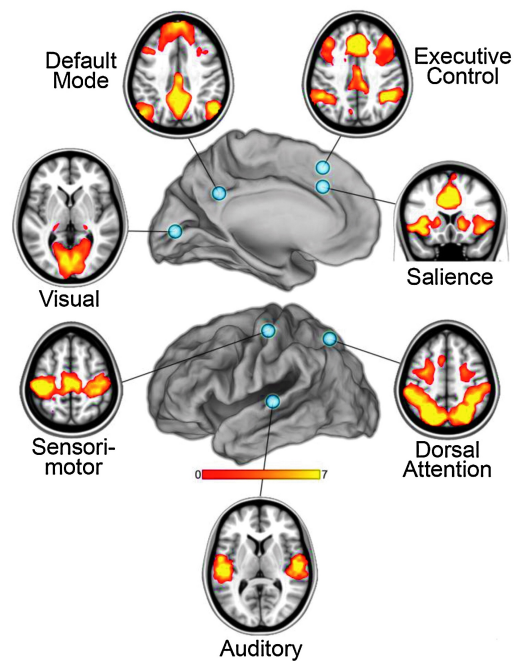


Figure 1.4: **Major resting-state networks (RSNs)**. Seven major RSNs extracted through seed-based spatial coherence from fMRI BOLD signals recorded during rest. Figure adapted from Raichle (2011).

1.2 Deep sleep and anesthesia

Sleep is a reversible brain state, which differentiates itself from wakefulness with reduced responsiveness, immobility and a decreased ability to react to external stimuli (Cirelli and Tononi, 2008). The human sleep cycle is usually classified into phases of rapid eye movement (REM) and non-REM (NREM) sleep, which are further sub-divided into N1, N2 and N3 sleep stages (Iber et al., 2007). These sleep stages are classically characterized applying EEG based on the occurrence of different EEG events (Carskadon and Dement, 2005; Léger et al., 2018).

The lightest sleep stage, N1, is defined as a state between wakefulness and deeper sleep with a usual duration of only a few minutes. In this stage the electrical brain activity as measured with EEG is characterized by the disappearance of the alpha rhythm, the most dominant electrical activity during wakeful rest, and the increased presence of moderate-amplitude

theta waves (Léger et al., 2018).

The next sleep stage, N2, is marked by the appearance of sleep spindles (events which last 0.5-1 s characterized by 10-15 Hz waxing and waning oscillations (Zepelin and Rechtschaffen, 1974)) and K-complexes (delta waves with a more biphasic shape which often occur together with a spindle (Steriade and Amzica, 1998; Cash et al., 2009)). With progression of the sleep depth the appearance of K-complexes and delta waves increases, leading into sleep stage N3, also called deep sleep or slow-wave sleep (Léger et al., 2018). Slow-wave sleep is characterized by delta oscillations (1-4 Hz) and slow oscillations (< 1 Hz), visible in the EEG (Iber et al., 2007). In the here presented studies we will focus on the deepest sleep stage, N3.

Sleep is characterized by widespread changes in neural network activity. In the last decades large-scale neural networks have been identified which are involved in different stages of the human sleep cycle. Decreased neural activity has been found in frontal and parietal cortices during NREM sleep (Braun et al., 1997), as well as in other brain areas such as the temporal cortex, amygdala, hippocampus and hypothalamus (Nofzinger et al., 2002).

In terms of network neuroscience global and local changes in FC have been identified in different stages of the human sleep cycle. fMRI recordings have shown that the FC decreases in fronto-parietal areas during NREM sleep (Horovitz et al., 2009; Sämann et al., 2011; Boly et al., 2012; Nobili et al., 2012). In general, it was shown that cortico-cortical FC decreases significantly during slow-wave sleep (Kaufmann et al., 2005; Horovitz et al., 2009; Sämann et al., 2011; Spoormaker et al., 2012; Tagliazucchi et al., 2012a). In a recent study by Tagliazucchi and Laufs (2014) an extensive whole-brain FC analysis on wakefulness and NREM sleep data divided in the sleep stages explained above, has been performed, where it was shown that while FC increases in N1 and N2 with respect to wakefulness, it drastically decreases in the slow-wave sleep stage (Tagliazucchi and Laufs, 2014) (see Fig. 1.5).

Furthermore it has been demonstrated that the whole-brain functional connectivity becomes more similar to the anatomical or structural connectivity (SC) during deep sleep as compared to wakefulness (Tagliazucchi et al., 2016b) (see Fig. 1.6).

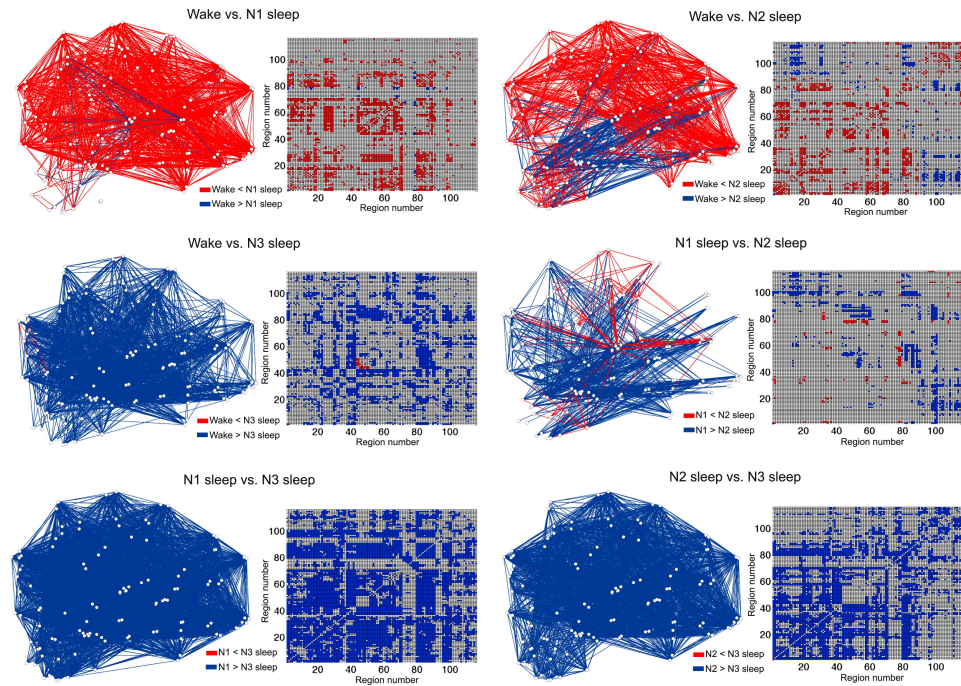


Figure 1.5: **Whole-brain functional connectivity patterns for awake and all 3 NREM sleep stages.** For each pair of sleep stages the significantly different functional connections are visualized as a graph and in functional connectivity matrix form. Figure reproduced from Tagliazucchi and Laufs (2014).

Given the above described global changes of FC during sleep, one would imagine that higher-order cortical RSNs would vanish with progressing sleep depth. It has however been shown that – regarding the spatial extent – the RSNs are generally preserved during all 3 NREM sleep stages and can still be identified even in the deepest sleep stage (Boly et al., 2008; Horovitz et al., 2009; Larson-Prior et al., 2009; Boly et al., 2012; Tagliazucchi et al., 2013) (see Fig. 1.7). These results though concern only the spatial extent of the RSNs, they do not take into account changes in connectivity strength within or between networks. In fact, the DMN has been demonstrated to exhibit altered connectivity strength, especially reduced involvement of the frontal cortex, a reduced network integrity and altered relations to other networks (Horovitz et al., 2009; Sämann et al., 2011), underlining yet again the global changes of spatio-temporal brain activity during reduced vigilance states.

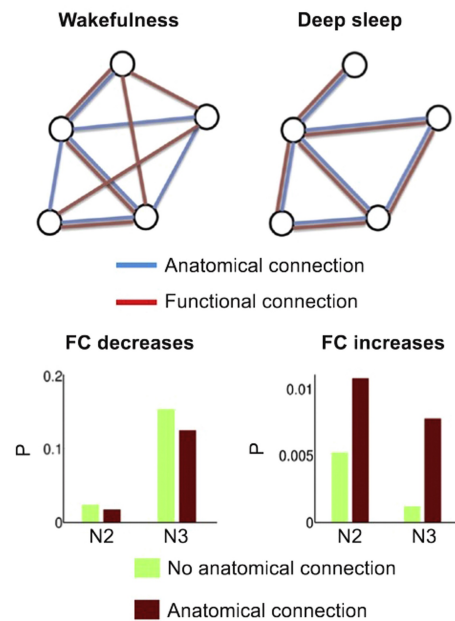


Figure 1.6: **Increased similarity between functional and anatomical connectivity in deep sleep.** Upper panel: schematic representation of anatomical and functional connectivity during wakefulness and deep sleep. Bottom panel: regions with weaker anatomical connections between each other show higher probability of FC decreases during N2 and N3 sleep, whereas for FC increases the opposite is observed. Figure adapted from Tagliazucchi et al. (2016b) and Tagliazucchi and van Someren (2017).

In addition to changes in neural activity, FC and RSN connectivity during sleep, combined transcranial magnetic stimulation and EEG (TMS-EEG) studies, performed by Massimini and colleagues (Massimini et al., 2009; Ferrarelli et al., 2010; Tononi, 2012; Casali et al., 2013), have shown a decrease in cortical effective connectivity (EC) during N3 sleep. Effective connectivity was defined in these studies as the capacity for causal interaction between distinct brain areas in response to an external perturbation with TMS (Massimini et al., 2005, 2007, 2009; Casali et al., 2013). This decrease in EC suggests a reduction of the brain's capability to integrate information on a global level accompanied by a limited communication between different brain areas and a lowered capability of the brain to amplify local stimuli. These findings are also in agreement with leading theories of consciousness, which hypothesize that the capacity of the brain to integrate information corresponds to a conscious brain state and that consciousness

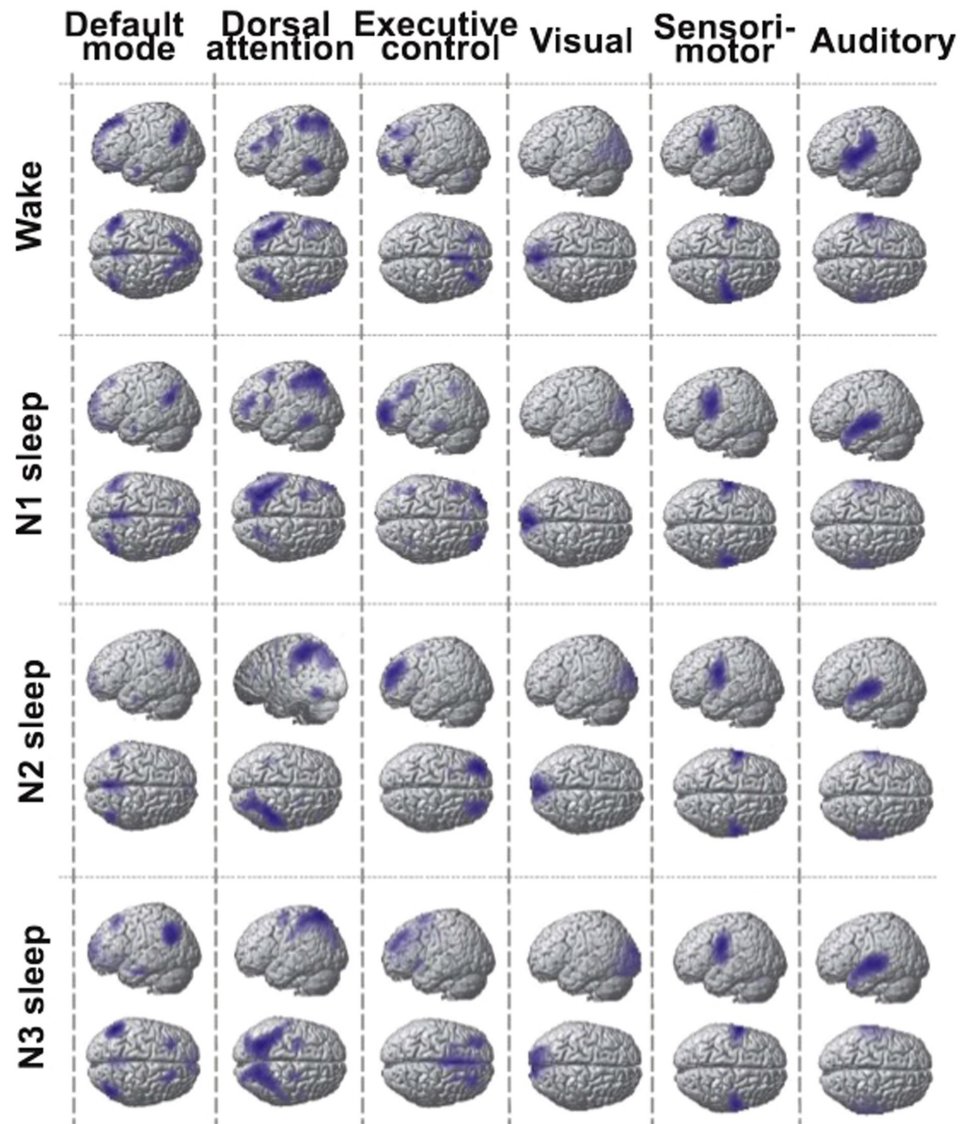


Figure 1.7: **RSN topographies are preserved during NREM sleep.** Default mode, dorsal attention, executive control, visual, sensorimotor and auditory RSN extracted from fMRI BOLD data recorded during wakefulness and all 3 NREM sleep stages. Figure adapted from Tagliazucchi and van Someren (2017).

requires effective communication between different brain regions, which has been shown to be impaired during states of unconsciousness (Dehaene et al., 1998; Tononi et al., 1998; Alkire et al., 2008; Dehaene et al., 2014).

To put the changes in brain activity during sleep in a more general concept of alterations of activity in reduced vigilance states, we will additionally quickly review the anesthetized brain state. General anesthesia introduces a state of temporary loss of awareness or consciousness. At low doses, anesthetics first provoke a state similar to drunkenness with a decrease in focused attention and working memory, amnesia, depersonalization and increased sleepiness (Alkire et al., 2008; Hudetz, 2012). With the increase of the anesthetic dose autonomic reflexes are suppressed (Hudetz, 2012) and at an even higher dose the brain activity decreases until its complete suppression, which would be one of the criteria indicating brain death (Wijdicks, 2001).

One of the main alterations in brain activity during general anesthesia is a global decrease in the cerebral metabolic rate and the cerebral blood flow (Alkire et al., 1995), with especially large effects in the thalamus (Alkire et al., 2008), the cuneus, precuneus, and posterior cingulate and retrosplenial cortex (Fiset et al., 1999) as well as in the frontal cortex (Veselis et al., 2004).

Further, brain connectivity changes under the influence of anesthetics: it has been found that thalamocortical and cortico-cortical interactions are impaired during anesthesia, showing disrupted functional connectivity within fronto-parietal areas and between fronto-parietal areas and the thalamus (Alkire and Miller, 2005). A recent study by Barttfeld et al. (2015) demonstrated in anesthetized non-human primates that FC decreases globally with the depth of anesthesia (see Fig. 1.8) and that with progressing depth of anesthesia the FC becomes more similar to the underlying anatomical activity. A similar result was also described by Vincent et al. (2007), where the coherent spontaneous fluctuations of resting-state activity was analyzed in anesthetized monkeys, and where it was shown that the spontaneous correlation patterns during anesthesia highly correlate with the anatomical connections (see Fig. 1.9) The described disruption of cerebral connectivity indicates a reduction of the brain's ability to integrate information (Bonhomme et al., 2011), characteristic for an unconscious brain state (Dehaene et al., 1998; Tononi et al., 1998; Alkire et al., 2008;

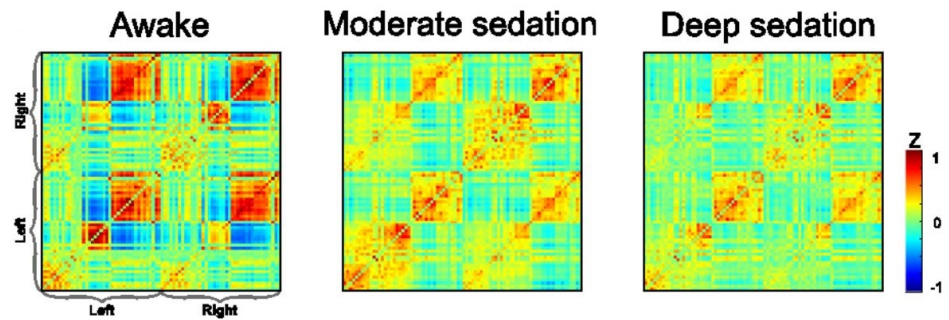


Figure 1.8: **Functional connectivity for different vigilance states.** Average functional connectivity matrices for each of the 3 vigilance conditions. Figure adapted from Barttfeld et al. (2015).

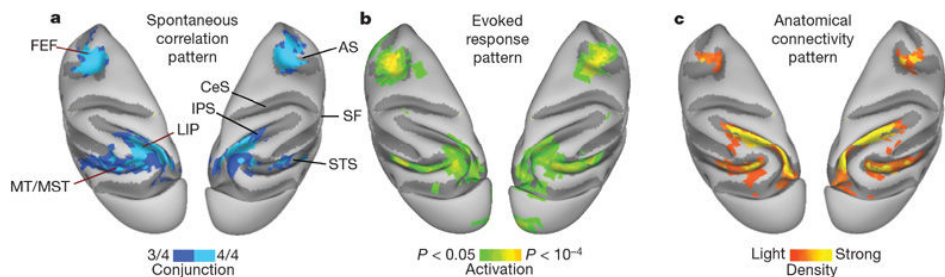


Figure 1.9: **Coherent spontaneous BOLD fluctuations resemble task-evoked responses and anatomical connectivity.** a. BOLD correlation map within the oculomotor system during anesthesia. b. Activation pattern evoked by a saccadic eye movement task. c. Density of cells labeled by retrograde tracer injections into the right lateral intraparietal area. Figure reproduced from Vincent et al. (2007).

Dehaene et al., 2014).

On an RSN level, it was demonstrated by Vincent et al. (2007) that robust RSNs (somatomotor, oculomotor, visual and DMN) were retained during anesthesia, but leaving the doubt if these networks were altered in connectivity strength with respect to wakefulness. Other studies focusing on the DMN, which in analyzing consciousness is of great interest because of its theorized role in self-referential operations (Buckner and Carroll, 2007; Buckner et al., 2008), consciousness of the environment (Fernández-Espejo et al., 2012) and of the self (Spreng and Grady, 2010), have shown that

FC was reduced in the posterior cingulate cortex (one of the main hubs of the DMN) (Greicius et al., 2008). Deshpande et al. (2010) on the other hand demonstrated that FC was globally reduced across the entire DMN. Furthermore it has been found that other higher-order RSNs, such as the external control network and the salience network, disconnected from the thalamus during anesthesia (Boveroux et al., 2010; Liu et al., 2012; Guldenmund et al., 2013) and the external control network showed also reduced activity in anesthesia (Boveroux et al., 2010). On the other hand lower-order RSNs, such as the auditory, sensorimotor and visual networks, were not affected from correlation decreases (Boveroux et al., 2010).

It is evident that both states of reduced vigilance – deep sleep and anesthesia – have lots of traits and characteristics in common, such as reduced neuronal activity, changes in global FC, connectivity alterations within and between RSNs and also a reduction of the capacity of the brain to integrate information, which is why these distinct brain states are often named together when talking about reduced vigilance or unconsciousness. In this thesis, in the Chapters 2 and 3, we will focus on the human brain during deep sleep, trying to find a mechanistic explanation of the discussed characteristic changes in brain activity and connectivity.

1.3 The psychedelic state

The usage of serotonergic hallucinogens in distinct human cultures all over the world – principally for ritual and therapeutic purposes – is a very ancient one (Grinspoon and Bakalar, 1979; Schultes et al., 1992). Classic examples of hallucinogens are lysergic acid diethylamide (LSD), mescaline (present in the peyote cactus), psilocybin (the hallucinogenic component of the so called “magic mushrooms”) and ayahuasca, a psychedelic beverage traditionally used by Amazonian Amerindians (Schultes et al., 1992; Labate and Cavnar, 2011; Labate and Jungaberle, 2011; Labate and Cavnar, 2014; McKenna and Riba, 2016). These drugs have in common that they produce a hallucinogenic effect on the human brain, including alterations of perceptions, mood, cognition and awareness (dos Santos et al., 2016). In this section we will mainly focus on the altering effects on the brain of LSD.

Studies on the effects on the brain of psychedelic drugs, especially lysergic acid diethylamide (LSD), but also psilocybin, have increased drastically within the past few years. LSD is a strong psychoactive drug, which was first synthesized in 1938 by Albert Hofmann, who discovered its psychological effects later in 1943 (Hofmann, 1980). In the 1950s and 1960s LSD was widely used by psychologists and psychiatrists for pharmacological research purposes and clinical applications. In this period the “psychedelic psychotherapy” was extensively applied on psychiatry patients (Grinspoon and Bakalar, 1979). Investigations were performed on possible positive effects of the drug on anxiety associated with terminal cancer, alcoholism, opioid use disorder and depression (Passie et al., 2008). In the late 1960s, though, research on LSD came to a halt due to the prohibition of its use because of its widespread recreational use by the 1960s youth culture.

In the past few years we have witnessed a revival of clinical, pharmacological and neuroimaging research studies performed on psychedelic drugs, mainly on LSD and psilocybin (Carhart-Harris et al., 2012, 2013; Muthukumaraswamy et al., 2013; Carhart-Harris et al., 2014; Roseman et al., 2014; Tagliazucchi et al., 2014; Kaelen et al., 2015; Carhart-Harris et al., 2016a,b; Kaelen et al., 2016; Tagliazucchi et al., 2016c; Carhart-Harris et al., 2017; Preller et al., 2017a,b).

From a neuroimaging point of view, Carhart-Harris et al. (2016b) analyzed fMRI BOLD resting-state data recorded in healthy subjects under the influence of either LSD or Placebo. They found significantly increased cerebral blood flow in the visual cortex (see Fig. 1.10), increased resting-state FC between the primary visual cortex (V1) and various cortical and subcortical areas and increased FC also in other brain areas, such as the parahippocampal region, the dorsomedial prefrontal cortex and the right dorsolateral prefrontal cortex, the ventromedial prefrontal cortex and bilateral caudate and inferior frontal gyrus.

Furthermore they could demonstrate that subjective ratings of hallucinations were significantly correlated with increases in FC in V1. Another main finding in this study was the decrease in FC within the DMN, which was correlated with the subjects’ subjective ratings of “ego dissolution”. Moreover they observed a within- and between-network decrease of resting-state FC in several other commonly found RSNs (see Fig. 1.11) (Carhart-Harris et al., 2016b).

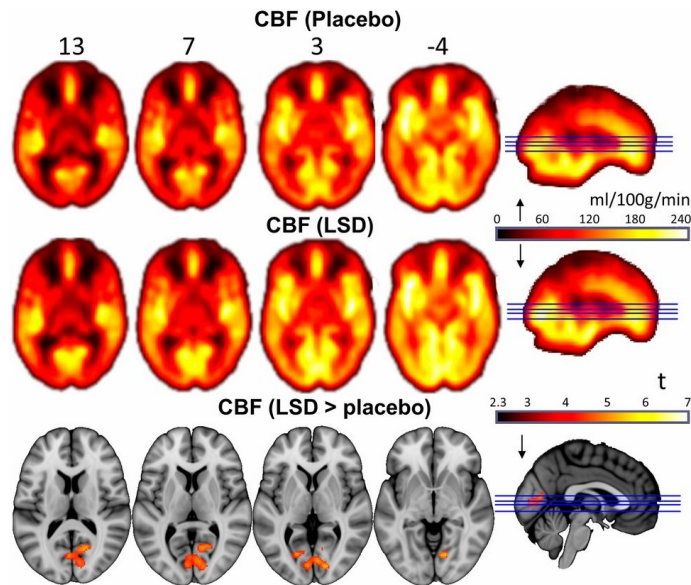


Figure 1.10: **Maps of whole-brain cerebral blood flow in LSD and Placebo conditions.** Visual areas show significantly elevated cerebral blood flow after LSD intake as compared to Placebo. Figure adapted from Carhart-Harris et al. (2016b).

In another recent study by Tagliazucchi et al. (2016c) the effects of LSD on global and local changes in resting-state FC using fMRI BOLD data recorded in a group of healthy participants having been administered either LSD or Placebo have been analyzed. They have shown that after intake of LSD the global FC increased significantly in the thalamus and in high-level association cortices (see Fig. 1.12) and also the communication between association and sensory cortices was increased (see Fig. 1.13). Moreover, the authors demonstrated that the increases in global FC correlated with subjective reports of “ego dissolution” (Tagliazucchi et al., 2016c).

Brain connectivity related changes of the LSD experience have also been studied in combination with music. It has been shown by Kaelen et al. (2016) that under LSD influence simple and complex hallucinations increased as well as personal memory recollection. Furthermore LSD combined with music increased significantly the FC between the parahippocampal cortex and V1, the left anterior insula and the left inferiorfrontal cortex (Kaelen et al., 2016). In another study Kaelen et al. (2015) showed that LSD enhances the emotional response to music, producing

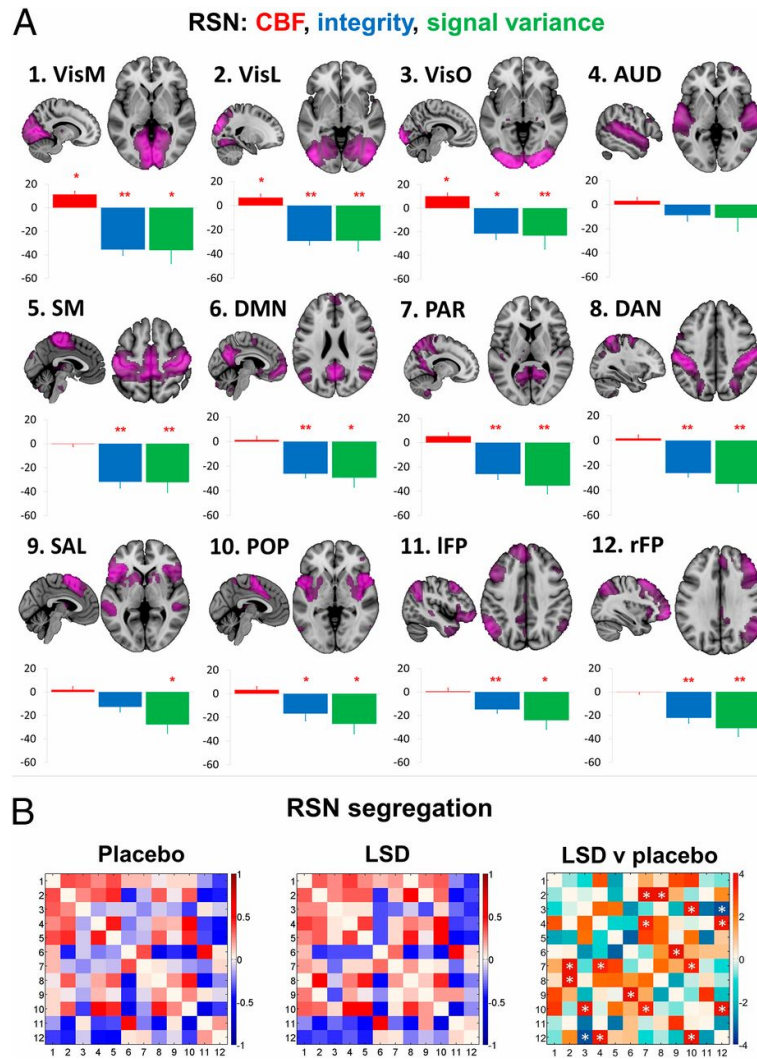


Figure 1.11: **LSD provoked changes in resting-state network integrity, cerebral blood flow, signal variance and segregation.** A. Mean percentage differences (+SEM) in cerebral blood flow, integrity (within-network FC) and signal variance in different RSNs after LSD intake relative to Placebo (red asterisks represent statistical significance). B. RSN segregation (between-network FC) under LSD as compared to Placebo. In the first two matrices positive strength of FC between a pair of different RSNs is indicated in red, negative strength in blue. In the matrix on the right the differences in covariance (t values) between the two conditions are shown: red = reduced segregation, blue = increased segregation under LSD (white asterisks indicate significant differences). Figure reproduced from Carhart-Harris et al. (2016b).

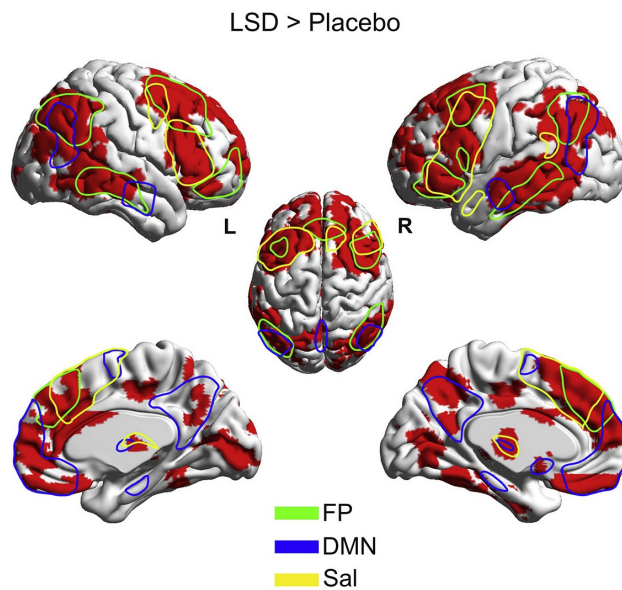


Figure 1.12: **FC increases under LSD.** Significant increases of FC after LSD intake as compared to Placebo primarily in frontal, parietal, and inferior temporal cortices, and in the bilateral thalamus. Outlines of the frontoparietal, salience, and default-mode RSNs are visualized on top of the map. Figure adapted from Tagliazucchi et al. (2016c).

intensified feelings of wonder and transcendence with respect to Placebo intake combined with music, making it therefore an important element in psychedelic-assisted psychotherapy (Kaelen et al., 2015). Yet another very recent study by Preller et al. (2017a) found that previously meaningless or neutral music excerpts were rated more meaningful after LSD intake by healthy participants, demonstrating that LSD assigned meaning to stimuli which were previously meaningless (Preller et al., 2017a).

Similar results have been found in studies applying psilocybin: In an fMRI BOLD study by Carhart-Harris et al. (2013), resting-state network and thalamocortical FC was analyzed under the influence of psilocybin, where it was shown that the FC between the DMN and the salience network, the right frontoparietal network and the auditory network were significantly increased, whereas thalamocortical FC did not show any significant changes (Carhart-Harris et al., 2013). In another study by Tagliazucchi et al. (2014)

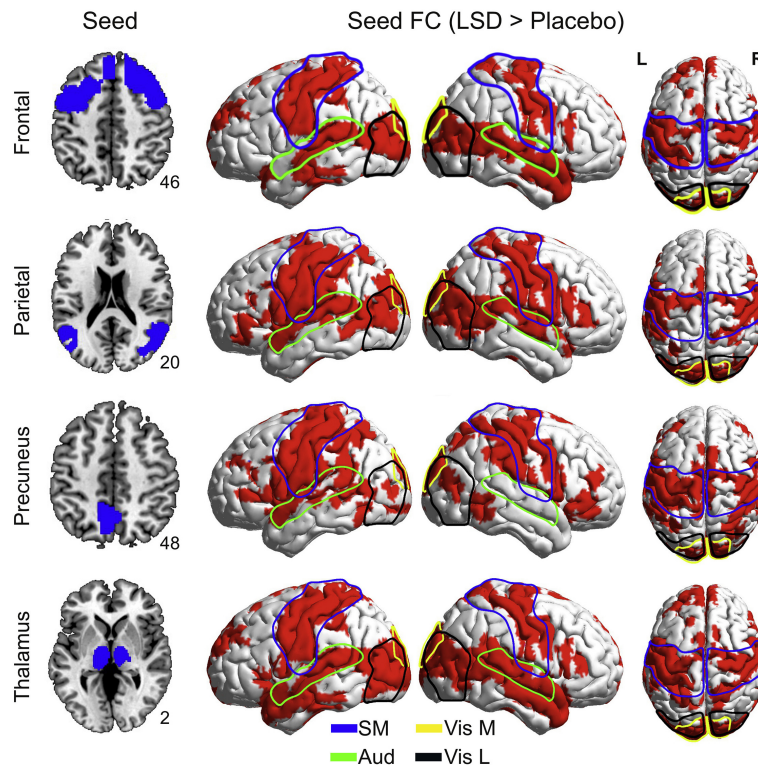


Figure 1.13: **Between-network FC increases under LSD.** Representation of a seed-based correlation analysis based on 4 seeds taken from the map of significant FC increases (see Fig. 1.12) (seed areas in left column). The three right columns show the maps of significantly higher connectivity with the seed regions. These increases overlap with four RSNs: sensorimotor (SM), auditory (Aud), visual medial (Vis M) and visual lateral (Vis L) (outlines visualized on top of the FC maps). Figure reproduced from Tagliazucchi et al. (2016c).

it was demonstrated that under psilocybin the variability of BOLD signal variance and total spectral power was significantly increased in the anterior cingulate cortex and bilateral hippocampi. Furthermore they showed that psilocybin provoked widespread decreases in low frequency power (0.01-0.1 Hz) in frontal and parietal regions, which correspond to higher-level association networks. Moreover, they found an increase in entropy of the dynamical FC states suggesting an expanded repertoire of connectivity states under the influence of psilocybin (Tagliazucchi et al., 2014)

All these results suggest that psychedelic drugs have profound effects on global brain function, whose underlying dynamics have still to be elucidated. So far, very little work has been done on what is causing these experimentally observable changes in global and local brain activity and connectivity. Chapter 4 will be dedicated to analyzing the underlying mechanisms of the psychedelic brain state.

1.4 The need for computational brain models

In the last sections we have discussed some experimentally observed phenomena regarding differences between distinct brain states, such as changes in global and local brain activity, FC, RSN connectivity and effective connectivity. The goal of this thesis is to find a possible explanation of the underlying mechanisms causing these emergent properties to change, and to understand the whole-brain dynamics which they are based on. This is why we need other approaches with more than only the descriptive data analysis perspective, as sophisticated or complex these analysis methods may be.

The main idea is the application of mathematical modeling to simulate the functional characteristics of the empirically observed data to gain insights into the underlying dynamical properties of the system as a whole during a particular brain state. The main advantage of modeling is the fact that we know exactly the underlying conditions which the model is based on and can such tune them and modify them in order to obtain an optimal representation of the experimental data while having total control over the dynamics producing these representations.

Computational brain models can simulate the brain activity on different

levels depending on the model which is applied: microscopic models, which simulate the activity of synapses or individual neurons, mesoscopic brain model, such as neural-mass models simulating the emergent behavior of groups of neurons as measured with local field potentials (LFPs) and macroscopic models, like neural field models, simulating the whole-brain dynamics and interactions between different brain regions, as measured with fMRI, EEG or MEG (Deco et al., 2008; Breakspear, 2017). Within the context of this work we will focus on models representing the macroscopic scale, since in the three studies presented in this thesis our goal is to explain large-scale whole-brain mechanisms emerging from interactions between different cortical and subcortical brain regions measured with fMRI. These models are less complex in the sense that they have a reduced parameter space to explore. Large-scale whole-brain models simulate the activity of large neuronal populations making it possible to reproduce fMRI (Ghosh et al., 2008; Deco et al., 2009; Honey et al., 2009; Cabral et al., 2011; Deco and Jirsa, 2012), MEG (Cabral et al., 2014b; Nakagawa et al., 2014), or EEG signals (Hindriks et al., 2014). In these types of models each brain area is representing a node which is connected to the other nodes by the underlying anatomical connectivity, which has been empirically obtained beforehand. The whole-brain anatomical connectivity or also called structural connectivity is usually based on tract-tracing or diffusion tractography techniques, where diffusion tensor imaging (DTI) (Basser et al., 1994; Le Bihan and Iima, 2015) or diffusion spectrum imaging (DSI) (Wedeen et al., 2005; Fillard et al., 2011) is used to track the fiber tracts in the brain through the direction of the diffusion of water molecules¹.

With the information of the anatomical connections at hand, a global model is built simulating the activity in each brain node, which are connected between each other through the underlying structural connections. The simulated brain activity thus emerges from the anatomical connectivity and the dynamics the applied model is based on, and can then be used to perform all kinds of analyses, while being treated the same way as experimental data. In order to be able to compare the simulated activity to

¹Obtaining the anatomical connections between different brain regions using DTI/DSI fiber tracking or tract tracing is a well established method, of which in this thesis the resulting structural connectivity matrix is only used as a tool for basing the whole-brain computational models on. It would be out of scope of this introduction going into a detailed explanation of the methods and procedures applied to obtain the anatomical connections. See e.g. Mori and van Zijl (2002), Hagmann et al. (2006) or Dell'Acqua and Catani (2012) for more detailed explanations of the method.

the recorded activity, the model needs to be adapted to the experimental data by fitting some characteristic feature, which describes best the state or condition one is interested in (Deco et al., 2009; Honey et al., 2009; Cabral et al., 2011; Deco et al., 2011). Very often, the global FC matrix is used for fitting the simulated to the experimental data. This is done by tuning the free model parameters such that the model becomes an optimized representation of the empirical data. How well the final encountered representation fits the underlying data is determined by the capabilities of the model itself.

Whole-brain computational models can help us on one hand to investigate the large-scale dynamics characterizing different brain states and hence bring us one step further to understand their underlying mechanisms, and on the other hand they represent an important tool to elucidate the connection between anatomical and functional connectivity. In the past decade there have been major advances in applying large-scale brain models to whole-brain activity especially as measured during the resting-state (Honey et al., 2007; Deco et al., 2009; Honey et al., 2009; Knock et al., 2009; Cabral et al., 2011; Deco and Jirsa, 2012; Deco et al., 2013b; Breakspear, 2017). A major finding discovered through the application of whole-brain modeling, is the observation that the brain seems to operate at a critical point during rest, at the edge of a bifurcation representing a transition point between different dynamical regimes (Deco and Jirsa, 2012; Deco et al., 2013b, 2017b). At this point the simulated activity was found to be most similar to the empirically observed features. It is speculated that this property of being close to criticality serves the brain during rest to increase its flexibility and to facilitate the exploration of different functional states, i.e. resting-state networks, in order to be able to efficiently respond to possible external inputs (Deco et al., 2009; Deco and Jirsa, 2012).

The question we want to answer in this thesis is how the system behaves in brain states different from the resting-state and how these altered states affect the dynamical regime the brain is working in. Before elaborating on these topics, we will introduce the large-scale computational brain model which we have applied in the three main studies explained in Chapters 2, 3 and 4 and another model of which the main model can be seen as an extension of.

1.4.1 The Kuramoto model of coupled phase oscillators

The Kuramoto model is a simple, but very powerful model based on a network of coupled phase oscillators simulating synchronization behavior of populations of any kind in different natural systems, may these be biological, physical, chemical or social (Strogatz, 2000; Pikovsky et al., 2003). This model has reached special attention in the field of neuroscience, since it has been associated with neural mass models, where it has been shown by Hoppensteadt and Izhikevich (1997) that the interaction dynamics between weakly-coupled Kuramoto oscillators and weakly-coupled Wilson-Cowan oscillators (Wilson and Cowan, 1972, 1973) resemble each other. Furthermore it has been demonstrated by Schuster and Wagner (1990) that the Wilson-Cowan model (Deco et al., 2009), a type of neural mass model, can be reduced to a network of coupled phase oscillators by only taking into account the phases and not the amplitudes. Cabral et al. (2011) have then successfully simulated whole-brain dynamics during rest applying the Kuramoto model of coupled phase oscillators by approximating the above described reduction of the Wilson-Cowan model. Some years later, Ponce-Alvarez et al. (2015a) applied the Kuramoto model to simulate the emergence of transiently synchronized networks between segregated brain regions.

With the reduction of neural mass models to a model of coupled phase oscillators, the dynamics of a group of neurons representing a brain node is exclusively measured by its phase. Kuramoto (1984) demonstrated that a network of coupled phase oscillators with weak coupling and similar phases can approximate the long-term behavior of interacting oscillatory systems. Assuming that we have a network of N brain nodes, which interact with each other through their phase differences, where the phase of node i ($i = 1, \dots, N$) is given by $\varphi_i(t)$, the temporal evolution of each phase can be represented by the following set of coupled differential equations:

$$\frac{d\varphi_i}{dt} = \omega_i + G \sum_{j=1}^N C_{ij} \sin(\varphi_j(t) - \varphi_i(t)) \quad (1.1)$$

Here ω_i is the natural intrinsic frequency of the i -th oscillator, C_{ij} the $N \times N$ -matrix containing the anatomical connections between the different brain regions and G represents the global coupling strength, which globally scales the anatomical connections. The global strength

level of the anatomical coupling is not known a priori, since the fiber strengths only approximate the effective couplings between different neuronal populations (Honey et al., 2009). The parameter G is used to determine the optimal working point of the model, where the simulated and empirical observations, such as the global FC, are most similar. Two given oscillators are interacting through the sine of the phase differences, $\sin(\varphi_j - \varphi_i)$, which tends to synchronize the oscillators due to the fact that if one of the oscillators is lagging behind the other one ($\varphi_j - \varphi_i > 0$) it will speed up, whereas in the opposite case of one oscillator leading the other ($\varphi_j - \varphi_i < 0$) it will slow down. Thus this model is a very simple, but very powerful way of simulating synchronization behavior in all kinds of systems.

In the next section we will discuss another computational model, which has been applied in the three main studies presented in this thesis in the following chapters. This model can be viewed as an extension of the Kuramoto model, where not only the phases of the oscillators vary, but also their amplitudes.

1.4.2 The Hopf model

This section is based on and reproduces parts of the Methods-sections of two published articles: *Increased stability and breakdown of brain effective connectivity during slow-wave sleep: mechanistic insights from whole-brain computational modelling* published in *Scientific Reports* in 2017. Link: <https://www.nature.com/articles/s41598-017-04522-x> and *Perturbation of whole-brain dynamics in silico reveals mechanistic differences between brain states* published in *NeuroImage* in 2018. Link: <https://www.sciencedirect.com/science/article/pii/S1053811917310236> and one article in preparation for submission: *A perturbational approach for characterizing the dynamics underlying the psychedelic state*. Beatrice M. Jobst, Selen Atasoy, Adrián Ponce-Alvarez, Ana Sanjuán, Leor Roseman, Mendel Kaelen, Robin Carhart-Harris, Morten L. Kringelbach, Gustavo Deco.

The Hopf computational model applied in neuroscience to simulate whole-brain resting-state dynamics as measured with fMRI, is quite a novel formalism adopted by Deco et al. (2017b) based on the normal form of a supercritical Hopf bifurcation (Freyer et al., 2011, 2012). This model has been recently successfully applied to simulate the network dynamics occurring at the ultra-slow scale of resting-state fMRI BOLD signal fluctuations (Deco et al., 2017b; Jobst et al., 2017; Saenger et al., 2017; Deco et al., 2018). The basic idea behind the application of this model to simulate resting-

state dynamics is to combine the two main types of neural mass models, namely oscillatory and asynchronous models, into one (Kringelbach et al., 2015). In the Hopf model the local dynamics in each brain area are simulated by the normal form of a supercritical Hopf bifurcation, which is able to describe the transition from noise-induced oscillations to full sustained oscillations (Kuznetsov, 1998; Deco et al., 2017b) (see Fig. 1.14). When coupled together using brain network architectures, it has been shown that the complex interactions between the local Hopf oscillators can replicate features of brain dynamics observed with electrophysiology (Freyer et al., 2011, 2012), magnetoencephalography (Deco et al., 2017a), and ultimately – as mentioned before – fMRI (Deco et al., 2017b; Jobst et al., 2017; Saenger et al., 2017; Deco et al., 2018).

The model is based on the coupling of the local nodes of the underlying structural connectivity matrix C_{ij} , obtained through DTI based tractography, which contains the fiber densities between all pairs of brain areas. The dynamics of a given uncoupled node j are represented by the following complex-valued equation:

$$\frac{dz_j}{dt} = z(a + i\omega_j) - z|z_j|^2 + \beta\eta_j(t), \quad (1.2)$$

where $z_j = \rho_j e^{i\theta_j} = x_j + iy_j$, $\eta_j(t)$ is additive Gaussian noise with standard deviation β , and ω_j is the intrinsic node frequency.

The following set of coupled equations represents the dynamics of an uncoupled node in Cartesian coordinates:

$$\frac{dx_j}{dt} = \frac{d\text{Re}(z_j)}{dt} = [a_j - x_j^2 - y_j^2] x_j - \omega_j y_j + \beta\eta_j(t) \quad (1.3)$$

$$\frac{dy_j}{dt} = \frac{d\text{Im}(z_j)}{dt} = [a_j - x_j^2 - y_j^2] y_j + \omega_j x_j + \beta\eta_j(t). \quad (1.4)$$

This normal form possesses a supercritical Hopf bifurcation at $a = 0$, meaning that for $a > 0$ the local dynamics settle into a stable limit cycle, producing self-sustained oscillations with frequency $f_j = \frac{\omega_j}{2\pi}$, while for $a < 0$ the damped oscillations lead the system to a stable fixed point (or focus), at $z_j = 0$, and, in the presence of noise, noise-induced oscillations are observed.

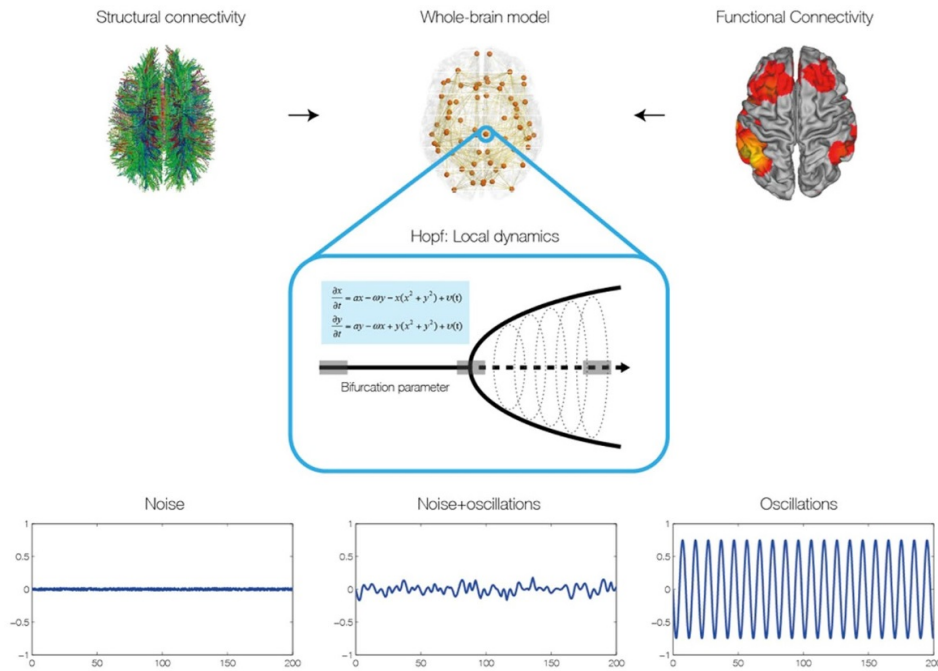


Figure 1.14: **Construction of the Hopf whole-brain model.** A. The whole-brain model is based on the structural connectivity matrix obtained through tractography of DTI (left) between all the distinct brain nodes. The control parameters of the model are adjusted using the FC matrix derived from fMRI BOLD data (right). B. For the simulation of the local neural masses in each node the normal form of a Hopf bifurcation is used, where depending on the dynamical regime the model is in, depending on the bifurcation parameter a (see description of the model equations), the local model produces a noisy signal (left), an oscillatory signal (right) or – at the bifurcation point – a mix of both (middle). It has been shown that the resting-state fluctuations are best approximated in the regime close to the bifurcation, at the border between noisy and oscillatory behavior (Deco et al., 2017b). Figure reproduced from Deco et al. (2017b).

In order to simulate the whole-brain dynamics a coupling term is added which represents the input from node j to node i scaled by the structural connectivity matrix C_{ij} . The whole-brain dynamics are then described by the following set of coupled equations:

$$\frac{dx_j}{dt} = [a - x_j^2 - y_j^2] x_j - \omega_j y_j + G \sum_i C_{ij} (x_i - x_j) + \beta \eta_j(t) \quad (1.5)$$

$$\frac{dy_j}{dt} = [a - x_j^2 - y_j^2] y_j - \omega_j x_j + G \sum_i C_{ij} (y_i - y_j) + \beta \eta_j(t). \quad (1.6)$$

As mentioned above, this model can be interpreted as an extension of the Kuramoto model with amplitude variations, hence the choice of coupling $(x_i - x_j)$, which relates to a tendency of synchronization between two coupled nodes.

Due to the macroscopic nature of the ultra-slow Hopf model considered herein – which explicitly neglects the contribution of faster neurophysiological rhythms – the variable x_j directly emulates the ultra-slow dynamics of the BOLD signal at each node j , without the need to apply a hemodynamic response function, which is necessary in more detailed models of neuronal activity (see also Cabral et al. (2017) for a detailed review exposing this difference between neuronal and large-scale models). The global coupling parameter G is – as in the Kuramoto model described before – the control parameter with which the model is adjusted to the dynamical working region where the simulations optimally fit the empirical data (Deco et al., 2017b; Jobst et al., 2017; Deco et al., 2018).

1.5 Perturbative studies on the brain

Another way of elucidating the underlying mechanisms of brain functioning, besides looking at the spontaneous activity patterns arising during rest, is perturbing the system and evaluating its response. A perturbation of the system can involve different kinds of procedures, ranging from task instructions, external stimuli, brain states which differ from the resting-state, such as those described in the previous sections, artificial external perturbations such as transcranial magnetic stimulation (TMS) and deep brain stimulation (DBS), or a combination of more than one of

these schemes. Here we will mainly focus on artificial external perturbation methods, since a main part of this thesis is dedicated to the introduction and application of a novel method for an artificial in silico perturbational approach based on whole-brain computational modeling helping us to reveal the dynamical properties underlying different brain states.

Within the last 15 years a number of studies have been performed analyzing artificial external perturbations of different brain regions applied in combination with whole-brain electrophysiological and neuroimaging methods to investigate brain function by exploring the dynamical responses to the perturbations (Massimini et al., 2005; Kringelbach et al., 2007a; Litvak et al., 2007; Massimini et al., 2009; Ferrarelli et al., 2010; Mohseni et al., 2012; Casali et al., 2013; Saenger et al., 2017). The artificial perturbations were provoked with either TMS combined with EEG (Massimini et al., 2005; Litvak et al., 2007; Massimini et al., 2009; Ferrarelli et al., 2010; Casali et al., 2013) or DBS combined with MEG (Kringelbach et al., 2007a; Mohseni et al., 2012) or fMRI (Saenger et al., 2017).

Deep brain stimulation (DBS) is based on the implantation of a so called DBS pacemaker or neurostimulator in specific brain regions which electrically stimulates certain brain areas (Kringelbach et al., 2007b). This technique is mainly used in clinical applications, since it has been shown to alleviate the symptoms of certain treatment-resistant disorders such as chronic pain (Marchand et al., 2003; Owen et al., 2006), Parkinson's disease (Krack et al., 2003; Bittar et al., 2005; Little et al., 2013), tremor (Koller et al., 1999; Rehncrona et al., 2003), depression (Mayberg et al., 2005; Schlaepfer et al., 2008) and dystonia (Vidailhet et al., 2005). But DBS can also be applied to study fundamental brain function due to its causal and interventional nature by combining it with non-invasive neuroimaging methods such as MEG, as performed by Kringelbach et al. (2007a), or recently also with fMRI (Saenger et al., 2017).

Transcranial magnetic stimulation (TMS) on the other hand is a non-invasive stimulation technique based on the principle of electromagnetic induction, with which the brain can be stimulated in a noninvasive manner (Barker et al., 1985; Hallett, 2000). For this technique an induction coil is placed over the subject's head while short current pulses are driven through it, which produces a transient magnetic field inducing an electrical current

in the tissues of the head, which is strongest at the cortical surface (Litvak et al., 2007). The activated surface area is usually several square centimeters while the depth of the activation is approximately 2-3 cm (Ruohonen and Ilmoniemi, 1999; Thielscher and Kammer, 2002). One single TMS pulse is capable of activating contralateral muscles when applied over the primary motor cortex (Litvak et al., 2007). This perturbational technique combined with whole-brain neuroimaging or electroencephalography makes it possible to study global brain function, functional connections and causal interactions during rest or other brain states by analyzing the dynamical responses to the perturbations (Massimini et al., 2005, 2009; Ferrarelli et al., 2010; Casali et al., 2013).

In the highly cited study of Massimini et al. (2005), TMS combined with high-density EEG was applied to analyze the changes in cortical information transmission during wakefulness and early non-REM sleep. The authors investigated how the activation of the premotor area was transmitted to the rest of the brain and how this transmission changed under the different brain states. What they found was that during rest after an initial response at the perturbation site a sequence of waves followed which propagated to connected cortical areas, while during sleep the initial response, although being stronger, did not propagate to other areas but was extinguished immediately at the stimulation site. The authors interpreted these results as a breakdown of cortical effective connectivity during sleep in terms of causal interactions between distinct cortical brain regions.

In a later study performed by Ferrarelli et al. (2010), a similar analysis performed on loss of consciousness (LOC) induced by pharmacologic agents was performed, where again the EEG responses to TMS were analyzed. Also here they found more localized activity with shorter duration in the LOC state as compared to wakefulness.

A few years later Casali et al. (2013) introduced an index – the Perturbational Complexity Index (PCI) – to measure the spatio-temporal propagation of an external perturbation on a whole-brain level, with which the authors were able to discriminate the level of consciousness on a single subject level during wakefulness, sleep, anesthesia and minimally conscious levels. The PCI is based on the level of complexity present in the brain which is hypothesized to change during different states of consciousness

(Tononi, 2004; Seth et al., 2008; Boly, 2011). It measures the amount of information contained in the thalamocortical response to a direct perturbation caused by TMS by first localizing the significant electromagnetic sources of the EEG activity and then applying the Lempel-Ziv complexity measure to the binary matrix of sources (matrix dimensions in space and time). With this index the information content of cortico-cortical causal interactions in response to an external perturbation is measured (Casali et al., 2013).

In this thesis, in Chapters 3 and 4, we will introduce a novel method of *in silico* model perturbation, which can be seen as complementary to the works performed by Massimini and colleagues just described. With this novel approach the recovery after the offset of a long-lasting model perturbation is measured, which will be applied to distinguish and characterize different brain states. The perturbation used in this approach is simulated through a computational model by strongly deviating the local node dynamics at the perturbation site from the basal activity, determined through the experimental data, into another dynamical regime, unnatural to its normal behavior. Consequently, the recovery from this perturbation is measured applying a novel index, the Perturbative Integration Latency Index (PILI) over a large number of trials, only possible in a computational model. An important difference to the previously described perturbation procedures by Massimini and colleagues is the fact that with this new approach we measure the recovery characteristics of the system after the offset of the perturbation, not the dynamical reaction to the perturbation itself.

With this concept of *in silico* perturbation as compared to experimental *in vivo* perturbation protocols, the main advantage is the fact that there are no ethical implications or guidelines to follow as for example with DBS (Siebner et al., 2009; Clausen, 2010; Kringelbach and Aziz, 2011), while also being much simpler and much less expensive to perform. Furthermore it is possible to stimulate different brain nodes singularly or even several nodes at a time with strong, long-lasting unnatural perturbations, which can be repeated over large amounts of trials, which is all not feasible in *in vivo* perturbations with TMS or DBS.

A detailed description of this novel method and its application on different brain states will be presented in Chapters 3 and 4.

So far in this introduction we have discussed the functionally relevant differences of distinct brain states when compared to the spontaneous resting brain activity. We have seen that the changes under altered brain states range from alterations in global and local brain activity, functional connectivity, RSN connectivity and effective connectivity. We have also introduced concepts and methods to elucidate the underlying mechanisms and dynamics governing these changes under different brain states. In the following chapters we will elaborate carefully on all of these topics, ranging from the underlying dynamics of slow-wave sleep to an LSD influenced state applying whole-brain modeling and in silico perturbation. Chapters 2 and 3 contain already published work which can be found under the following links:

Chapter 2: *Increased stability and breakdown of brain effective connectivity during slow-wave sleep: mechanistic insights from whole-brain computational modelling* published in *Scientific Reports* in 2017. Link: <https://www.nature.com/articles/s41598-017-04522-x>.

Chapter 3: *Perturbation of whole-brain dynamics in silico reveals mechanistic differences between brain states* published in *NeuroImage* in 2018. Link: <https://www.sciencedirect.com/science/article/pii/S1053811917310236>.

Chapter 4 on the other hand is being prepared for submission under the title: *A perturbational approach for characterizing the dynamics underlying the psychedelic state*. Beatrice M. Jobst, Selen Atasoy, Adrián Ponce-Alvarez, Ana Sanjuán, Leor Roseman, Mendel Kaelen, Robin Carhart-Harris, Morten L. Kringelbach, Gustavo Deco.



The underlying brain dynamics of slow-wave sleep

This chapter contains published work which can be found in: *Increased stability and breakdown of brain effective connectivity during slow-wave sleep: mechanistic insights from whole-brain computational modelling* published in *Scientific Reports* in 2017. Link: <https://www.nature.com/articles/s41598-017-04522-x>.

Recent research has found that the human sleep cycle is characterized by changes in spatio-temporal patterns of brain activity. Yet, we are still missing a mechanistic explanation of the local neuronal dynamics underlying these changes. We used whole-brain computational modeling to study the differences in global brain functional connectivity and synchrony of fMRI activity in healthy humans during wakefulness and slow-wave sleep. We applied a whole-brain model based on the normal form of a supercritical Hopf bifurcation and studied the dynamical changes when adapting the bifurcation parameter for all brain nodes to best match wakefulness and slow-wave sleep. Furthermore, we analyzed differences in effective connectivity between the two states. In addition to significant changes in functional connectivity, synchrony and metastability, this analysis revealed a significant shift of the global dynamic working point of brain dynamics, from the edge of the transition between damped to sustained oscillations during wakefulness, to a stable focus during slow-wave sleep. Moreover, we identified a significant global decrease in effective interactions during slow-wave sleep. These results suggest a possible mechanism for the empirical functional changes observed during slow-wave sleep, namely a global shift of the

brain's dynamic working point leading to increased stability and decreased effective connectivity.

2.1 Introduction

One of the great challenges in neuroscience is to understand the underlying mechanisms taking place in different conscious brain states. Sleep is a reversible state characterized by unresponsiveness and altered consciousness, distinguished from wakefulness by a decrease in the ability to interact with the external world (Cirelli and Tononi, 2008). A long line of sleep research, using primarily EEG, underlies our current classification of sleep into rapid eye movement (REM) and non-REM sleep. Current consensus further sub-divides non-REM sleep into three stages: N1, N2, and N3, where N3 is often referred to as slow-wave sleep (Iber et al., 2007).

From a behavioral point of view the contrast between sleep and wakefulness is clear. However, while the EEG shows clear changes between the two, it is less clear how the brain's spatio-temporal dynamics supports these different behavioral states. From this perspective recent decades research has improved our understanding of wakefulness in particular, characterizing the organization of the brain's spontaneous activity in terms of correlated activity patterns across different brain regions (as measured with fMRI), commonly known as 'resting-state networks' (Biswal et al., 1995; Fransson, 2005; Fox and Raichle, 2007; Lee et al., 2012; Smith et al., 2012). Using ICA and seed-based methods have found that resting-state networks appear to be preserved during sleep, even during slow-wave sleep (Boly et al., 2008; Horovitz et al., 2009; Larson-Prior et al., 2009; Boly et al., 2012; Tagliazucchi et al., 2013). Specifically, the DMN has been shown to be retained during slow-wave sleep (Tagliazucchi et al., 2013) albeit with altered connectivity strength and relations to other networks (Horovitz et al., 2009; Sämann et al., 2011). More generally, slow-wave sleep is associated with a general decrease of cortico-cortical functional connectivity (Kaufmann et al., 2005; Horovitz et al., 2009; Sämann et al., 2011; Spoormaker et al., 2012; Tagliazucchi et al., 2012a), and a diminished level of information integration (Spoormaker et al., 2010; Boly et al., 2012; Spoormaker et al., 2012; Tagliazucchi et al., 2013). The repertoire of functional brain connectivity is constrained by the underlying anatomical connectivity (Greicius et al., 2009), and the functional connectivity is more correlated to the anatomical backbone during states of deep sleep and

anesthesia compared to wakefulness (Barttfeld et al., 2015; Tagliazucchi et al., 2016b).

Furthermore, combined transcranial magnetic stimulation and electroencephalography (TMS-EEG) studies have shown decreased cortical effective connectivity during deep sleep, with effective connectivity understood here as the capacity for a causal interaction in response to an external perturbation (Massimini et al., 2005, 2007, 2009; Casali et al., 2013). This result suggests a lowering of the capability of the brain to integrate information across different cortical areas and a diminished capacity to amplify local perturbations.

These major alterations during deep sleep suggest a change in collective brain dynamics compared to wakefulness, raising the challenge of providing a mechanistic understanding of the empirical observations based on qualitative changes in the local underlying dynamics of the brain.

To address this problem, we first study the differences between wakefulness and deep slow-wave sleep by analyzing functional connectivity and phase synchrony in an fMRI dataset consisting of 18 participants falling asleep in the scanner. We apply a whole-brain computational model based on the normal form of a supercritical Hopf bifurcation incorporating underlying brain dynamics and unfolding over realistic brain anatomical connectivity (Deco and Kringelbach, 2016). This novel model is able to describe the transition from a stable focus presenting noisy oscillations to a stable limit cycle defined by fully sustained oscillations, and can characterize global brain dynamics in terms of their stability and global coupling. We investigate how these parameters change between wakefulness and slow-wave sleep by estimating them from the empirical data and identifying the optimal dynamic working point of each brain state. Finally, to identify the actual level of interaction between different brain nodes, we investigate the differences between the two brain states in terms of their effective connectivity based on the previously mentioned whole-brain model. This approach allows us to find a possible underlying mechanism explaining the empirically observed phenomena.

2.2 Methods

2.2.1 Experimental data

2.2.1.1 Participants

In this study we included a total of 18 young, healthy consecutive participants with data of sufficient quality. Written informed consent was obtained from all subjects. The experimental protocol was approved by the local ethics committee "Ethik-Kommission des Fachbereichs Medizin der Goethe-Universität Frankfurt am Main, Germany" with the ethics application title "Visualisierung von Gehirnzuständen in Schlaf und Wachheit zum Verständnis der Abnormitäten bei Epilepsie und Narkolepsie" and the assigned number: 305/07. The subjects were reimbursed for their participation. The applied methods were carried out in accordance with the relevant guidelines and regulations.

Participants entered the scanner in the evening and underwent a resting-state fMRI session with simultaneous EEG acquisition lasting for 52 minutes. Participants were not instructed to fall asleep, but were asked to relax, close their eyes and not to fight sleep. Lights were dimmed in the scanner room and subjects were shielded from scanner noise using earplugs. For the day of the study all participants reported a wake up time between 5:00 AM and 11:00 AM the night before and a sleep onset time between 10:00 PM and 2:00 AM. These values remained similar throughout the 6 days prior to the experiment. All of the 18 participants included in this study (8 females, mean \pm SD age of 23.1 ± 2.6 years) reached deep sleep (N3) as determined by sleep staging simultaneously acquired polysomnography data according to the standard rules of the American Academy of Sleep Medicine (Iber et al., 2007). For these participants the mean (\pm SD) durations of contiguous sleep epochs were 12.37 ± 6.61 minutes for wakefulness, 8.52 ± 2.83 minutes for N1, 14.69 ± 5.72 minutes for N2 and 16.56 ± 8.39 minutes for N3. These subjects were part of a larger cohort (63 participants in total, 36 females, mean \pm SD age of 23.4 ± 3.3 years). A sub-selection of participants was necessary in order to obtain comparable stretches of time in each sleep stage, since only the aforementioned 18 subjects reached N3 sleep. In this study only wakefulness and deep sleep (N3) were considered.

2.2.1.2 fMRI and EEG data collection

EEG via a cap (modified BrainCapMR, Easycap, Herrsching, Germany) was recorded continuously during fMRI acquisition (1505 volumes of T2*-weighted echo planar images, TR/TE = 2080 ms/30 ms, matrix 64×64 , voxel size $3 \times 2 \times 2 \text{ mm}^3$, distance factor 50%; FOV 192 mm^3) at a 3T Siemens Trio (Erlangen, Germany). An optimized polysomnographic setting was employed (chin and tibial EMG, ECG, EOG recorded bipolarly [sampling rate 5 kHz, low-pass filter 1 kHz] with 30 EEG channels recorded with FCz as the reference [sampling rate 5 kHz, low-pass filter 250 Hz]. Pulse oxymetry and respiration were recorded via sensors from the Trio [sampling rate 50 Hz]) and MR scanner compatible devices (BrainAmp MR+, BrainAmpExG; Brain Products, Gilching, Germany), facilitating sleep scoring during fMRI acquisition (Iber et al., 2007).

MRI and pulse artifact correction were performed based on the average artifact subtraction (AAS) method (Allen et al., 1998) as implemented in Vision Analyzer2 (Brain Products, Germany) followed by objective (CBC parameters, Vision Analyzer) ICA-based rejection of residual artifact-laden components after AAS resulting in EEG with a sampling rate of 250 Hz. EEG artifacts due to motion were detected and eliminated using an ICA procedure implemented in Vision Analyzer2. Sleep stages were scored manually by an expert according to the AASM criteria (Iber et al., 2007). This type of data has been published and well described in several publications (Jahnke et al., 2012; Tagliazucchi et al., 2012a, 2013).

2.2.1.3 fMRI pre-processing

Using Statistical Parametric Mapping (SPM8, www.fil.ion.ucl.ac.uk/spm) Echo Planar Imaging (EPI) data were realigned, normalized (MNI space) and spatially smoothed (Gaussian kernel, 8 mm^3 full width at half maximum). Data was resampled to $4 \times 4 \times 4 \text{ mm}$ resolution to facilitate removal of noise and motion regressors. Note that resampling introduces averaging of BOLD signals, which are finally averaged over cortical and sub-cortical regions of interest (determined by the automatic anatomic labeling [AAL] atlas). Cardiac, respiratory (both estimated using the RETROICOR method (Glover et al., 2000)) and motion-induced noise (three rigid body rotations and translations, as well as their first 3 temporal derivatives, resulting in 24 motion regressors) were regressed out using least squares and retaining the residuals. Data was band-pass filtered in the range 0.01-0.1

Hz 58 using a sixth order Butterworth filter.

2.2.2 DTI data collection and processing

We used the normal structural connectome obtained using DTI in 16 healthy right-handed participants (11 men and 5 women, mean age: 24.75 ± 2.54), recruited through the online recruitment system at Aarhus University. In this study, participants with psychiatric or neurological disorders (or a history thereof) were excluded from participation. The MRI data (structural MRI, DTI) were recorded in a single session on a 3T Siemens Skyra scanner at CFIN, Aarhus University, Denmark. The following parameters have been applied for the structural MRI T1 scan: voxel size of 1 mm^3 ; reconstructed matrix size 256×256 ; echo time (TE) of 3.8 ms and repetition time (TR) of 2300 ms.

The DTI data were collected using $\text{TR} = 9000 \text{ ms}$, $\text{TE} = 84 \text{ ms}$, flip angle $= 90^\circ$, reconstructed matrix size of 106×106 , voxel size of $1.98 \times 1.98 \text{ mm}$ with slice thickness of 2 mm and a bandwidth of 1745 Hz/Px. Furthermore, the data were recorded with 62 optimal nonlinear diffusion gradient directions at $b = 1500 \text{ s/mm}^2$. One non-diffusion weighted image ($b = 0$) per 10 diffusion-weighted images was acquired, approximately. Additionally, the DTI images were recorded with different phase encoding directions. One set was collected applying anterior to posterior phase encoding direction and the second one was acquired in the opposite direction. We used the automated anatomical labeling (AAL) template to parcellate the entire brain into 90 regions (76 cortical regions and 14 subcortical regions, AAL90). The parcellation contained 45 regions in each hemisphere (Dang-Vu et al., 2005). In order to co-register the EPI image to the T1-weighted structural image, we used the linear registration tool from the FSL toolbox (www.fmrib.ox.ac.uk/fsl, FMRIB, Oxford) (Jenkinson et al., 2002). We co-registered the T1-weighted image to the T1 template of ICBM152 in MNI space. The resulting transformations were concatenated and inverted and further applied to warp the AAL template (Tzourio-Mazoyer et al., 2002) from MNI space to the EPI native space, where we preserved the discrete labeling values by applying interpolation using nearest-neighbor method. Accordingly the brain parcellations were conducted in each individuals native space. The acquired DTI data was used to generate the structural connectivity maps for each participant. The two recorded datasets were processed, each with different phase encoding

to optimize signal in difficult regions. To construct these structural connectivity maps we applied a three-step process. First, we defined the regions of the whole-brain network with the AAL template as used in the functional MRI data. Secondly, we used probabilistic tractography to estimate the connections between nodes in the whole-brain network (i.e. edges). Finally the data was averaged across participants.

In order to ensure that the resulting group SC matrix was representative of the average single subject and that no unwanted biases were introduced by averaging across subjects, the single subject SC matrices are represented in Fig. A.1 in Appendix A. Furthermore we performed a consistency analysis following Roberts et al. (2017) (see Fig. A.1 in Appendix A).

In accordance with the procedure applied for analyzing the rs-fMRI data, the AAL template was used to parcellate the entire brain into AAL90. In order to co-register the b0 image in diffusion MRI space to the T1-weighted structural image and then to the T1 template of ICBM152 in MNI space (Collins et al., 1994), we used the FLIRT tool from the FSL toolbox (www.fmrib.ox.ac.uk/fsl, FMRIB, Oxford). We concatenated and inversed the two transformation matrices from the described co-registration steps and applied them correspondingly to warp the AAL templates (Tzourio-Mazoyer et al., 2002) from MNI space to the diffusion MRI native space.

2.2.3 Construction of surrogate data

In order to assess the statistical significance of the results found in this study, surrogate data were constructed under the null hypothesis of no difference between conditions (wakefulness and slow-wave sleep) based on randomly shuffled group assignments. Each of the 18 datasets consists of an awake session and a sleep session recorded in the same subject. Based on these original datasets, surrogate data were created by randomly shuffling the vigilance state assignments with a probability of 0.5. This means that the group sizes remained the same as in the original data, with the difference that for each subject there existed a 50% chance that its brain state assignments were switched between the two recordings. In this way the recordings were not mixed between participants, but the vigilance conditions were randomly shuffled within each group instead. Applying this method, there exists a 50% chance that a data pair "awake-sleep" either remains "awake-sleep" or becomes "sleep-awake", meaning that the groups get randomly mixed and thus fulfilling the null hypothesis of no difference

between conditions. Due to computational demands 100 surrogate datasets were produced which resulted in a minimum possible p-value of 0.0099.

2.2.4 Group averaged functional connectivity matrices

First, the signals were detrended and demeaned before they were band-pass filtered within the range of 0.04-0.07 Hz following Glerean et al. (2012). In order to be able to extract the instantaneous phases of the BOLD signals (see Section 2.2.6), the signals must be filtered within a narrow band. We chose the frequency range of 0.04-0.07 Hz because this frequency band has been mapped to the gray matter and it has been shown to contain more reliable and functionally relevant information compared to other frequency bands and to be less affected by noise (Biswal et al., 1995; Achard et al., 2006; Buckner et al., 2009; Glerean et al., 2012). Subsequently the filtered time series were z-scored, meaning that the mean was subtracted and they were divided by their standard deviation. This was done for each subject, because the standard deviation of the BOLD signal is subject-specific. Next, we calculated the FC matrices for each of the 18 participants for each of the two recordings. The FC matrix is defined as the matrix of Pearson correlations between the BOLD signals of all pairs of regions of interest (ROIs) in the AAL atlas over the whole acquisition duration. Fixed-effect analysis was used to obtain group-level FC matrices, meaning that the Fisher's r-to-z transform was applied to the correlation values before averaging over participants within the two vigilance states and back-transforming to correlation values. This resulted in two final FC matrices, one for each condition. In order to compare the averaged FC matrices between the two vigilance states, we calculated the mean and standard deviation of the upper triangle matrix of both of the FC matrices. We subtracted the resulting mean value for the sleep state from the mean value of the awake state. Finally, to test for significance, the same procedure was performed on the surrogate datasets.

2.2.5 Brain state classification with Gaussian classifier

In order to establish how specific the functional connectivity is to the condition (i.e. wakefulness and slow-wave sleep), we classified the brain state based on the covariance of fMRI signals using a jackknife cross-validation approach, assuming that observations are drawn from a multivariate Gaussian distribution. First, for each vigilance state, the data of $n - 1$ participants (train set) was used to estimate the covariance (Σ_{awake} and Σ_{sleep}), where

n is the number of participants. Note that since the data was z-scored, the mean of each fMRI time series was zero and, thus, in the Gaussian approximation, the fMRI signals were fully determined by their covariance. Second, the data of the remaining subject (test set) was associated to a vigilance state by choosing the zero-mean multivariate Gaussian process ($N(0, \Sigma_{\text{awake}})$ or $N(0, \Sigma_{\text{sleep}})$) that maximizes the log-likelihood of the test data given the trained model. The percentage of correct classifications was computed across the n participants. The likelihood of a test N -dimensional vector X_t , representing the t -th time step of the test data, given the zero-mean multivariate Gaussian process $N(0, \Sigma)$, is given by:

$$P(X_t|\Sigma) = [2\pi\det(\Sigma)]^{-\frac{1}{2}} \exp\left(-\frac{1}{2}X_t^*\Sigma^{-1}X_t\right), \quad (2.1)$$

where $\det(\Sigma)$ is the determinant of the covariance Σ and the superscript $*$ is the transpose. Assuming independence of the observations, the log-likelihood L of the entire test time series $X = X_{1,\dots,T}$, where T is the number of time steps, is given by:

$$L(X|\Sigma) = \log \prod_{t=1}^T P(X_t|0, \Sigma) = \sum_{t=1}^T \log P(X_t|\Sigma), \quad (2.2)$$

In summary, for each test data X , we calculated $L(X|\Sigma_{\text{awake}})$ and $L(X|\Sigma_{\text{sleep}})$ and if $L(X|\Sigma_{\text{awake}}) > L(X|\Sigma_{\text{sleep}})$, the predicted vigilance state was awake, otherwise the predicted vigilance state was sleep.

To assess statistical significance of the classification performance we calculated the probability of getting k correct classifications (hits) by chance, which is given by: $\Pr(k) = C_n^k p^k (1-p)^{n-k}$, where p is the probability of getting a hit by chance ($p = \frac{1}{2}$) and n is the number of tests. Significant decoding was reached when the decoding performance exceeded the 95th percentile of $\Pr(k)$.

We used a similar procedure to evaluate how similar the time series of a single subject are to a random sample from the grouped time series of the other $n - 1$ subjects, in each behavioral condition. Let $X^{(i)}$ be an N -by- T matrix containing the time series of the i -th subject. We estimated the covariance Σ_{train} using the data from the remaining $n - 1$ subjects, but excluding T N -dimensional vectors randomly selected that form a surrogate N -by- T time series X_{pseudo} . We then compared the ratio between the log-likelihoods $L(X^{(i)}|\Sigma_{\text{train}})$ and $L(X_{\text{pseudo}}|\Sigma_{\text{train}})$, i.e.

$r_i = L(X^{(i)}|\Sigma_{\text{train}})/L(X_{\text{pseudo}}|\Sigma_{\text{train}})$, using equations 2.1 and 2.2. We repeated this procedure for 5000 random selections of X_{pseudo} and calculated the average log-likelihood ratio $\langle r_i \rangle$. We expected that $\langle r_i \rangle \sim 1$ if the time series of the i -th subject were indistinguishable from a random sample taken from the time series of the remaining subjects.

2.2.6 Phase synchrony and metastability

For each of the 90 brain regions, we extracted the phases of the band-pass filtered fMRI BOLD signals for each of the 36 recordings (Glerean et al., 2012). The phases were obtained by applying the Hilbert transform to the filtered time series, which results in the associated analytic narrow-band signal, $a(t)$. The analytic signal $a(t)$ of a signal $x(t)$ is defined as $a(t) = x(t) + i \cdot H[x(t)]$, where i is the imaginary unit and $H[x(t)]$ denotes the Hilbert transform of $x(t)$.

We quantify the global level of synchronization between the nodes across time with the Kuramoto order parameter (Kuramoto, 1984), $R(t)$, a measure of phase locking, given by:

$$R(t) = \left| \frac{1}{n} \sum_{k=1}^n e^{i\varphi_k(t)} \right|, \quad (2.3)$$

where n is the total number of nodes and $\varphi_k(t)$ the instantaneous phase of the narrow-band signal at node k . Thus, the Kuramoto order parameter measures the modulus of the average phase of the system at each time point and takes values from 0 to 1, where 0 represents complete phase asynchrony and 1 the completely synchronized case implying phase-locked behavior with a phase difference of 0.

Then, to obtain measures on the group level, we calculated the temporal average and standard deviation of the Kuramoto order parameter per subject and subsequently averaged these measures within groups. Thus, we obtained for each vigilance group two measures: the group average of the mean and of the standard deviation over time of the Kuramoto order parameter, which we termed synchrony and metastability (Shanahan, 2010; Deco and Kringelbach, 2016), respectively. The synchrony represents the global, temporally averaged level of synchronization between all the nodes

of the system, whereas the metastability gives us information about the temporal variation of the synchronization level.

2.2.7 Hopf computational whole-brain model

The Hopf whole-brain model was based on the 90 coupled brain areas or nodes, containing cortical and subcortical regions, derived from the AAL parcellation explained above. The details of the model have been explained in the Introduction of this thesis (see Section 1.4.2 in Chapter 1); a schematic overview of the model and the procedure is presented in Figure 2.1.

The structural connectivity matrix has been scaled to a maximum value of 0.2, following Deco et al. (2017b), leading to a reduced parameter space to search for the optimal parameter combination. Since here we were interested in modeling the slow BOLD signal fluctuations observed in the different brain states, the intrinsic frequency ω_j of each node j was set to the empirical peak frequency estimated directly from the data, as in Deco et al. (2017b) within the frequency range 0.04-0.07 Hz according to the data analysis (see Section 2.2.4). The standard deviation of the additive Gaussian noise was set to $\beta = 0.04$. The final fMRI BOLD signal was simulated by the variables x_j for each node j using the Euler algorithm with a time step of $0.1 \cdot \left(\frac{\text{TR}}{2}\right)$, where TR represents the repetition time, meaning the temporal resolution of the fMRI signal. The two free model parameters, which are used to adjust the model to the empirical dynamics are the bifurcation parameter a and the global coupling parameter G .

2.2.8 Model fitting

We performed a parameter space exploration of the whole-brain model by varying the two free model parameters: the global coupling strength G was varied from 0 to 3 in steps of 0.1 and the bifurcation parameter a from -0.5 to 0.5 in steps of 0.02, where the bifurcation parameter a was changed homogeneously over nodes. The simulated time series were filtered in the range of 0.04-0.07 Hz in accordance with the empirical data and also their length coincided with the duration of the empirical data recordings. Next, we estimated the FC matrix for each parameter combination with the same procedure as explained above. Subsequently we calculated the fitting between the empirical and the simulated FC matrices for the two vigilance states for each parameter combination as the Euclidean distance between the two matrices. This resulted in one fitting value for each parameter

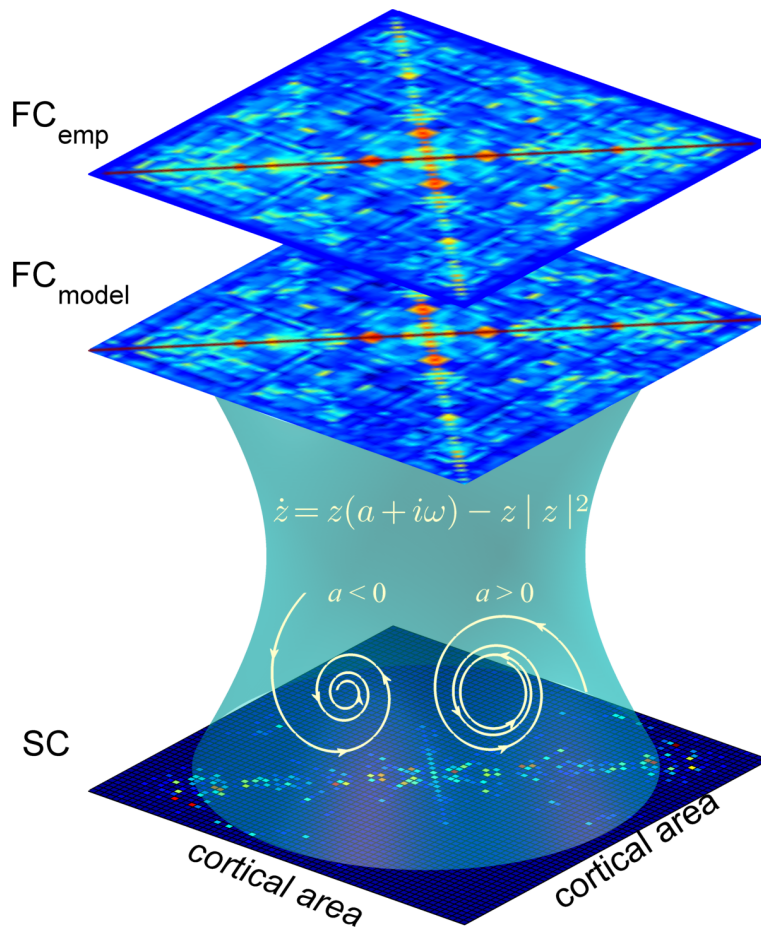


Figure 2.1: **Whole-brain model linking anatomical connections and FC.** The anatomical connectivity data were obtained using DTI averaged over a group of healthy participants. Using the AAL 90 parcellation we obtained an SC matrix linking 90 cortical and subcortical nodes with each other anatomically. Based on this matrix, a Hopf whole-brain computational model was built which simulates the resting activity of the 90 coupled brain areas. The simulated functional connectivity matrix (FC_{model}) was then fitted to the empirical functional connectivity matrix (FC_{emp}) for different model parameter combinations using the Euclidean distance between the values of FC_{model} and FC_{emp} (see Section 2.2.8). With this framework the model parameter space could be explored in order to find the optimal parameter combination for each brain state.

combination per vigilance state. The whole simulation procedure was performed 50 times under exactly the same conditions, over which the results were then averaged. This was done in order to minimize the random effects caused by the Gaussian noise introduced into the model. In order to compare the two states, the minimum distance was calculated for each G from 0.2 onward and the according a was determined for each of the minima. Then, we computed the difference between the awake and the sleep state by subtracting the bifurcation parameter values (in concordance with the optimal fit for each G) of the sleep state minus the awake state. The resulting curve was finally compared to the curves based on the surrogate datasets. The same procedure was performed for each a : the minimum distance was determined for each a and the differences between the two states were computed.

As a next step the synchrony and metastability were computed for the whole parameter space (with G and a varying as above) based on the filtered simulated time series by applying the same procedure as on the empirical data. To compare again the two vigilance states with each other, we determined for each global coupling value G the according bifurcation parameter value a , where the simulated synchrony and metastability, respectively, was closest to the empirical one.

2.2.9 Effective connectivity analysis

The effective connectivity matrix is based on the existing anatomical connections, which were obtained through the DTI fiber tractography as explained above. The general idea of the effective connections between different brain regions is here an update of the existing synaptic weights taking into account the dynamics of the whole-brain model fitted to the empirical data.

For the computation of the EC matrix we used the SC matrix as a primer. Since we took into account only the existing anatomical connections, meaning only the non-zero entries of the SC matrix, we added very small non-zero entries (Matlab machine epsilon: 2^{-52}) compared to the smallest SC non-zero entry ($\sim 8.4 \cdot 10^{-5}$) to the diagonal of the interhemispheric connections, since these are known to be missed by DTI based tractography (Messé et al., 2014). Next, as a first step of the fitting procedure, the SC matrix was weighted with the fraction between the empirical

and the simulated synchrony by applying the Hopf model in order to simulate the BOLD signals as done before. For the model simulations regarding the EC calculation the global coupling parameter and bifurcation parameter were fixed ($G = 1$, $a = 0$). The weighting procedure of the SC matrix was performed as long as the difference between the empirical synchrony and the simulated one was not smaller than 0.1. This weight adjustment was realized in order to bring the SC matrix closer to the final EC estimate and to avoid an exhaustive number of iteration steps in the main EC estimating procedure, which we explain in the next paragraph.

We estimated the EC for each vigilance state using a gradient descent algorithm. The previously updated SC matrix was iteratively adjusted to minimize the Euclidean distance between the empirical FC matrix ('FCemp') and the FC matrix predicted by the model ('FCmodel') through simulations of the network activity. Specifically, each iteration is given by:

$$SC_{ij}^{\text{old}} = SC_{ij}^{\text{old}} + \alpha (FC_{\text{emp}_{ij}} - FC_{\text{model}_{ij}}), \quad (2.4)$$

where α is the learning rate ($\alpha = 0.01$) and (i, j) are the non-zero links of the original SC. We iterated this algorithm while the current Euclidean distance between the empirical and model values was smaller than the one obtained in the previous iteration step. We stopped the re-estimations after 200 iterations. After this procedure, the effective connectivity was given by the last updated SC matrix. Again, as in the general parameter space exploration of the model, the complete procedure for calculating the effective connectivity was performed 50 times with the exact same starting conditions. As before, the reasoning behind this was to minimize the random effects caused by the Gaussian noise present in the model.

In order to assess the differences between the EC matrices in both modalities and to investigate whether the differences were of global or rather local nature, we calculated the node strength of each node of the EC matrix (Barat et al., 2003). Next, we calculated the mean and the standard deviation over the node strength and to test for significance we did the same for the surrogate datasets. We subtracted the mean of the sleep condition from the mean of the awake state and did again the same for the surrogate data, resulting in a global difference measure. In order to determine local differences, we computed the number of nodes displaying higher node strength

during wakefulness than during sleep, and again, for significance testing, we performed the same computation on the surrogate data.

2.2.10 Effective connectivity model validation

In order to test the reliability of the procedure for computing the effective connectivity between different brain areas a simple model validation simulation was performed. First, the EC matrix was calculated as described above by updating the weights of the anatomical connections by fitting FCmodel and FCemp in each iteration step. As a second step the same procedure was repeated, with the difference that the original empirical FC matrix was replaced by the simulated one resulting from the EC calculation in the first step. This is the optimal FC matrix resulting in the n^{th} iteration step, where $n = 1, \dots, 200$, which displays the lowest distance to the empirical FC matrix. This optimal simulated FC matrix served as the new FC ground truth for the computation of the EC matrix. The anatomical connectivity matrix, on the other hand, was kept the same. The EC matrix obtained with this strategy should highly correlate with the original one if the EC computation procedure is reliable.

2.3 Results

We investigated the differences between two different vigilance states: an awake resting-state condition and a slow-wave sleep condition in a group of 18 healthy human participants. We applied a data analysis approach and, to gain further insight, a whole-brain modeling approach in order to examine the differences between the two states in functional connectivity, synchrony, metastability and dynamic working region. Furthermore we analyzed the effective connectivity in both conditions using whole-brain modeling.

2.3.1 Lowering of functional connectivity, phase synchrony and metastability in deep sleep

We analyzed the differences between the awake and the sleep state in functional connectivity, phase synchrony and metastability. We calculated the functional connectivity matrices for the two vigilance states by averaging the matrices of the Pearson correlations between the BOLD signals of all pairs of regions of interest (ROIs) over subjects within one vigilance group. This resulted in two FC matrices, one for each condition. Then, for comparing the two vigilance states, we computed the mean and standard deviation of both of the FC matrices and finally subtracted the mean FC value of the sleep state from the awake state. We found that the difference between the mean FC values in the two conditions was significantly higher than the differences found in the surrogate data created by randomly shuffling vigilance state assignments (awake: 0.471 ± 0.125 , sleep: 0.293 ± 0.152 ; p-value: 0.0099) (Fig. 2.2B). The surrogate data we applied was constructed under the null hypothesis of no difference between conditions, hence appropriate for comparing the two states amongst each other. Additionally, in order to verify that the group FC matrices were indeed representative of the average subject, we calculated the node strength for each individual FC matrix. We found that 83% of all the subjects exhibited higher FC node strength during wakefulness than during sleep (see Fig. A.2A in Appendix A), indicating that the group FC matrices indeed represented the average participant with high accuracy.

Next, in order to quantify the global level of synchronization between the signals of each of the nodes, we computed the Kuramoto order parameter, a temporal measure taking values from 0 to 1, where 0 represents complete phase asynchrony and 1 complete synchronization. Consequently we calculated the temporal mean and standard deviation of the Kuramoto order parameter and averaged over all subjects within one vigilance state group.

We termed these two measures synchrony and metastability, respectively (see Section 2.2.6). We found significantly higher synchrony in awake than in sleep (awake: 0.560, sleep: 0.431; p-value: 0.0099) (Fig. 2.2C) and significantly higher metastability in awake than in sleep (awake: 0.206, sleep: 0.181; p-value: 0.0099) (Fig. 2.2D).

2.3.2 Classification of consciousness state with Gaussian classifier

We evaluated how specific the functional connectivity was to the vigilance state. We used a jackknife cross-validation procedure consisting of: first, calculating the covariances on a subset of the data from $N - 1$ participants, separately for each vigilance state, and then using these covariances to classify the data of the remaining subject (see Section 2.2.5). We found that the Gaussian classifier significantly predicted the vigilance state with high accuracy (83.33% and 94.44% for awake and sleep test sets, respectively) (Fig. 2.2E). Thus, the whole-brain covariance of single participants reliably related to the vigilance state, justifying the use of group measures.

Furthermore, we tested how similar the time series of a single subject were to a random sample from the grouped time series of the other $n - 1$ subjects by using a similar procedure (see Section 2.2.5). We expected the log-likelihood ratio to be approximately 1 if the time series of the i -th subject were indistinguishable from a random sample taken from the time series of the remaining subjects. We found that this was the case for most of the subjects: the log-likelihood ratio ranged between 0.67-1.52 and it was equal to 1.07 ± 0.13 and 1.00 ± 0.06 averaged over subjects, for awake data and sleep data, respectively (see Fig. A.2B in Appendix A). This result confirms that the fMRI time series of single subjects strongly resemble the ones of the group and can be viewed as a random sample taken from it.

2.3.3 Shift of the dynamic working point during sleep

To gain theoretical insights, we fitted a large-scale model of coupled nonlinear oscillators to the data of each of the vigilance states (see Sections 2.2.7 and 2.2.8). We compared the two vigilance states with regards to their dynamic working point, meaning the parameter region where the model fits the data best. We simulated the fMRI BOLD activity in each of the 90 brain regions by using the Hopf whole-brain model with the brain nodes coupled through the empirical SC matrix (see Section 2.2.7 and Fig. 2.1). We performed a parameter space exploration by varying the two free pa-

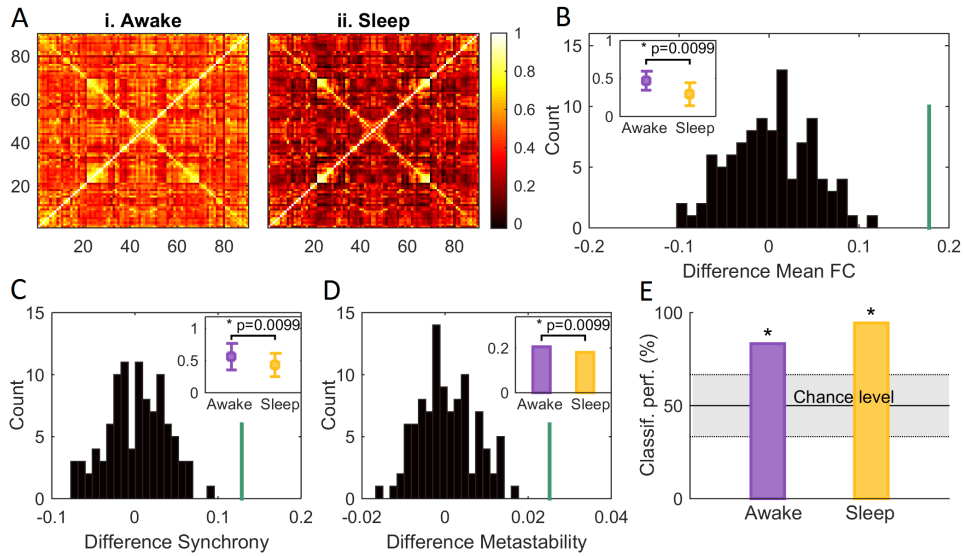


Figure 2.2: **Data Analysis.** In A the FC matrices averaged over participants are shown for the two different vigilance states. In B the difference of the mean of the upper triangle FC matrices (group average) between the awake and the sleep state are shown. The histogram (black) represents the distribution of the test-statistic under the null hypothesis of no difference between vigilance states, whereas the green line shows the difference of the means of the empirical FC matrices. In the upper left corner the mean FCs and their standard deviations are shown. They were significantly different with a p-value of 0.0099. C demonstrates the difference between the mean synchrony (see Section 2.2.6) in the awake state and the sleep state. Again, the histogram represents the distribution of the test-statistic and the green line the difference between the synchrony in awake and sleep obtained from the empirical data. In the upper right corner the means and the standard deviations are shown, the mean synchrony was significantly higher in awake than in sleep with a p-value of 0.0099. In D the difference between the metastability (see Section 2.2.6) in awake and in sleep is shown. The histogram and the green line are to be read as in B and C. In the upper right corner the metastability in awake and in sleep is represented, also in this modality a significant difference (p-value 0.0099) can be observed. In E the classification performance using a Gaussian classifier is shown for awake (violet) and sleep (yellow) test sets, respectively (see Section 2.2.5). The vigilance state was predicted with high accuracy (83.33% and 94.44% for awake and sleep test sets, respectively) exceeding the 95th percentile of chance level.

rameters of the model: the global coupling parameter G and the bifurcation parameter a , where a was changed homogeneously over all nodes. We calculated the model's FC matrix, phase synchrony and metastability for each parameter combination in the same fashion as for the empirical data. Then, we computed the best fit between the empirical and the simulated FC matrices for the two vigilance states (see Section 2.2.8) and found a significant difference between the optimal bifurcation parameters in awake and sleep from a global coupling strength of 1.6 onwards (p-value 0.0396). In detail the optimal fit between empirical and simulated data lied in awake in the bifurcation parameter range between -0.04 and -0.06 and in sleep between -0.08 and -0.12. In general, we observed a better fit in the whole negative bifurcation parameter region in sleep as compared to awake from $G = 0.4$ onwards for awake and from $G = 0.3$ onwards for sleep (Fig. 2.3A+B). Regarding the global coupling parameter, we found that during wakefulness the optimal fit as a function of the bifurcation parameter lied in a higher range of G -values in the vicinity of the bifurcation ($-0.1 \leq a \leq 0$) than during sleep. This means that the connectivity strength between different brain areas was higher during wakefulness as compared to sleep (Fig. 2.3C). Furthermore we analyzed the optimal concordance in the parameter space between the simulated and empirical phase synchrony and equally for the metastability, and also here we found a shift of the optimal fit in sleep as compared to awake to more negative bifurcation parameter values and to lower global coupling strengths (Fig. 2.3D+E).

In summary, the dynamic working point shifted significantly to more negative bifurcation parameter values during sleep as compared to the awake state, where the system remained closer to the bifurcation. Additionally the system presented higher connectivity during wakefulness than during sleep, which benefits the propagation of interaction between different brain regions.

2.3.4 Lowering of the effective connectivity during sleep

In order to determine the actual level of interaction and connectivity between different brain areas, we investigated the differences between the two brain states by studying the changes in the effective connections between different brain nodes. Here we define effective connectivity as a combination of anatomical connectivity and connection weights (i.e., synaptic conductivity), meaning the effective interaction between different brain areas. The EC was estimated by iteratively updating the weights of the non-zero anatomical connections with the weighted difference

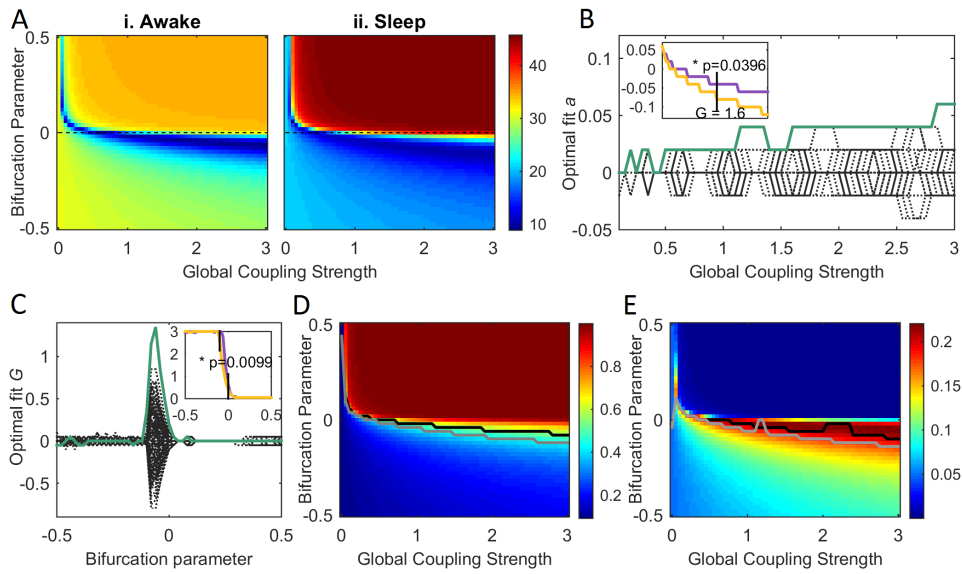


Figure 2.3: Whole-brain model parameter space exploration and fitting. A i.+ii. Euclidean distance between FCmodel and FCemp for different values of the global coupling strength G and the bifurcation parameter a in awake (i.) and sleep (ii.). The optimal fit corresponds to a minimal Euclidean distance. In B the difference between the optimal Euclidean distance fit in awake and in sleep is shown as a function of G . The broken black lines represent the surrogate data constructed under the null hypothesis of no difference between vigilance states, whereas the green line shows the difference between the optimal fit in awake and sleep. In the upper left corner the optimal fit for awake (violet) and sleep (yellow) is shown as a function of G . There was a significant difference between the two states from $G = 1.6$ onward with a corresponding p-value of 0.0396. In C the difference between the optimal Euclidean distance fit in awake and in sleep is displayed as a function of a . The broken black lines and the green line are to be read as in B. In the upper right corner the optimal fit for awake (violet) and sleep (yellow) is shown as a function of a . There was a significant difference between the two states for $-0.1 \leq a \leq 0$ with a corresponding p-value of 0.0099. D represents the simulated global synchrony as a function of G and a . The black line shows the optimal fit for the awake state, namely the closest value to the empirical global synchrony for each G . The gray line shows the same for the sleep state. In E the simulated metastability is displayed, also here as a function of G and a . The black and the gray lines are to be read as in D. Note the observable global shift to more negative bifurcation parameter values in D and E.

between the empirical and the simulated FC matrix (see Section 2.2.9). In each iteration step the Euclidean distance between the empirical and the simulated FC matrix was calculated and if this distance was smaller than the previous one, the EC matrix was updated with the optimized structural weights (see Section 2.2.9). This optimization procedure was performed for 200 iterations, after which the fitting had already reached a stable value (Fig. 2.4C i.+ii.).

Comparing the resulting final EC matrices between the two brain states, we observed a global lowering of the strength of the effective connections in sleep with respect to the awake state (Fig. 2.4A i.+ii.). In order to assess these differences we computed the node strength of the EC matrix for each of the 90 brain nodes (Fig. 2.4D). We found that the mean node strength of the effective connections was significantly higher in awake than in sleep (awake: 0.3520 ± 0.0898 , sleep: 0.2804 ± 0.0854 , p-value: 0.0099) (Fig. 2.4E i.). In addition to that we investigated the local differences between effective connection node strengths and we found that the total number of nodes displaying higher node strength during wakefulness with respect to sleep was significantly higher in the data as compared to the surrogate data. (84 nodes, p-value 0.0495) (Fig. 2.4E ii.). The few regions displaying higher node strength during sleep were the calcarine sulcus (left and right), the cuneus (left and right), the lingual gyrus (right) and the paracentral lobule (left). The 10 regions with the highest difference in node strength between wakefulness and sleep were in order from the highest difference onward: Superior temporal gyrus (right); Precentral gyrus (right); Superior temporal gyrus (left); Postcentral gyrus (right); Putamen (left); Postcentral gyrus (left); Insula (left); Inferior frontal gyrus, pars opercularis (right), Middle occipital gyrus (left) and Inferior occipital cortex (left).

Overall, the effective connections were significantly lower during sleep than during wakefulness. Being this the case for the mean over nodes and also for 93% of the local brain nodes, we suggest, that this observable difference is of global rather than local nature.

2.3.5 Validation of the effective connectivity modeling procedure

Next, we tested the reliability of the procedure for computing the effective connectivity by applying a simple model validation simulation. We computed the EC matrix starting from the optimal simulated FC matrix,

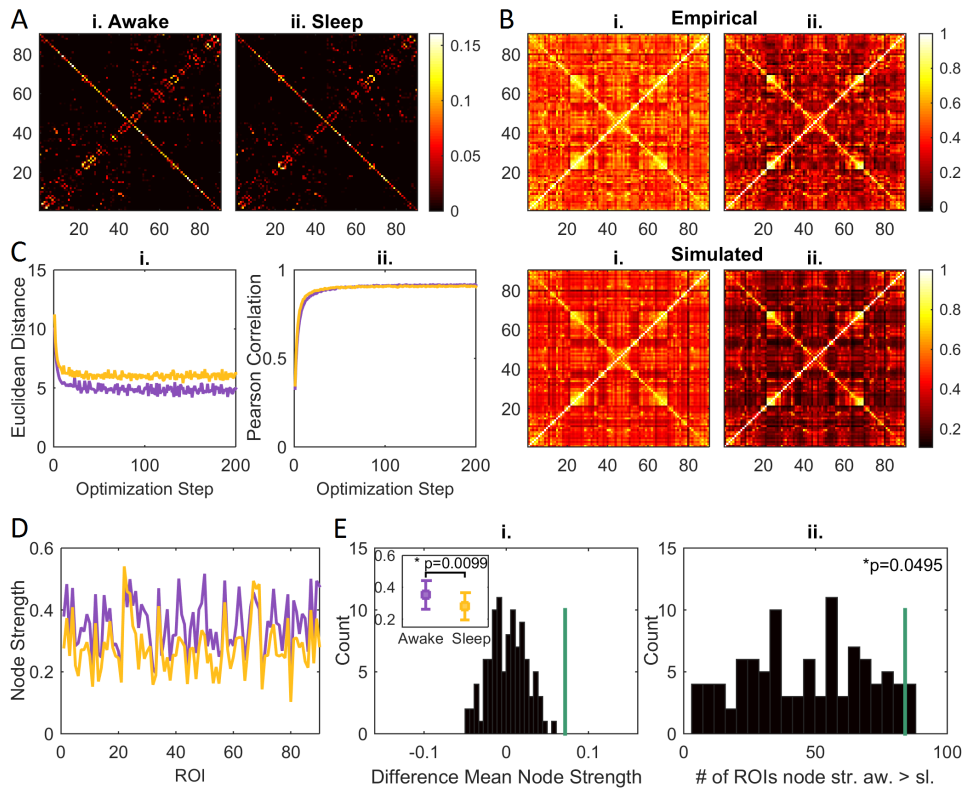


Figure 2.4: **Effective connectivity in awake and sleep.** In A the final EC matrices are shown in awake (i.) and in sleep (ii.). The above row in B displays the empirical FC matrices in awake (i.) and in sleep (ii.), the row underneath the simulated FC matrices (i. awake, ii. sleep) after the EC optimization procedure. C demonstrates the fitting as a function of the iteration steps: in i. the Euclidean distances between FCmodel and FCemp for awake (violet) and sleep (yellow) are shown, and in ii. the Pearson correlation between the two matrices is represented. We obtained node-wise EC values by calculating the node strength of the EC matrices (D). E i. shows the difference between the mean node strength in awake and in sleep. The histogram (black) represents the distribution of the test-statistic under the null hypothesis of no difference between vigilance states, whereas the green line shows the same difference between the actual EC matrices. In the upper left corner the mean node strengths and their standard deviations are shown. They were significantly different with a p-value of 0.0099. In ii. the number of nodes with node strength higher during wakefulness than during sleep are displayed. As before, the histogram represents the test-statistic and the green line the actual number of nodes. The number of nodes with higher node strength in awake than in sleep was significantly higher than obtained with the surrogate data (p-value: 0.0459).

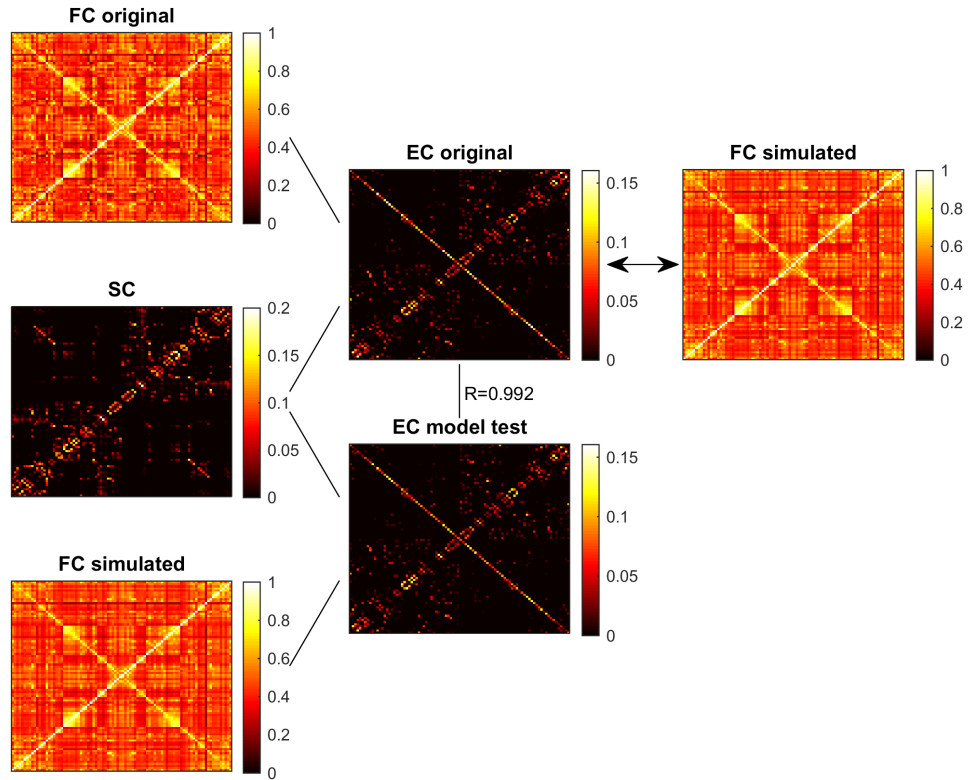


Figure 2.5: **Effective connectivity procedure validation.** The original EC matrix was computed based on the experimental FC matrix. Additionally we calculated the EC matrix based on the optimal simulated FC matrix resulting from the original EC calculation, which served as the new FC ground truth. The anatomical connectivity matrix was kept the same. The two EC matrices were then compared to each other by calculating the Pearson correlation coefficient, which was found to be 0.992.

obtained through the original EC calculation (Fig. 2.4 simulated B i.+ii.), instead of using the empirical one (Fig. 2.4 empirical B i.+ii.) (see Section 2.2.9). We correlated the resulting validation EC matrix with the original one and found a Pearson correlation coefficient of 0.992 (Fig. 2.5), meaning that the procedure for computing the EC matrix was reliable.

2.3.6 Theoretical model response to external stimulus

We have shown that the awake state is associated with a model in which the whole system is positioned closer to a Hopf bifurcation, meaning a closer to

0. This is a functionally relevant feature, since it is known that, close to the bifurcation, the Hopf model has optimal resonance and nonlinear amplification behaviors (Camalet et al., 1999). Indeed, if the system is subjected to a sinusoidal stimulus $F(t) = F e^{i\omega_F t}$ at frequency ω_F , the node's response presents a resonance when it is stimulated at its intrinsic frequency $\omega_F = \omega_0$ (Fig. 2.6A+B). Moreover, in the vicinity of the bifurcation and if the node is stimulated at its intrinsic frequency, the amplitude of the response, $|Z|$, follows the power law $Z \propto F^{\frac{1}{3}}$ (Fig. 2.6C+D). Such power law relation indicates that weak inputs are highly amplified, while strong inputs elicit responses with lower gain. This makes the network to have a large dynamic range of responsiveness.

In conclusion, in the vicinity of the bifurcation the node presents sharp frequency selectivity with high sensitivity allowing for a better communication between nodes and a better reaction to external stimuli.

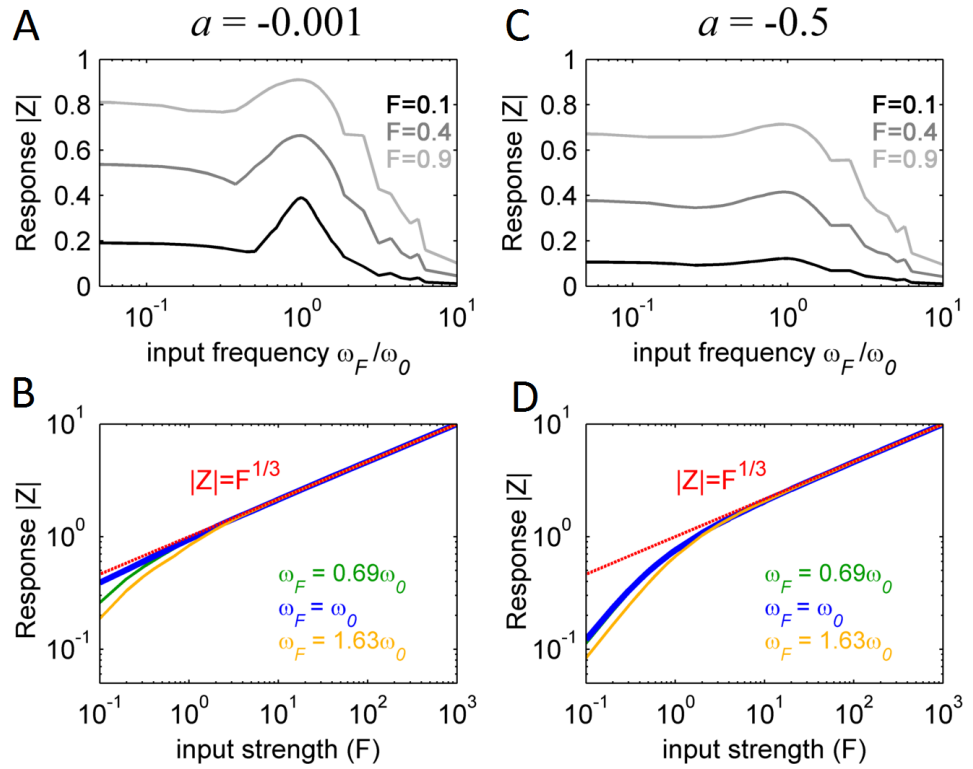


Figure 2.6: **Single node response to external stimulus for two different dynamic working regimes.** In A the response – the absolute value of the simulated complex signal z – of a single node is shown as a function of the input frequency for different input strengths F . ω_0 is the intrinsic frequency, which was here set to 1. B displays the model response as a function of the input strength for different input frequencies. The red line shows hypothetical power law behavior. Both A and B were simulated with the bifurcation parameter a very close to the bifurcation at $a = 0$. C and D show the same as A and B, with the difference that the bifurcation parameter used for the simulations was set to a negative value in the noisy regime of the model. Note that for a close to the bifurcation the model response follows the power law $Z \propto F^{1/3}$ for an input frequency equal to ω_0 , whereas for a in the negative regime this is not the case: weak inputs are no more amplified. In this analysis no noise was added to the system.

2.4 Discussion

We used data- and model-driven analyses to compare the brain states of two different behavioral conditions, namely wakefulness and slow-wave sleep. Using the whole-brain model we found a significant shift of the brain's global working point from the edge of the transition between noisy and sustained oscillatory behavior during wakefulness to a noisy regime characterized by a stable focus during slow-wave sleep as a possible mechanistic explanation of the observed empirical functional changes between those two brain states. We also found that the effective connectivity was reduced in slow-wave sleep compared to wakefulness. Overall, these results suggest that the propagation of external perturbations is decreased in slow-wave sleep compared to wakefulness, with incoming inputs being transmitted with sharper selectivity and higher sensitivity during wakefulness.

Interestingly, in our data-driven analysis, we found that the metastability (i.e. the standard deviation of the phase synchrony) decreased during sleep (Fig. 2.2D). This is particularly interesting given the recent focus on the non-stationarity of resting-state activity, where studies have demonstrated that functional correlations are dynamic and evolve over time (Chang and Glover, 2010; Tagliazucchi et al., 2012b; Hutchison et al., 2013; Allen et al., 2014; Hindriks et al., 2016). Importantly, Ponce-Alvarez and colleagues have shown that the global phase synchrony of the BOLD signals evolves at a very slow time scale of < 0.01 Hz and that with this variability the system visits different synchronized brain states (Ponce-Alvarez et al., 2015a). If, as observed in the case of slow-wave sleep, this variability decreases compared to wakefulness, the dynamical repertoire of the brain during this vigilance state could be limited, indicating that the brain must operate in a different dynamic working region. The finding that slow-wave sleep is more constrained by the underlying structural connectivity further supports this interpretation (Tagliazucchi et al., 2016b).

This fits with our further demonstration that, on average, the functional connectivity was lower during sleep as compared to wakeful rest (Fig. 2.2A+B). This finding is consistent with previous studies showing that the resting-state networks are generally preserved during sleep, but with altered connectivity strength (Horovitz et al., 2009; Sämann et al., 2011). These previous studies show that in slow-wave sleep the cortico-cortical functional connections lose their strength (Kaufmann et al., 2005; Horovitz

et al., 2009; Sämann et al., 2011; Tagliazucchi et al., 2012a), in particular, almost all cortico-cortical connections in the AAL template are reduced during deep sleep (Spoormaker et al., 2010; Tagliazucchi and Laufs, 2014). This clearly demonstrates that the functional connectivity decreases on a global level.

Furthermore, we have shown that the mean phase synchronization was lower during sleep than during wakefulness (Fig. 2.2C). This result supports the fact that the communication in the brain is constrained during slow-wave sleep, as has been found in intracerebral (EEG) recordings, where slow oscillations appear often out-of-phase in different brain regions and appear as events of a local nature (Nir et al., 2011). While these results are valid for electrophysiological data, it has been demonstrated that slow cortical potentials recorded with intracerebral EEG show a similar correlation structure as spontaneous BOLD fluctuations during slow-wave sleep (He et al., 2008; Hiltunen et al., 2014).

In order to find a mechanistic explanation of the empirical results and to learn more about the underlying dynamics, we applied a whole-brain model based on the normal form of a supercritical Hopf bifurcation. We showed that the region where the model fits the data best lied during wakefulness close to the bifurcation, on the edge between noise-induced and self-sustained oscillations, whereas during sleep it shifted to a more negative regime characterized by noisy oscillations. Furthermore, we demonstrated that during wakefulness the optimal global coupling parameter value as a function of the bifurcation parameter was higher in the vicinity of the bifurcation than during sleep (Fig. 2.3). These results indicate that the brain is operating in a different dynamical regime during deep sleep when compared to wakeful rest. The brain's global working point presented higher connectivity and less stability during wakefulness, suggesting that the propagation of activity is increased in this brain state. This allows for better communication between different brain areas and an improved reaction to stimuli during wakefulness. Increased stability implies a failure to amplify weak stimuli, as required, for instance, for the firing of few cells in V1 to globally propagate to the fronto-parietal cortex during conscious access of visual information, according to the Global Neuronal Workspace theory proposed by Dehaene and Changeux (Dehaene et al., 1998; Dehaene and Changeux, 2005; Dehaene et al., 2014). This ignition of the global workspace is facilitated during wakefulness, instead, since

dynamics are posed near the bifurcation point (Fig. 2.6). Our analysis was global in nature and thus could not localize the dynamical changes to sensory areas or the fronto-parietal cortex. Further analyses are needed to identify if the dynamical changes are due to global processes or in fact to local changes influencing the system on a global level. A possible way of expanding the current method in order to look into local region wise changes could be to adapt the bifurcation parameter for each node instead of taking one value homogeneously for all the regions as is done here. In fact this approach has been performed by Deco and Kringelbach (2016), where they optimized the spectral characteristics of each local brain region and thus gained a heterogeneous optimal working point for each brain region. Nevertheless, the here presented method shows a clear shift in the bifurcation parameter and in the global coupling strength, which is an indication for this phenomenon to be more of global nature than of a local one. This is supported by the fact, that for a fixed bifurcation parameter a the model for sleep becomes the model for wakefulness when $G = G + \Delta G$, as can be observed in Figure 2.3A. The whole system is shifted between the two brain states. By increasing the global coupling strength, the mean node strength of the SC matrix is increased, which directly influences the simulated FC matrices in a global way, resulting in a better fit with the empirical FC matrix during wakefulness. On the contrary, decreasing the global coupling strength results in a better fit with the empirical FC matrix during sleep. We tested the scenario of equal FC node strengths in wakefulness and sleep and found that indeed the differences in the dynamical range which fits the data best vanish (see Fig. A.3 in Appendix A). Still, we cannot exclude that local region wise changes are responsible for the globally observed effects.

Another important point is the fact that the Hopf model possesses optimal resonance and amplification behavior when close to the bifurcation as shown in Figure 2.6. We showed that in the vicinity of the bifurcation, as it is the case during wakefulness, the system demonstrates a large dynamic range of responsiveness, showing frequency specificity and power-law behavior. The proximity of the optimal dynamical working point to the bifurcation during wakefulness is functionally relevant in the sense that in this regime sensory inputs are transmitted with sharper selectivity and higher sensitivity due to a better communication between nodes. Furthermore the network has the largest dynamic range of responsiveness. These properties are important and characteristic for an awake state. Additionally the response to stimuli is non-linear. For lower bifurcation parameters, as during deep sleep, we do not observe these properties, and instead the response is dominated by the

linear terms (Camalet et al., 1999). This implies further that close to the bifurcation the system needs to have a higher level of complexity to show the previously mentioned characteristics. This confirms the findings in the studies performed by Massimini and colleagues (Massimini et al., 2009; Ferrarelli et al., 2010; Tononi, 2012; Casali et al., 2013), where the level of consciousness is assessed by measuring the Perturbative Complexity Index (PCI), characterizing the deterministic cortical responses to external perturbations. It has been observed that the PCI is lower during an unconscious state such as slow-wave sleep. This agrees with the fact that during sleep the system is located in the negative bifurcation parameter regime, where it is less complex in the sense that the dynamic range of responsiveness is smaller.

Besides the parameter space exploration of the model, we also simulated the effective connections between different brain areas in order to get a better insight into the actual level of connectivity between different brain nodes. We found decreased effective connectivity on a global level during slow-wave sleep in comparison to wakefulness (Fig. 2.4). Effective connectivity is usually defined as a causal connectivity measure, meaning the directional influences of one brain area or neural element over another (Friston et al., 2003; Tononi and Sporns, 2003; Massimini et al., 2005; Stephan and Friston, 2010). In this work we have applied another approach: here the effective connections were estimated using the anatomical connections, the functional connections and the dynamics given by the model. They can be interpreted as the synaptic weights between the different brain nodes, which are not captured by the structural or functional connections alone. Effective connectivity can be understood as the biophysical "mechanistic causes" of the apparent changes in the functional connections, given that we can explain those changes with changed effective interactions in only existing anatomical links given by the anatomical connections. The observable decrease in EC during deep sleep indicates a drop of integration in the brain on the global level: the communication between different brain areas is limited. This result is compatible with the Integrated Information Theory of Consciousness, which states that consciousness corresponds to the capacity of the brain to integrate information, and other studies which have shown that integration is impaired during unconsciousness (Alkire et al., 2008; Dehaene et al., 2014). Furthermore it is evident, when looking at the node strength of each brain area (Fig. 2.4D), that the effective connections in the two brain states

are only a scaled version of one another. A possible interpretation of this particular result could be that during wakefulness the system demonstrates higher excitability which supports the finding that excitability increases with the time awake (Huber et al., 2013; Ly et al., 2016). When looking more deeply into the set of regions which showed the highest differences in node strength between wakefulness and sleep, we observed that most of these regions are related to the processing of sensory information (superior temporal: auditory, somatosensory: postcentral), motor planning (precentral gyrus which contains the primary motor cortex) and include a subcortical structure (putamen), which is densely connected to both primary somatosensory and motor cortices. The functional isolation of these areas from the rest of the cerebral cortex could indicate diminished levels of arousal during deep sleep. Such diminished arousal comprises lack of motor activity and increased thresholds for awakening – with awakenings due to stimulation during sleep being generally related to either somatosensory and/or auditory stimulation.

The results from the dynamical brain model described in this chapter were obtained using fMRI BOLD signals, but similar, matching brain activity patterns were shown in EEG signals. Deep sleep is characterized by the onset of high amplitude delta (1-4 Hz) waves, which indicates an increment in the local synchronization of neural populations (Amzica and Steriade, 1998). Deep sleep, such as other states of unconsciousness, is governed by bistable oscillations that reflect alternating periods of firing and neural quiescence. This stereotypical pattern of neural firing entails a decrease in the differentiation of brain activity which is related (via the information-integration theory) to diminished conscious awareness (Tononi, 2004).

Our results obtained from modeling whole-brain BOLD dynamics and connectivity reflect these and other electrophysiological observations. Increased stability of oscillations has been reported for the unconscious state induced by propofol, a general anesthetic drug (Solovey et al., 2015; Tagliazucchi et al., 2016a). Furthermore, the effective connectivity of neural activity measured using EEG is notoriously reduced during unconscious states such as deep sleep, general anesthesia and in patients with disorders of consciousness. While in many of these brain states EEG recordings yield patterns of activity with seemingly high levels of local and global synchronization, the propagation of externally induced perturbations (using TMS) is damped during unconscious brain states (Casali et al., 2013). We can speculate that the loss of stability, global coupling and effective connectivity revealed

from fMRI data using our computational model represents the hemodynamic counterpart to these results.

This speculation is consistent from combined EEG-fMRI and positron-emission tomography (PET) studies that relate fluctuations in brain metabolism to delta band power during deep sleep. The work of Dang-Vu et al. (2005) established that frontal metabolism presents an inverse correlation with delta band oscillations during deep sleep. A similar result was obtained by Lei et al. (2014) using concurrent EEG-fMRI recordings. In their paper, Lei et al. showed that fronto-parietal BOLD signals present an inverse correlation with fluctuations in delta power during deep sleep. These studies suggest that frontal (and possible parietal) BOLD signals reflect fluctuations in delta power and that their computational modeling might, in turn, yield insights about the stability and effective connectivity of slow oscillations during deep sleep. To which extent BOLD signal fluctuations from other brain areas reflect slow activity or other independent electrophysiological phenomena remains to be investigated in the future.

2.5 Conclusion

In this work we have suggested a possible mechanistic explanation of the empirical functional changes observed during slow-wave sleep. We have shown that the dynamic working point of the human brain is significantly different during slow-wave sleep compared to wakeful rest. We have demonstrated that during deep sleep the system shifts to a noisy oscillatory state, whereas during awake it stays closer to the bifurcation, and discussed how this might allow the brain to better process information in more complex ways during wakefulness. We have also shown that the brain's global working point presents higher connectivity during wakefulness than during sleep. We suggest that these dynamical changes occur mainly on a global rather than a local scale. This claim is further supported by the fact that the effective connections between different brain areas decrease globally during sleep, which suggests a higher level of integration and excitability during wakefulness on a whole-brain level. Further studies are required to verify if these changes are in fact due to effects on a global level or if the observable effects can be explained by a group of local nodes driving the dynamic system.

Overall, by exploring the mechanistic properties of whole-brain dynamics in two different behavioral states, wakefulness and slow-wave sleep, we have

|

|

added complementary evidence to the developing understanding of the brain as a complex system that supports widely different purposes. Importantly the whole-brain modeling allowed us to explore features of the functional connectome not immediately tractable to standard analysis strategies.

Perturbation of whole-brain dynamics in different brain states

This chapter contains published work which can be found in: *Perturbation of whole-brain dynamics in silico reveals mechanistic differences between brain states* published in *NeuroImage* in 2018. Link: <https://www.sciencedirect.com/science/article/pii/S1053811917310236>.

Human neuroimaging research has revealed that wakefulness and sleep involve very different activity patterns. Yet, it is not clear why brain states differ in their dynamical complexity, e.g. in the level of integration and segregation across brain networks over time. Here, we investigated the mechanisms underlying the dynamical stability of brain states using a novel offline in silico perturbation protocol. We first adjusted a whole-brain computational model to the basal dynamics of wakefulness and deep sleep recorded with fMRI in two independent human fMRI datasets. Then, the models of sleep and awake brain states were perturbed using two distinct multifocal protocols either promoting or disrupting synchronization in randomly selected brain areas. Once perturbation was halted, we used a novel measure, the Perturbative Integration Latency Index (PILI), to evaluate the recovery back to baseline. We found a clear distinction between models, consistently showing larger PILI in wakefulness than in deep sleep, corroborating previous experimental findings. In the model, larger recoveries are associated to

a critical slowing down induced by a shift in the model's operation point, indicating that the awake brain operates further from a stable equilibrium than during deep sleep. This novel approach opens up for a new level of artificial perturbative studies unconstrained by ethical limitations allowing for a deeper investigation of the dynamical properties of different brain states.

3.1 Introduction

Investigating brain function often requires a black box approach, from which information can be obtained by either measuring the spontaneous activity arising from the non-perturbed system, or perturbing the system and measuring how the system responds. This information then serves to postulate mechanistic scenarios, which may be verified via mathematical/computational models. In the case of perturbation, a wide range of schemes is available, ranging from natural interventions such as sensory stimuli or task instructions, to artificial – usually electromagnetic – interventions such as transcranial magnetic stimulation (TMS) or deep brain stimulation (DBS).

Alterations in brain activity elicited by natural perturbations can be detected non-invasively and at the whole-brain level using fMRI, allowing to map the brain regions whose activity correlates with different stimuli or tasks, resulting in a detailed repertoire of task-specific functional networks (Rissman et al., 2004; Raichle, 2009a; Yarkoni et al., 2011). Notably, many of these task-specific functional networks have also been detected in baseline brain activity during rest (Biswal et al., 1995; Raichle et al., 2001; Damoiseaux et al., 2006; Smith et al., 2009; Zhang and Raichle, 2010). With hindsight, the fact that the brain at rest still exhibits highly structured spatio-temporal patterns of activity has important implications for our understanding of brain function (Raichle et al., 2001; Deco et al., 2011; Cabral et al., 2014a; Cole et al., 2014; Deco and Kringelbach, 2016).

Beyond the insights obtained under natural conditions, direct artificial perturbations allow for the systematic exploration of dynamical responses elicited by controlled perturbative protocols. However, such perturbative approaches are generally limited to TMS in healthy humans (Siebner et al., 2009), or DBS in human patients, due to ethical considerations (Kringelbach et al., 2007b; Clausen, 2010; Kringelbach and Aziz, 2011;

Fox et al., 2014). Combining these direct stimulation techniques with whole-brain neuroimaging allows exploring how the system leaves the resting equilibrium by characterizing the resulting dynamics in terms of complexity and latencies using TMS-EEG (Ilmoniemi et al., 1997; Massimini et al., 2005; Litvak et al., 2007; Casali et al., 2013), DBS-MEG (Kringelbach et al., 2007a; Mohseni et al., 2012) and DBS-fMRI (Saenger et al., 2017).

There is a long history of trying to characterize the global dynamics of brain activity in terms of complexity and dynamical stability, particularly in EEG studies (Pereda et al., 1998; Stam, 2005). The general picture that emerges is that brain activity during some diseases, coma and sleep is characterized by dynamical stability and loss of complexity. This phenomenon has been variously characterized in terms of principal component analysis and related decompositions into spatial modes, correlation dimension and dynamical formulations in terms of Lyapunov exponents (Pradhan and Sadasivan, 1996). Indeed, the (fractal) dimension is usually estimated using the Kaplan-Yorke conjecture, based upon estimates of Lyapunov exponents. Heuristically, the Lyapunov exponents reflect the degree of dissipation, decay or relaxation rate of various modes following endogenous or exogenous perturbation (Pradhan and Sadasivan, 1996). In sleep and some pathological brain states the fall in complexity of brain activity is generally accompanied by a loss of critical unstable modes, which increases dynamical stability usually associated with the emergence of slow brain rhythms.

Using an artificial perturbative approach, Massimini and colleagues investigated the perturbation-elicited changes in global brain activity during wakefulness and sleep using TMS-EEG, showing that non-REM sleep is accompanied by a breakdown in cortical effective connectivity, where the stimuli rapidly extinguish and do not propagate beyond the stimulation site (Massimini et al., 2005; Ferrarelli et al., 2010; Casali et al., 2013). These findings corroborate leading theories of consciousness postulating that consciousness requires effective communication between brain regions (Dehaene et al., 1998; Tononi et al., 1998; Dehaene et al., 2014), which appears impaired in certain stages of sleep and anesthesia (Alkire et al., 2008).

To assess the brain-wide spatio-temporal propagation of external stim-

ulation, Casali et al. (2013) introduced the Perturbational Complexity Index (PCI), which measures the amount of information contained in the amplitude of the average perturbation-elicited responses by calculating the Lempel-Ziv complexity of the binary matrix describing the statistically significant sources, in space and time, of the EEG signals. PCI has been successfully used for separation of brain states in healthy subjects during wakefulness, dreaming, sleep, under different levels of anesthesia and in coma (Ferrarelli et al., 2010; Rosanova et al., 2012; Casali et al., 2013). Nevertheless, it is important to note that PCI is obtained from a grand average of an evoked potential, typically with relatively short latencies of 12 s, and ignores the pre-existing variability prior to every individual perturbation as well as the variability in responses across the series of perturbations.

In this work, we expand the traditional perturbative approaches to a new level by using the Hopf whole-brain computational model (see Section 2.2.7 in Chapter 2) that can be systematically perturbed offline *in silico* in ways not possible *in vivo*. This allows for a deeper investigation of the biophysical mechanisms underlying the changes in dynamical complexity observed experimentally between brain states. Using this approach, in Jobst et al. (2017) (see Chapter 2) we have shown that fMRI dynamics of wakefulness and deep sleep can be differentiated by a global coupling parameter that shifts the dynamical regime of the network model.

Following these recent theoretical and experimental insights, we hypothesize that the *in silico* perturbation of the sleep model would result in a faster rate of decay of prominent synchronization modes relative to the awake model, consistent with less complex and more stable dynamics. Operationally, we conjecture that this is associated with a shift in the brain's dynamical regime, which alters the rate of dissipation of induced (or disrupted) synchronization among coupled brain areas, perhaps linked to the phenomenon of critical slowing down (Wissel, 1984; van Nes and Scheffer, 2007). We measure this dissipation using the Perturbative Integration Latency Index (PILI), which measures the recovery of global integration levels back to baseline, scoring the persistence of the largest connected component in terms of BOLD phase synchronization.

3.2 Methods

3.2.1 Overview of perturbative approach

The following procedure, illustrated in Figure 3.1, was implemented:

1. Fit the whole-brain computational model to fMRI data recorded in each brain state, i.e. during wakefulness and deep sleep (stage N3).
2. Compute from simulations the evolution of integration for each unperturbed brain state.
3. Systematic application of two offline perturbation protocols (noise and synchronization) in 1-10 random brain regions and compute the evolution of integration after the offset of perturbation for each brain state.
4. Compute the PILI as the area under the normalized curve of perturbed integration until it reaches the basal integration levels. Repeat trials to estimate significance levels.

3.2.2 Experimental data


We used fMRI data from two independent studies recorded in Frankfurt, Germany (Tagliazucchi et al., 2012a) and Liège, Belgium (Boly et al., 2012) where participants fell asleep during a simultaneous EEG-fMRI scanning session. As in the previous study, also here we only considered the subset of subjects who reached deep sleep (stage N3).

3.2.2.1 Frankfurt dataset

This dataset has been previously described in Tagliazucchi et al. (2012a) and is the same dataset as described in Chapter 2 (see Section 2.2.1 for detailed description). Again, we selected the 18 subjects out of the total 63 who reached slow-wave sleep (N3 stage).

3.2.2.2 Liège dataset

Participants Twenty-five young healthy participants (eleven females, mean age of 22.0 years; age range 18-25 years) were recruited by advertise-



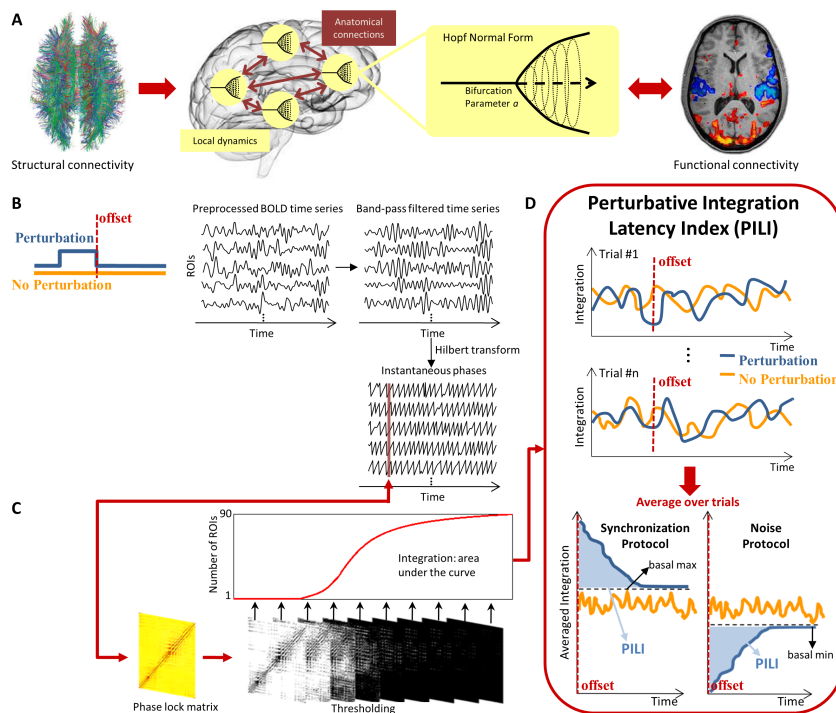


Figure 3.1: **Procedure for computing the Perturbative Integration Latency Index (PILI).** A. First, the whole-brain computational model was constructed based on the empirical structural and functional connectivity between 90 brain regions, each represented by a Hopf bifurcation model. B. Second, the simulated time series for each brain region were band-pass filtered and the instantaneous phases obtained using the Hilbert transform. C. Third, the integration was calculated over 200 s in the basal unperturbed state and after the suppression of a perturbation protocol. For each time point a phase locking matrix was constructed and binarized, calculating the number of regions in the largest connected component for each threshold value. The integration is defined as the integral over all thresholds. D. Finally, the PILI was computed to characterize, in a single value, the recovery to basal equilibrium after the suppression of perturbation. The PILI was computed as the integral between the curves of integration values over time (in light blue) for the perturbed dynamics (dark blue line) compared to the maximum or minimum (black dotted line) of the basal state dynamics (orange line) (see Section 3.2.9 for details).

ment. From this group, only the 12 participants that maintained periods of steady slow-wave N3 sleep were included in this study. None were on medication or sleep deprived. See further details in Boly et al. (2012).

EEG-fMRI acquisition and pre-processing Functional MRI time series were acquired using a 3-Tesla MR scanner (Allegra; Siemens). Multi-slice T2*- weighted fMRI images were obtained with a gradient echo-planar sequence using axial slice orientation [32 slices; voxel size, $3 \times 3.4 \times 3 \text{ mm}^3$; matrix size, $64 \times 64 \times 32$; repetition time (TR) = 2460 ms; echo time (TE) = 40 ms; flip angle = 90° ; field of view (FOV) = 220 mm; delay = 0]. The three initial scans were discarded to avoid magnetic saturation effects. A structural T1-weighted 3D Magnetization Prepared RAPid Gradient Echo (MP-RAGE) sequence (TR = 1960 ms; TE = 4.43 ms; inversion time, 1100 ms; FOV = $230 \times 173 \text{ mm}^2$; matrix size, $256 \times 192 \times 176$; voxel size, $0.9 \times 0.9 \times 0.9 \text{ mm}^3$) was also acquired in all participants.

EEG was recorded using two MR-compatible 32-channel amplifiers (Brainamp MR plus; Brain Products) and an MR-compatible EEG cap (Braincap MR; Falk Minow Services) with 64 ring-type electrodes. The EEG cap included 62 scalp electrodes that were online referenced to a fronto-central electrode (FCz), as well as one electro-oculogram (EOG) and one electro-cardiogram (ECG) channel. Using abrasive electrode paste (ABRALYT 2000; FMS), electrodeskin impedance was kept below 5 kOhm in addition to the 5 kOhm resistor built into the electrodes. To avoid movement-related EEG artifacts, participants' heads were immobilized in the head coil by a vacuum pad. EEG was digitized at a 5000 Hz sampling rate with a 500 nV resolution. Data were analog filtered by a band-limiter low-pass filter at 250 Hz (30 dB per octave) and a high-pass filter with 10 s time constant corresponding to a high-pass frequency of 0.0159 Hz. Data were transferred outside the scanner room through fiber-optic cables to a personal computer where the EEG system running Vision Recorder Software v1.03 (Brain Products) was synchronized to the scanner clock. Sleep EEG was monitored online with BrainProductsRecView Software. For analysis, EEG data were low-pass filtered (finite impulse response filter, 36 dB at 70 Hz), down-sampled to 250 Hz, and re-referenced to linked mastoids. Scanner artifacts were removed in Vision Analyzer, using an adaptive average subtraction. Ballisto-cardiographic artifacts were removed using an algorithm based on independent component analysis.

fMRI processing Processing of the functional fMRI data was carried out using MELODIC (Multivariate Exploratory Linear Decomposition into Independent Components) Version 3.14 (Beckmann and Smith, 2004), part of FSL (FMRIB’s Software Library, www.fmrib.ox.ac.uk/fsl). We used the default parameters of this imaging pre-processing pipeline on all participants: motion correction using MCFLIRT (Jenkinson et al., 2002); non-brain removal using BET (Smith, 2002); spatial smoothing using a Gaussian kernel of FWHM 5 mm; grand-mean intensity normalization of the entire 4D dataset by a single multiplicative factor and high-pass temporal filtering (Gaussian-weighted least-squares straight line fitting, with $\sigma = 50.0$ s). We used tools from FSL to extract and average the time courses from all voxels within each cluster in the AAL90 atlas (i.e. the AAL atlas using cortical and subcortical but not cerebellar regions) (Tzourio-Mazoyer et al., 2002) which were then used to constrain the global coupling of the Hopf model. In brief, our FSL pipeline used *fslmaths* to create a binary mask of each of the 90 clusters in AAL90 in MNI space, which was then used with *fslmeants* to extract and average the full time series for each of these clusters.

3.2.3 Structural connectivity

In the whole-brain network model, the interactions between the 90 brain areas were scaled in proportion to their white matter structural connectivity (Fig. 3.1A). For the present study, we used the structural connectivity between the 90 AAL regions already obtained in previous studies (Deco et al., 2017a; Jobst et al., 2017) and described in Chapter 2 (see Section 2.2.2) averaged across 16 healthy young adults (5 females, mean \pm SD age: 24.75 ± 2.54).

3.2.4 Group averaged functional connectivity matrices

The same pre-processing steps were applied to the time series as described in Chapter 2 (see Section 2.2.4). Pairwise Pearson correlation between all 90 regions was then computed resulting in a 90×90 FC matrix for each participant and brain state. Correlation values were converted to z-values applying Fisher’s transform before averaging across participants in the same cohort, resulting in a 90×90 FC matrix for each brain state (rest and sleep) and for each dataset (Frankfurt and Liège).

3.2.5 Whole-brain computational model

The whole-brain computational model applied in this study was the same as used in the previous chapter (see Section 2.2.7 in Chapter 2), which has been described in detail in the Introduction of this thesis (see Section 1.4.2 in Chapter 1). Also here the intrinsic node frequencies ω_j of each node j were set to the empirical peak frequency of the BOLD signal in each brain region and for each brain state within the frequency range 0.04-0.07 Hz. The distributions of peak frequencies are reported in Figures B.1 and B.2 in Appendix B. In this study we adjusted only one of the two free model parameters – the global coupling parameter G – to the empirical dynamics. The bifurcation parameter a was set to 0 corresponding to the bifurcation point of the model.

3.2.6 Fitting the model to empirical data

To obtain a representative model of BOLD activity in both wakefulness and deep sleep, we first adjusted the model parameters to fit the spatio-temporal dynamics of BOLD signals recorded in each brain state and in each dataset.

In order to mimic the unperturbed basal dynamics in wakefulness and deep sleep, we followed the study by Jobst et al. (2017) where we performed a careful exploration of the model’s parameter space in terms of the global coupling G and the bifurcation parameter a in these two brain states (see Chapter 2). In particular, there we have found that the optimal fit was obtained when the nodes operate in the vicinity of the bifurcation ($-0.1 \leq a \leq 0$) and, for a fixed a in this range, consistently occurred for higher G during wakefulness as compared to sleep (Jobst et al., 2017) (see Section 2.3.3 in Chapter 2). As such, we fixed the local bifurcation parameters at $a_n = 0$ for all nodes, i.e. at the edge of a Hopf bifurcation describing the transition from a noisy to an oscillatory state as in Deco et al. (2017b), and adjusted only the global coupling parameter G in order to match the global level of BOLD phase synchronization measured empirically in each brain state.

To match the level of BOLD phase synchronization, the BOLD signals (both empirical and simulated) were band-pass filtered within the narrow-band 0.04-0.07 Hz and the time-varying phases $\varphi_n(t)$ of each narrow-band signal were computed using the Hilbert transform (Fig. 3.1B)

(Glerean et al., 2012; Ponce-Alvarez et al., 2015a). The Hilbert transform represents a signal, $s(t)$, in the time domain as a rotating vector with an instantaneous phase, $\varphi(t)$, and an instantaneous amplitude, $A(t)$, as $s(t) = A(t) \cos(\varphi(t))$. Knowing the instantaneous phase $\varphi_i(t)$ of each narrow-band BOLD signal at node n , the level of global BOLD phase synchronization over time is given by the Kuramoto order parameter $R(t)$ described in Chapter 2 (see Section 2.2.6). For each value of G ranging between 0 and 1 (with increments of 0.01), we computed the absolute difference between the mean levels of synchronization of simulated and empirical BOLD signals for each brain state and each dataset (see Fig. 3.2, red lines). Note that, for the mean levels of BOLD phase synchronization to be meaningful, the global signal should not be regressed out.

In addition, for each value of G , we calculated a simulated FC matrix as the 90×90 correlation matrix between the simulated BOLD signals (x_n) in all 90 regions. Correlation values were converted to z-values applying Fisher's transform and the simulated FC matrices were compared to the empirical ones obtained for each brain state (see Section 3.2.4) by calculating the Pearson correlation coefficient between the elements of the upper triangular part of both empirical and simulated FC matrices.

3.2.7 Offline perturbation protocols

Despite being purely phenomenological, the Hopf model is particularly well-suited for perturbative studies because each brain area n has a local parameter a_n that defines the distance to a supercritical Hopf bifurcation, inducing synchronized BOLD fluctuations for $a_n > 0$ and strong noise for $a_n < 0$ (Kringelbach et al., 2015; Deco et al., 2017b). We used two different offline perturbation protocols eliciting strong deviations from the basal (i.e. unperturbed) state dynamics by artificially imposing more synchronization or temporarily suppressing synchronization in different brain regions. In order to attenuate the local effects associated to the perturbation of specific brain areas, we systematically repeated each protocol 3000 times, perturbing a different set of randomly selected brain regions in each trial.

1. *Synchronization perturbation protocol*: 1 to 10 randomly selected brain regions were simultaneously perturbed for 100 s by shifting their local bifurcation parameter values to the positive range ($a_n = 0.6$), which imposes more synchronized oscillatory BOLD signals.

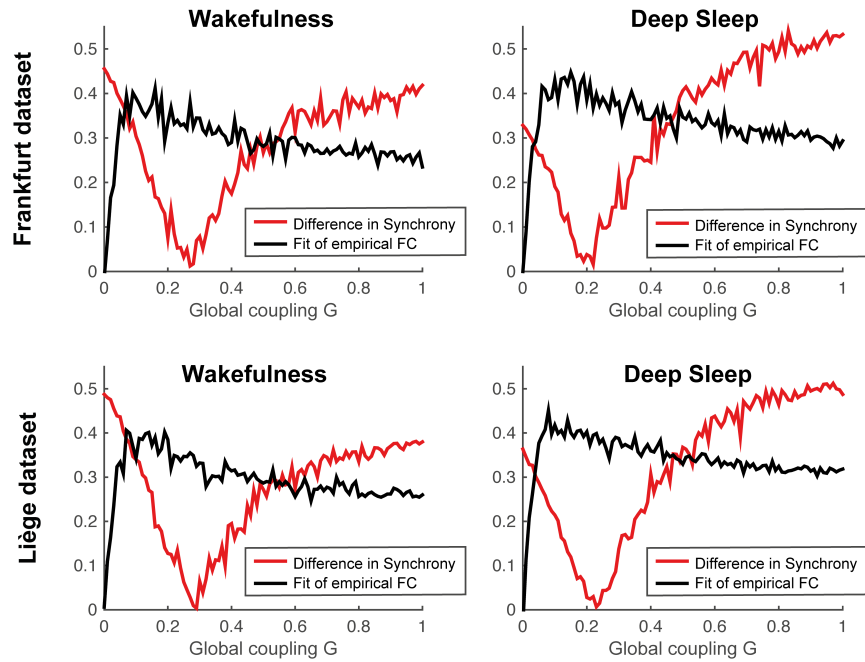


Figure 3.2: **Adjusting the Hopf whole-brain model to the basal brain activity of wakefulness and deep sleep.** Before applying the perturbative protocol, we first defined the model parameters of the Hopf whole-brain model in order to obtain a representative model of the brain activity recorded during wakeful rest and deep sleep using fMRI from two independent studies (Frankfurt and Liège) (Jobst et al., 2017). The red line shows the difference between synchrony degrees, such that, when the synchrony error reaches zero, the mean synchrony degree of simulated BOLD signals matches the one measured empirically. In addition, the black line shows the correlation between empirical and simulated FC matrices, which is kept high for the range where the synchronization error is optimal.

2. *Noise perturbation protocol*: To temporarily suppress synchronization, the local parameters of 1-10 randomly selected brain regions were simultaneously shifted to the negative region ($a_n = -0.6$) for 100 s eliciting more noisy behavior and hence causing an artificial perturbative destruction of the basal synchronization across the different brain areas.

In both protocols, the bifurcation parameters were reset to zero after perturbation.

3.2.8 Integration over time

To characterize the level of brain-wide BOLD signal interactions across time, we used an observable measure that summarizes in a single value for each time point the level of integration across the whole brain previously defined in Deco et al. (2015), and which characterizes the broadness of communication between brain regions at the instantaneous level (Lord et al., 2017).

To calculate the integration, first we used the BOLD signal phases $\varphi_n(t)$ (obtained using the Hilbert transform, see Section 3.2.4) to calculate a phase locking matrix P , describing for each time point the level of pairwise phase synchronization between regions n and p as:

$$P_{np}(t) = \operatorname{Re} \left| e^{-3(\varphi_n(t) - \varphi_p(t))} \right| = \cos(\varphi_n(t) - \varphi_p(t)) \quad (3.1)$$

Based on this phase locking matrix, we computed the level of integration $I(t)$ at each time point t as the size of the largest connected component of $P(t)$ averaged over thresholds (Deco et al., 2015). More specifically, for a given absolute threshold θ between 0 and 1 (scanning the whole range), P was binarized (0, if $|P_{np}| < \theta$, 0 and 1 otherwise). For each threshold θ and for each time t , the number of nodes in the largest connected component of $P(t)$ was extracted (see Fig. 3.1C). The largest component is the largest sub-graph of the binarized $P(t)$, in which any two vertices are connected to each other by paths, and which connects to no additional vertices. In order to be independent of a given threshold, we repeated this procedure scanning all possible thresholds (between 0 and 1) and defined the integration at each time t , $I(t)$, as the integral of the largest component curve as a function of the thresholds. It has been shown recently that this measure is both

sensitive and specific with the ability to classify FC differences associated with different diseases and brain states (Deco et al., 2015). Following this procedure, we calculated the integration over 200 s of simulated BOLD signals in the basal conditions and right after perturbation offset.

3.2.9 Perturbative Integration Latency Index

The Perturbative Integration Latency Index (PILI) characterizes the recovery of the perturbed brain dynamics to regain basal equilibrium after suppression of the perturbation (see Fig. 3.1D). The key idea is to characterize the latency of extinction of a massive stimulation perturbing a basal state. Thus, to determine when the evoked perturbative dynamics relax back to the basal dynamics of wakefulness or deep sleep after the offset of perturbation, we measured the alterations in the level of integration over time (see Fig. 3.1D).

In more detail, we first computed the integration for 200 s of the simulated unperturbed basal cases, and detected the maximal and minimal values, I_{\max}^{basal} and I_{\min}^{basal} , for each brain state (see Fig. 3.3, red lines). Then, we perturbed the system and computed the integration for 200 s after the offset of perturbation, averaged across 3000 trials. The values I_{\max}^{basal} and I_{\min}^{basal} were used as the criterion for reaching the basal values for the synchronization and for the noisy perturbative protocols, respectively. The PILI was obtained by normalizing the extrema of I to 1 at the offset of perturbation (i.e. for $t = 0$) and 0 at the point where the integration reaches the basal values and calculating the integral of that curve. Larger values of this integral mean longer latency of extinction of the perturbative effects and smaller values indicate shorter latencies. The process is sketched in Figure 3.1. Significance levels were estimated over the 3000 trials over 200 repetitions thereof, calculating the mean of the distribution and estimating the error.

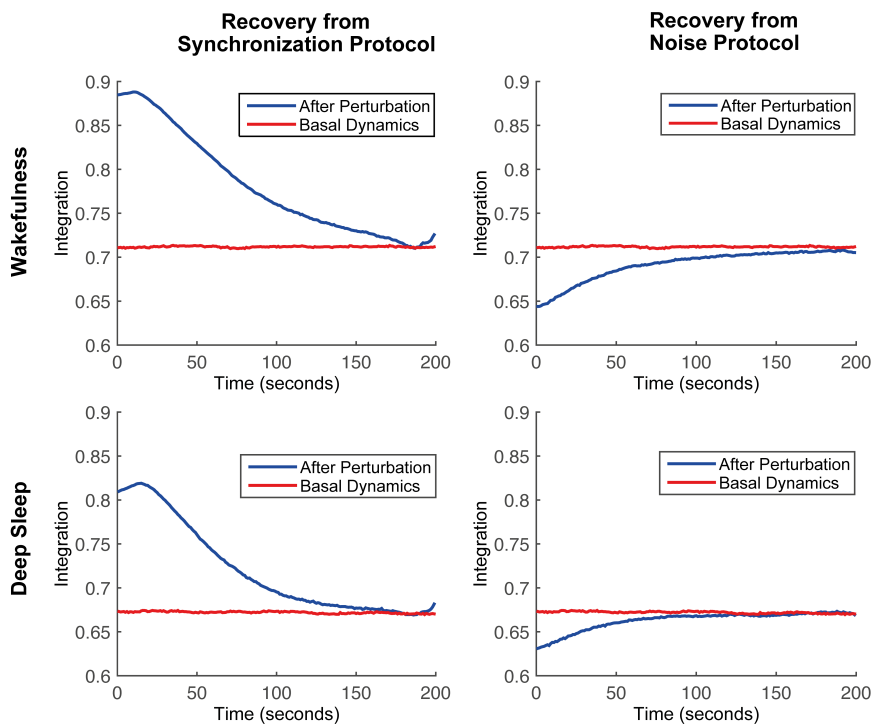


Figure 3.3: **Response to perturbation in silico for wakefulness and deep sleep.** Blue lines: Responses in the level of global integration after 10 random brain areas were perturbed using the synchronization protocol (left column) or the noise protocol (right column) during wakefulness (top line) and deep sleep (bottom line) averaged over 3000 trials. Red lines: Baseline levels of integration in the unperturbed simulated dynamics, different for wakefulness (top) and deep sleep (bottom). Once perturbation is halted (at $t = 0$ s), the integration slowly decays (left) or rises (right) towards the baseline values of each state (see Section 3.2.9 for details). For the purpose of illustration, the results are shown for the Frankfurt dataset only, but similar plots were obtained with the Liège dataset.

3.3 Results

We investigated the differences between two brain states, wakefulness and deep sleep, in healthy human participants from 2 independent previously published studies using a new offline perturbative approach in which we focused on the latency that the system takes to recover back to baseline after the offset of a strong multifocal perturbation applied offline.

3.3.1 Optimal working point

As a first step, the whole-brain computational model was adjusted to the baseline activity of each brain state recorded with fMRI in each study (see Section 3.2.6). In Figure 3.2 (red lines) we show how the global coupling parameter G was adjusted such that the mean degree of synchronization in simulated BOLD signals matched the ones measured empirically in each brain state and in each dataset. We found that this match – i.e. when the difference between the mean synchronization levels reaches zero (red lines) – occurred for a very specific value of G , which was consistently lower in deep sleep than wakefulness for both datasets. This result goes in agreement with previous findings suggesting that functional connectivity at the level of the BOLD signals is stronger during wakefulness than deep sleep (Jobst et al., 2017). In addition, we show in Figure 3.2 (black lines) the correlation between the empirical and simulated FC matrices as a function of G . This measure, however, is less constrictive since a good fit is obtained not only for the optimal G determined above but also when the simulated BOLD signals highly differed from the real ones in terms of phase synchronization.

3.3.2 Perturbation of whole-brain dynamics

Once we obtained a representative model of the whole-brain dynamics of each brain state, i.e. a Wakefulness Model and a Sleep Model (adjusted to each dataset), the models were perturbed offline following two distinct perturbation protocols in which we induced either more synchronization or more noise in 1-10 random brain regions for 100 seconds (see Section 3.2.7). After perturbation was stopped, we measured the perturbation-elicited changes in terms of global integration, which captures the brain-wide connectedness of BOLD signals in terms of phase locking (see Section 3.2.8)

(Deco et al., 2015; Lord et al., 2017).

In Figure 3.3, we show the evolution of integration (averaged over 3000 trials) right after the perturbation of 10 random brain areas (blue lines) compared to the basal condition (red lines) for each model and for each perturbation protocol. Notably, the basal integration was consistently higher during wakefulness (red line, top plots) than during sleep (red line, bottom plots), which means a higher connectedness at the level of BOLD signal phases during unperturbed wakefulness. At the offset of a long-lasting perturbation, i.e. at $t = 0$ (blue lines), the levels of integration were strongly deviated from the baseline, with increased integration after the synchronization protocol (left plots) and decreased integration after the noise protocol (right plots). During the recovery period, the levels of integration slowly decayed (or rose) towards their corresponding basal levels lasting on average more than 100 s to fully recover. Importantly, we found that each brain state, here wakefulness and sleep, recovered differently after being submitted to the same perturbation protocols.

3.3.3 Higher latencies after perturbation during wakefulness

To characterize the recovery after a long-lasting perturbation, we defined the Perturbative Integration Latency Index (PILI), which can be interpreted from Figure 3.3 as the area between the normalized red and blue curves. To capture only the recovery dynamics in the PILI, the curves of perturbed integration were normalized such that $I(t_0) = 1$ at the offset of perturbation, irrespective of the brain state, and $I = 0$ at the point where the integration reached the basal values. We calculated the PILI for each brain state and each perturbation protocol with varying number of perturbed areas. In Figure 3.4, we show the values of PILI as a function of the number of brain regions perturbed, for each brain state and synchronization protocol. Importantly, for both datasets, we found consistently higher PILI values for wakefulness than for sleep, with significance $p < 10^{-5}$, irrespective of the number of nodes perturbed. This result shows that two brain states, here wakefulness and deep sleep, can be dissociated based on their dynamical response to a strong long-lasting perturbation, which is efficiently characterized using the PILI. Whether the perturbation acts on promoting or disrupting synchronization, the

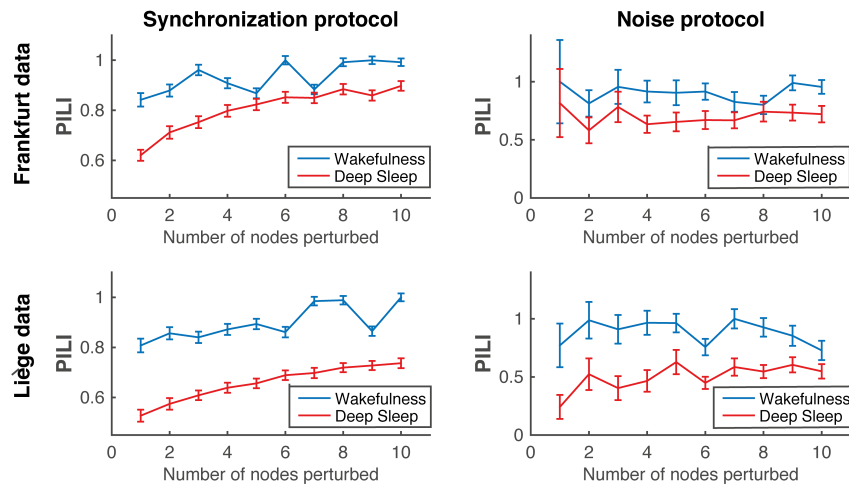


Figure 3.4: **Slower recoveries in the Awake model compared to the Sleep model following systematic perturbation reveal critical slowing down of the network dynamics.** Mean PILI values obtained in the awake (blue) and deep sleep (red) models as a function of the number of random brain regions perturbed, for each dataset and perturbation protocol. Larger PILI values correspond to slower recovery rate. Error bars represent the standard error of the mean over 200 repetitions of the 3000 trials. We found clear significant differences in PILI values between wakefulness and deep sleep, with p -value $< 10^{-5}$, in both datasets and synchronization protocols.

recovery is consistently longer during wakefulness as compared to deep sleep.

3.4 Discussion

In this chapter we presented a novel methodological approach designed to investigate the dynamical complexity of brain states through their recovery from strong long-lasting perturbations using the PILI. This approach has the potential to significantly expand our understanding of the dynamical complexity underlying different conscious and unconscious states. Our results show that the PILI efficiently dissociated two brain states, here wakefulness and deep sleep, with significantly higher PILI values in wakefulness in both datasets and perturbation protocols, regardless of the number of areas perturbed. Overall, these results show that a shift in the dynamical regime of the brain – induced by a change in the global coupling weight potentially linked to cholinergic levels (Deco et al., 2014) – turns the brain more rigid to external perturbations during deep sleep, returning faster to its equilibrium dynamics, whereas during wakefulness the brain integrates perturbations in the dynamics for longer. Theoretically, these results express the critical slowing down of a system when it is shifted away from an equilibrium point (Wissel, 1984; van Nes and Scheffer, 2007), in line with previous EEG studies showing that sleep is characterized by dynamical stability and loss of complexity (Pereda et al., 1998).

Importantly, all perturbations in this work are applied offline to a whole-brain computational model, which allows eliciting strong unnatural deviations from the basal activity with recoveries lasting more than a hundred seconds. The model is previously adjusted to the basal activity recorded with fMRI in each brain state, here wakefulness and deep sleep, resulting in two distinct models representative of each unperturbed brain state (Jobst et al., 2017). These models can then be exhaustively perturbed in silico without the ethical and safety constraints of in vivo perturbations (Clausen, 2010; Kringelbach and Aziz, 2011). Previous studies have used whole-brain computational models to simulate the effects of structural lesions, i.e. by removing links or nodes, and studying its impact in whole-brain dynamics (Cabral et al., 2012; Váša et al., 2015; Aerts et al., 2016; Deco et al., 2017c). In particular, it has recently been shown that the removal of specific binding regions impacts subsequent brain activity, specifically in terms of integration and information encoding capability (Deco et al., 2017c). Rather than removing regions, we perturbed regions by making them either more oscillatory or more noisy and measured the recovery of the system’s global integration. Other studies

have recently started to locally perturb models of resting-state activity to investigate their response to stimulation, particularly focusing on the activation/stabilization of meaningful functional networks in task (Cocchi et al., 2015; Spiegler et al., 2016; Gollo et al., 2017). Yet the strategy presented herein differs from previous offline stimulation approaches because it does not aim to simulate natural perturbative interventions (pathological or not) but rather to further investigate why brain states can be dissociated based on their response to perturbations, revealing important features of their dynamical complexity.

The introduction of our novel method for revealing the dynamical complexity following systematic perturbation is complementary to the seminal work of Massimini and colleagues who have used TMS with EEG for characterizing different conscious brain states (e.g. wakefulness, sleep and anesthesia) (Massimini et al., 2005; Ferrarelli et al., 2010; Casali et al., 2013). In contrast to this previous method, which uses brief TMS pulses and thus measures the weak perturbation-elicited dynamics, our approach measures the recovery after the offset of a long-lasting perturbation. Moreover, since the perturbation-evoked activity is influenced by fluctuations in spontaneous brain activity present at the time of perturbation, we reduce the effect of such fluctuations by strongly deviating the dynamics from the basal activity through a substantial long-lasting perturbation – only possible in a computational model – and then measuring the recovery from this perturbation over 3000 trials.

Following a growing trend in the analysis of dynamic BOLD signal connectivity, we consider only the coupling at the level of BOLD phases (Glerean et al., 2012; Cabral et al., 2017; Deco et al., 2017a). Measuring changes in phase space allows for a better characterization of the rich BOLD signal dynamics and any changes arising from perturbations. In particular, this makes it possible to directly determine the global level of synchronization across the whole brain, to obtain the phase locking matrices at the instantaneous level and derive the global level of integration over time (Deco et al., 2015). This reduction to phase space relies on the fact that the non-linear brain dynamics share more features with the non-linear phenomena observed in the waves and turbulence of the ocean than with that of a sedate pond, which can be characterized solely with amplitude measurements. The fundamental idea behind our hypothesis is that a strong perturbation to the turbulent ocean of brain activity elicits

alterations in phase (rather than amplitude) space.

There are a number of limitations to our analysis that deserve mention. First, we have modeled directly the hemodynamics with a Hopf normal form model, which presupposes that the temporal scale of hemodynamics can be represented solely by the slow fluctuations of neuronal activity inherent in fMRI time series. Second, we are characterizing the stability (or complexity) of coupled dynamical units – not the neuronal dynamics generating brain signals. Practically, this means that we have shown that changing the global (symmetric) coupling parameter G of coupled Hopf units induces a shift in the dynamical regime of the model, which changes its global stability (i.e. complexity). The importance of this observation has been motivated by previous results showing that the global coupling required to emulate sleep and waking functional connectivity in empirical data also changes (Jobst et al., 2017) (see Chapter 2).

But the link between the empirical and the simulated dynamics does not rest solely upon global coupling. It is equally important to consider the role of specific BOLD frequencies, as the ones within the most meaningful resting-state narrow-band. We found a wider distribution of BOLD frequencies during sleep (see Figures B.1 and B.2 in Appendix B), which, in a network model, allows for increased segregation and lower integration. As such, the lower BOLD integration levels in the baseline sleep model are likely to be a combination of both the weaker coupling strength and the wider frequency distribution obtained from empirical data. Here, we show that these two features of brain dynamics shift the model's dynamical regimes into different levels of baseline integration, which may be directly or indirectly related to different states of consciousness. Yet, other ingredients and features certainly play a role in regulating the dynamical complexity of different brain states, namely the asymmetric, region-specific and context-sensitive coupling in real brains. Since our methodological approach is not exclusive to the Hopf model used herein, it will be interesting in future work to fit more realistic models of effective connectivity to empirical data and pursue a more detailed characterization along the lines above.

Here we exposed two dynamical features inducing changes in the complexity of brain activity while the underlying network structure remained intact,

namely the global coupling strength and the intrinsic ultraslow frequency of each brain area. From an analytic perspective, recent studies on the stability and controllability of the human brain's structural connectivity matrix have made significant achievements in relating the dynamical complexity with the underlying network architecture (Gu et al., 2015; Betzel et al., 2016), in particular under artificial stimulation (Muldoon et al., 2016). Thus, such analytical studies in combination with the insights obtained from numerical simulations have the potential to become important tools for the development of personalized stimulation protocols.

Overall, *in silico* perturbations of whole-brain dynamics open up for a new level of artificial perturbative studies unconstrained by ethical limitations allowing for a deeper investigation of the dynamical properties of different brain states. To introduce the model, we restricted our analysis to two healthy brain states, wakefulness and sleep, but it would be important to test the method on other natural or pathological brain states such as vegetative coma, minimal conscious state, locked-in syndrome and various levels of anesthesia (Casali et al., 2013; Deco and Kringelbach, 2014) or in altered states elicited by drugs such as morphine, amphetamines, psilocybin and LSD (Carhart-Harris et al., 2014), which will be covered in Chapter 4.

3.5 Conclusion

In this chapter we have presented a novel approach for studying the underlying dynamics of different brain states. The here described Perturbative Integration Latency Index (PILI) characterizes the dynamical stability of brain states in terms of their recovery following *in silico* perturbation. After perturbing the whole-brain computational model by shifting it away from its basal state either into a synchronous or a noisy regime, the recovery of the system back to the equilibrium state is evaluated applying the PILI. We have shown that this novel measure can efficiently dissociate between the two analyzed brain states (wakefulness and slow-wave sleep), with significantly higher PILI values in wakefulness as compared to sleep. This result could be reproduced in two independent datasets and with both perturbation protocols. The here presented results show that a shift in the global brain dynamics causes the brain to be less affected by external perturbations during deep sleep as compared to wakefulness, returning faster to its equilibrium state after a strong model perturbation. The approach presented in this chapter opens up for a new level of artificial

perturbative studies, making it possible to study the underlying dynamics of different brain states in ways not possible experimentally.

Beyond the dissociation between brain states via massive perturbation protocols, the perturbative approach proposed herein offers a new strategy for effectively introducing probabilistic causality into neuroimaging studies and may be modified to further explore the minimal perturbation necessary to induce a significant dissociation between states, or to evaluate the efficacy of different perturbation protocols applied to different target regions. By offering the possibility to causally perturb a whole-brain computational model that fits human empirical neuroimaging data, this method could become a tool for determining where efficacious perturbation might help rebalance the dynamical complexity of the brain (Kringelbach et al., 2011; Saenger et al., 2017). It may therefore be useful in clinical contexts for predicting the outcome of DBS or TMS for specific disorders, perhaps even at the individual level.

Characterizing the psychedelic state through perturbation of whole-brain dynamics

This chapter introduces work in preparation for submission as an original research article: *A perturbational approach for characterizing the dynamics underlying the psychedelic state*. Beatrice M. Jobst, Selen Atasoy, Adrián Ponce-Alvarez, Ana Sanjuán, Leor Roseman, Mendel Kaelen, Robin Carhat-Harris, Morten L. Kringelbach, Gustavo Deco.

Lysergic acid diethylamide (LSD) is a potent psychedelic drug, which has seen a revival in clinical and pharmacological research within the last years. Human neuroimaging studies have shown fundamental changes in brain-wide functional connectivity and an expansion of dynamical brain states, thus raising the question about a mechanistic explanation of the dynamics underlying these phenomena. We here applied a novel perturbational approach, presented in Chapter 3, based on a whole-brain computational model, which opens up the possibility to externally perturb different brain nodes *in silico* and thus investigate differences in dynamical complexity of different brain states. After adjusting the whole-brain model to the dynamics of fMRI BOLD signals recorded under the influence of LSD or Placebo, perturbations of different brain areas were simulated by introducing either more synchronization or more noise into the regarding node. After perturbation offset we quantified the recovery of the brain node to its basal dynamical state with the Perturbational Integration Latency Index (PILI) and used this measure to distinguish between the two brain states. We

found significant changes in dynamical complexity, showing consistently higher PILI values after LSD intake on a global level, indicating a shift of the brain's global working point further away from a stable equilibrium as compared to normal conditions. On a local level we found that the highest differences were located within the limbic network, the visual network and the default mode network, confirming results of previous experimental studies. Additionally we found changes in the hierarchical organization of the brain between the two states, exhibiting stronger hierarchy under LSD. The here presented results provide important new insights into the brain-wide dynamical changes underlying the psychedelic state and underline possible future clinical applications of psychedelic drugs in particular psychopathological states.

4.1 Introduction

In the past few years we have witnessed an increasing interest in the study of the effects of psychedelic drugs, especially lysergic acid diethylamide (LSD), on the human brain. LSD is a potent psychoactive drug, which was first synthesized in 1938 and whose hallucinogenic effects were discovered in 1943 (Hofmann, 1980). Between the 1950s and the late 1960s LSD was widely used in psychology and psychotherapy and its clinical applications as a pharmacological substance were well studied (Passie et al., 2008; Nichols, 2016). Due to political reasons because of its widespread uncontrolled recreational use, LSD was made illegal in the late 1960s, which is why human research with LSD came to a halt for approximately 50 years. It was not until recently, that the drug has lived a renaissance in clinical and especially brain research.

Within the last years a significant number of human neuroimaging studies have been performed to study the psychedelic state (Carhart-Harris et al., 2012; Muthukumaraswamy et al., 2013; Tagliazucchi et al., 2014; Palhano-Fontes et al., 2015; Carhart-Harris et al., 2016b; Tagliazucchi et al., 2016c; Preller et al., 2017a,b), reporting an increase in visual cortex blood flow and an expanded visual cortex functional connectivity, a reduction of the integrity of functional brain networks, a global increase in connectivity between networks and an enhanced repertoire of dynamical brain states.

While these results offer us valuable insights into the major functional alterations taking effect in the brain during the psychedelic state, we are still missing a mechanistic understanding of these empirical observations providing us information about the underlying whole-brain dynamics.

To address this problem, we here apply a novel method combining a whole-brain computational model with an *in silico* model perturbation, previously described by Deco et al. (2018), where it is possible to simulate external perturbations of any brain region for an unlimited amount of time in ways not possible experimentally (see Chapter 3).

In the last 15 years there has been a number of studies investigating brain function by systematically exploring the dynamical responses to controlled artificial external perturbations of different brain regions and combining them with whole-brain neuroimaging (Massimini et al., 2005; Kringelbach et al., 2007a; Litvak et al., 2007; Mohseni et al., 2012; Casali et al., 2013; Saenger et al., 2017). These approaches are limited though to transcranial magnetic stimulation (TMS) in healthy human subjects and to deep brain stimulation (DBS) in patients due to ethical considerations (Siebner et al., 2009; Clausen, 2010; Kringelbach and Aziz, 2011). In addition to that, these procedures are usually costly and expensive to perform.

Here we apply a novel *in silico* model perturbation approach, introduced in Chapter 3, to study the perturbation-elicited changes in global and local brain activity and to obtain a deeper understanding of the mechanisms underlying the experimentally observed dynamical brain changes under the influence of LSD in different conditions (rest and while listening to music). This approach is based on a whole-brain model, described in Section 1.4.2 in Chapter 1, directly simulating the resting-state BOLD signal fluctuations (Clausen, 2010; Deco et al., 2017b; Jobst et al., 2017; Saenger et al., 2017; Deco et al., 2018), which we perturb systematically on a node-by-node level. Based on the above described experimental insights on LSD and on the recent application of this approach to human neuroimaging sleep data, where the decay after perturbation was found to be faster during sleep than during awake (Deco et al., 2018), we expect that under the influence of LSD the system would take longer to regain baseline activity after a strong model perturbation, which is consistent with more complex and less stable dynamics (Deco et al., 2018). We further expect this predicted observation to be even stronger in the Music condition, where the effects of LSD have been found to be amplified (Kaelen et al., 2015, 2016; Preller et al., 2017a). The expected results could be related to a shift in the dynamical working regime of the brain in the LSD state, consistent with previously described results, like globally increased connectivity, an enhanced repertoire of brain dynamical states and closeness to criticality (Tagliazucchi et al., 2014; Carhart-

|

|

Harris et al., 2016b; Tagliazucchi et al., 2016c; Atasoy et al., 2017b).

We furthermore analyze the differences between LSD and Placebo induced brain states by comparing the perturbation-elicited dynamical responses on a resting-state network level, where we hypothesize to find larger differences in brain sub-networks experimentally known to be relevant for the LSD state. Finally we introduce an index for hierarchical information processing in the brain, and evaluate eventual differences between the LSD and Placebo states, expecting to find higher hierarchical organization under the influence of LSD.

4.2 Methods

4.2.1 fMRI data

For the fMRI BOLD data, 20 healthy participants were scanned in 6 different conditions: LSD resting-state, Placebo (PCB) resting-state, LSD and PCB while listening to music, and LSD and PCB resting-state after listening to music. All participants gave informed consent. The experimental protocol was approved by the UK National Health Service research ethics committee, West-London. Experiments conformed with the revised declaration of Helsinki (2000), the International Committee on Harmonization Good Clinical Practice guidelines and the National Health Service Research Governance Framework. The data collection was sponsored by the Imperial College London, which was carried out under a Home Office license for research with schedule 1 drugs. 8 out of the 20 subjects needed to be excluded from further analyses for the following reasons: the scanning session of one participant needed to be terminated early due to the subject reporting significant anxiety. 4 participants were excluded due to high levels of head movement (as described in the original publication by Carhart-Harris (Carhart-Harris et al., 2016b) the exclusion criterion for excessive head movement was subjects displaying more than 15% scrubbed volumes with a scrubbing threshold of $FD = 0.5$). 3 participants needed to be excluded due to technical problems with the sound delivery in the Music condition. Thus, 12 subjects were considered for further analyses. Each participant received either 75 μg of LSD (intravenous, I.V.) or saline/placebo (I.V.) 70 minutes prior to MRI scanning. LSD and PCB sessions were separated by at least 14 days with the condition order being balanced across participants, who were blind to this order.

The fMRI BOLD data were recorded using a gradient echo planar imaging sequence, $TR/TE = 2000/35$ ms, field of view = 220 mm, 64×64 acquisition matrix, parallel acceleration factor = 2, 90° flip angle. The exact length of each of the two BOLD scans per participant was 7:20 minutes. BOLD signals were averaged over cortical and sub-cortical regions of interest following the automated anatomical labeling (AAL) atlas parcellation of the brain into 90 regions of interest (76 cortical and 14 subcortical regions, AAL90), comprising 45 regions in each hemisphere (Dang-Vu et al., 2005). The full details on the study design, the scanning protocol and the fMRI pre-processing can be consulted in the supplementary information of the original publication (Carhart-Harris et al., 2016b).

4.2.2 Anatomical connectivity

The anatomical connectivity data between the different brain areas applied in this study has already been described in various publications (Deco et al., 2017a; Jobst et al., 2017; Deco et al., 2018) and was the same as used in Chapters 2 and 3 (see Sections 2.2.2 and 3.2.3) for basing the interactions between the distinct brain areas of the whole-brain network model on.

4.2.3 Hopf computational whole-brain model

The whole-brain computational model which was used in this study to simulate the empirical dynamics observed in the two different drug states matches the models applied in the previous chapters (see Section 2.2.7 in Chapter 2, Section 3.2.5 in Chapter 3 and Section 1.4.2 in Chapter 1 for a detailed description of the model). Again, as in Chapter 3, only the global coupling parameter G was adjusted to the empirically observed dynamics, while the bifurcation parameter a was set to 0 corresponding to the bifurcation point of the model, the transition point between noisy and oscillatory behavior.

4.2.4 Functional connectivity estimation

After detrending and demeaning, the BOLD signals were band-pass filtered within the range of 0.04-0.07 Hz following the procedure applied in Chapters 2 and 3 (see Sections 2.2.4 and 3.2.4) (Glerean et al., 2012), since this frequency band has been shown to be less affected by noise and to be more functionally relevant compared to other frequency bands (Biswal et al., 1995; Achard et al., 2006; Buckner et al., 2009; Glerean et al., 2012). Next, after z-scoring the filtered time series, the FC matrices were first calculated for each participant in each condition and then averaged over groups applying fixed-effect analysis (see Sections 2.2.4 and 3.2.4 in Chapters 2 and 3). Thus we obtained 6 final FC matrices, one for each condition. For comparing the group level FC matrices between the LSD and PCB conditions, we compared the mean FC values among drug induced states for each LSD – PCB condition pair (i.e. Rest, Music and Rest after Music). To test the significance of the differences of the conditions, we generated 100 surrogate datasets, applying the same strategy as in Chapter 2 (see Section 2.2.3), where the LSD and PCB conditions were randomly permuted with a 50% chance of switching of the condition assignment. This way, the group pairs get randomly mixed and thus fulfill the null hypothesis of no difference between drug induced conditions.

4.2.5 Fitting the model to experimental data

We explored the parameter space of the whole-brain computational model by varying the global coupling strength parameter G from 0 to 2 in steps of 0.01, similar to the procedure explained in Chapters 2 and 3 (see Sections 2.2.8 and 3.2.6). To match the procedure applied on the empirical data, we filtered the simulated BOLD time series as well in the range of 0.04-0.07 Hz. Furthermore the signal lengths of the simulated data coincided with the duration of the empirical data recordings. Next, the FC matrix was estimated on the simulated data for the whole parameter space applying the same procedure as on the empirical data. As a consequence we calculated the fitting between the empirical and the simulated FC matrices for each LSD – PCB condition pair (i.e. Rest, Music and Rest after Music) for the whole parameter space as the Kolmogorov-Smirnov distance (KS distance) between the two matrices, amounting in one fitting value per parameter value G for each condition. We simulated the BOLD time series and fitted them to the empirical data under the same conditions 50 times and averaged subsequently over the final results in order to minimize the random effects due to the Gaussian noise present in the model. We compared the resulting fitting curve minima to the surrogate data explained above in order to test for significant differences between the LSD and PCB conditions. The coupling parameter values where the fitting curves were minimal were then used for the following analysis steps.

4.2.6 Model perturbation protocols

Following the procedure applied in Chapter 3 (Deco et al., 2018), we made use of the locally defined bifurcation parameter a of the Hopf model to simulate two kinds of offline perturbation protocols evoking either deviations from the basal state ($a = 0$) into the synchronous regime ($a > 0$) or into the noisy regime ($a < 0$). In order to investigate the local effects provoked by the perturbation of single brain areas, we perturbed one node at a time repeating this procedure 3000 times so that finally we could average over the 3000 trials and perform statistical analyses based on the error of the distribution. One perturbation trial consisted in perturbing one out of 90 nodes for 100 seconds by setting its local bifurcation parameter value a to either $a > 0$ or $a < 0$. Specifically, for the synchronization perturbation protocol a was set to 0.6 and for the noise perturbation protocol to -0.6. This leads in the synchronization case to more oscillations in the perturbed node and in the noise case to an artificial destruction of

the basal synchronization between the perturbed node and the other brain areas. After perturbation, the bifurcation parameter was reset to zero in the perturbed node.

The procedure applied herein is very similar to the one explained in the previous chapter in Section 3.2.7 with the difference that here we mainly focus on the local effects by perturbing only one node at a time while leaving the other nodes at their basal state ($a = 0$). A similar procedure has been performed by Deco et al. (2018) (Fig. 5), where the node-wise perturbations were correlated with various node-wise metrics, but no details about the local effects of node-wise perturbation differences were analyzed.

4.2.7 Integration measure

In order to measure the level of brain-wide simulated BOLD signal interactions over time, we applied the integration measure described in Chapter 3 (see Section 3.2.8), which characterizes the level of integration across all brain regions for each time point (Deco et al., 2015, 2018). As in the previous chapter, we computed the integration over 200 seconds of simulated BOLD time series in the basal state and starting at perturbation offset in the perturbed case.

4.2.8 Perturbative Integration Latency Index (PILI)

To characterize the return of the brain dynamics to the basal state after a model perturbation of the system we calculated the Perturbative Integration Latency Index (PILI) (Fig. 4.1). As in the previous chapter in Section 3.2.9 we used the changes of the level of integration over time from the basal dynamics to the perturbed state.

First, the integration was calculated for 200 seconds of the simulated basal state (orange curve in Fig. 4.1), the average over 3000 trials was calculated and finally the maximum and minimum values of the averaged curve were identified. This was done for each of the 6 conditions. Then, the system was perturbed following the procedure described above and again the integration was computed over 200 seconds after the offset of the perturbation. This procedure was performed 3000 times. The maximum and minimum values of the basal integration curve were used to determine the moment of recovery after the model perturbation, for the synchronization and noise protocol, respectively. Then, the PILI was calculated as the integral of the integration curve from perturbation offset to the reaching point of the

basal state. Finally, we computed the average PILI over trials to obtain one final value for each brain area. The PILI gives us information about how strong the system reacts to a model perturbation and how long it takes for it to regain its basal dynamical state. The statistical significance tests were performed across the 3000 trials applying a Mann-Whitney U test to compare between the drug and PCB induced states.

The here described procedure for calculating the PILI, was adopted from Chapter 3 (see Section 3.2.9) (Deco et al., 2018), with some slight differences. First of all, in this study the integration curves were not normalized between 0 and 1 after perturbation offset until reaching baseline. As a consequence not only the time it takes for the integration curve to reach the basal state after a model perturbation is taken into consideration, but also how strong it deviates from the baseline in the first place. We found that this was an equally important feature, since a perturbation with the same strength can cause a much stronger deviation from the basal state depending on the brain state.

Second, here we averaged over trials only *after* calculating the PILI values for each trial as the integral of the integration curve (see Fig. 4.1 as compared to Fig. 3.1D in Chapter 3). Thus it was not necessary to repeat the 3000 trials various times in order to calculate the statistical significance levels, but the 3000 trials could be used directly to test for significance. This simplification procedure was possible in this study, since, in contrast to the previous chapter, here we only perturbed one node at a time, thus making various trials to vary the randomly picked nodes irrelevant.

4.2.9 Region-wise and resting-state network analysis

The above described procedure resulted in one PILI for each of the 90 brain areas. We compared the p-values between all brain regions for each of the 3 conditions (Rest, Music, Rest after Music), computed with the above described statistical significance test, by ordering them from smallest to largest. Bonferroni correction was applied in order to correct for the number of brain areas, meaning that a p-value had to be lower than $0.05/90 \approx 5.556e - 04$ to be significant.

Next, we evaluated the differences between PILI values in seven commonly observed RSNs, default mode, executive control, dorsal attention, ventral attention, visual, limbic and somato-motor network, as described in Thomas Yeo et al. (2011). The parcellation of the cerebral cortex into

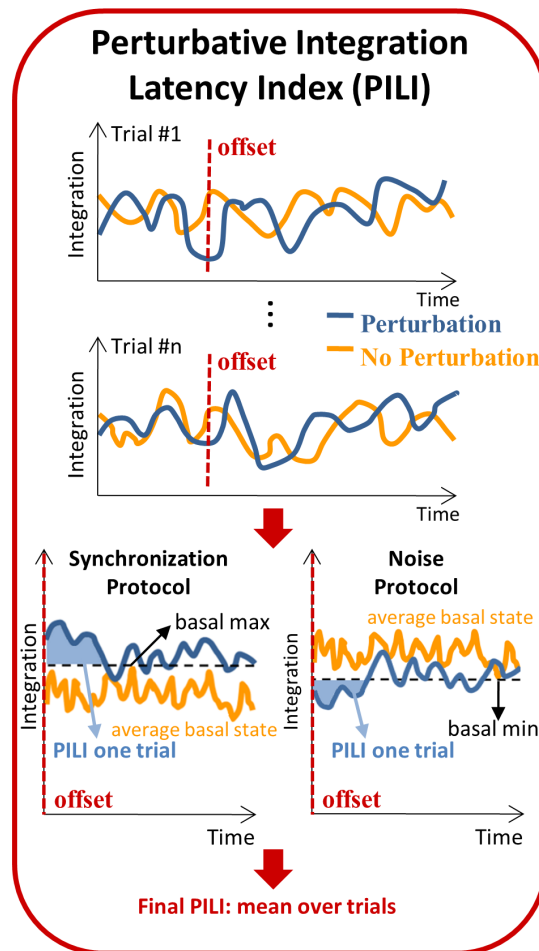


Figure 4.1: **Calculation of the Perturbative Integration Latency Index (PILI)**. For each trial, the PILI was computed as the integral of integration values after the offset of the model perturbation (blue) until reaching the maximum or the minimum of the basal state (orange). The final PILI was obtained by averaging over trials. The PILI characterizes the return of the brain dynamics to the basal state after a model perturbation of the system.

these seven networks has been extracted from the intrinsic functional connectivity data from a group of 1000 participants (Thomas Yeo et al., 2011) and is available online at http://surfer.nmr.mgh.harvard.edu/fswiki/CorticalParcellation_Yeo2011. We computed for each reference RSN (Thomas Yeo et al., 2011; Atasoy et al., 2016) the standardized difference between LSD and PCB induced states by calculating Cohen’s d-values (Cohen, 1988) taking into account only those brain areas being part of one RSN. Cohen’s d-value is defined as follows (Cohen, 1988):

$$d = \frac{(\mu_1 - \mu_2)}{s_{\text{pooled}}}, s_{\text{pooled}} = \sqrt{\frac{(\sigma_1^2 + \sigma_2^2)}{2}}, \quad (4.1)$$

where μ_1 and μ_2 are the means of the PILI values within one RSN group and σ_1 and σ_2 the standard deviations of either group.

The RSNs were then ordered from highest to lowest Cohen’s d-value, where the higher the value, the higher the difference between PILI values and thus the higher the response to a model perturbation under the influence of LSD in one particular RSN.

4.2.10 Hierarchy index

Following the concept of Deco and Kringelbach (2017), we here introduce an index for the hierarchy of information processing in the brain, short hierarchy index, by making use of the variability of the PILI values over different brain regions. We thus define the hierarchy index as the standard deviation of the PILI values over brain nodes, implying that the higher the variability over nodes, the stronger the hierarchy. We calculated this index for each of the 3 conditions for the LSD and the PCB state for each of the 3000 trials and then compared the distributions over trials between LSD and PCB. We evaluated statistically significant differences between the LSD and PCB induced brain states applying a two-sided t-test.

4.3 Results

We investigated the differences between two drug-induced brain states in 3 different conditions, namely LSD and PCB during rest, LSD and PCB while listening to music and LSD and PCB during rest after listening to music. We applied a previously published offline perturbational approach based on a whole-brain model which characterizes the return of the brain dynamics to the basal state after a model perturbation of the system (see Chapter 3) (Deco et al., 2018).

4.3.1 Functional connectivity and optimal working point

First of all we looked at the differences in functional connectivity between LSD and PCB induced brain states in all 3 conditions. After filtering the data, the FC matrices were calculated on a subject-level basis, after which they were averaged over subjects within each condition. To analyze the differences between the LSD and PCB brain states, the mean FC value was computed for each condition and then compared to the surrogate data. We found a significant difference between the mean FC values in the Music condition (LSD: 0.204 ± 0.179 , PCB: 0.140 ± 0.197 ; p-value: 0.0297). We furthermore found a slight increase in mean FC values during the LSD state with respect to PCB in the other conditions as well (Rest: LSD: 0.186 ± 0.175 , PCB: 0.154 ± 0.202 ; Rest after Music: LSD: 0.181 ± 0.171 , PCB: 0.163 ± 0.191), which did not hold the statistical significance test, though (Fig. 4.2A).

Next, we fitted the Hopf whole-brain model to the data in each condition in order to compare between the two drug induced states with regards to their dynamical working point, being that the parameter region where the model fits the data best. The Hopf whole-brain model has been introduced in the previous chapters and has already been shown in several publications to be able to simulate fMRI BOLD network dynamics (Kringelbach et al., 2015; Deco et al., 2017b; Jobst et al., 2017; Deco et al., 2018). Furthermore it is especially well suited for simulating external perturbations to distinct brain nodes, as discussed in Chapter 3 and demonstrated in Deco et al. (2018). We computed the KS distance between the empirical and the simulated functional connectivity matrices and found a shift in the optimal global coupling parameter G , being that the minimal KS distance, to higher values under the influence of LSD in all 3 conditions (Rest: LSD: 0.31, PCB: 0.27; Music: LSD: 0.35, PCB: 0.25, Rest after Music: LSD: 0.29, PCB: 0.28) with a significant difference in the Music condition (p=0.0099) (Fig. 4.2B).

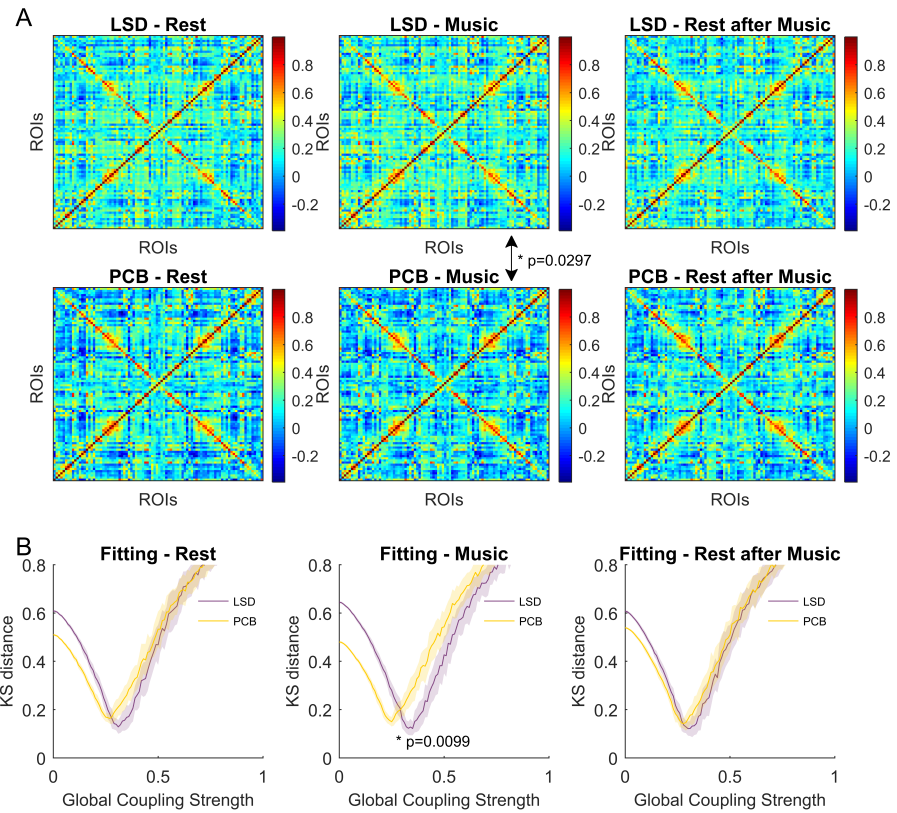


Figure 4.2: **Empirical functional connectivity and model fitting.** In A the functional connectivity matrices are shown for each of the 6 conditions. Significance tests have been performed between the LSD and PCB conditions resulting in a significant difference in the mean functional connectivity between the LSD and the PCB state in the music scanning session. In B the mean and standard deviation over 50 realizations of the KS distance between the empirical and the simulated functional connectivity matrices are shown for each condition as a function of the global coupling strength. The optimal fit corresponds in each condition to the minimal KS distance. We found a significant difference between the optimal fit in the LSD and the PCB state in the music scanning session.

As above, to assess statistical significance, the values were compared to surrogate data obtained by randomly permuting group assignments (see Section 4.2.4).

4.3.2 Global differences in integration

With the adjustment of the whole-brain model to the data, we obtained a representative model of the basal brain state for each condition and drug state. We then simulated two kinds of model perturbation protocols, by either shifting one brain node to a more synchronous state or to a more noisy state for 100 seconds (see Section 4.2.6). This was done for each of the 90 brain nodes. Immediately after perturbation, we quantified the perturbation-caused changes in brain-wide signal interactions over time by computing the global integration measure (see Sections 4.2.7 and 3.2.8 in Chapter 3).

In Fig. 4.3 the integration averaged over 3000 trials and all 90 brain nodes is displayed as a function of time. The integration is shown immediately after perturbation offset for each condition and drug state. The first thing to note is that the basal integration (black) was higher for each condition during LSD administration than for PCB, being this difference highest in the Music condition. This means that without perturbation the level of BOLD signal connectedness was higher in the LSD state than in PCB. It is also noteworthy that, comparing the basal integration among conditions within one drug state, the basal integration increased under the influence of LSD while listening to music, while in the PCB state it decreased with music. Regarding the perturbation protocols, we can observe that for all conditions the deviations from the basal activity were both stronger and longer lasting under the influence of LSD with respect to PCB after being exposed to the same kind of perturbation. While this is valid for both synchronization protocols (red) and noise protocols (yellow), we can already see that the effects on the differences in integration in the LSD state compared to the PCB state were much smaller for the noise protocol than for the synchronization protocol (detailed analysis in Section 4.3.3 and Appendix C). We therefore decided to mainly focus on the synchronization protocol for the rest of the study. The results of the noise perturbation protocol can be consulted in Appendix C.

Furthermore, we can again observe the differences in integration after perturbation among conditions within one drug state, where also after perturbation the integration increased in the Music condition for LSD, while during PCB it decreased.

Another interesting observation is that the differences between LSD and PCB were diminished in the Rest after Music condition. This is most likely due to the vanishing effect of LSD during the experiment, being this particular condition the last one in the sequence of experimental conditions

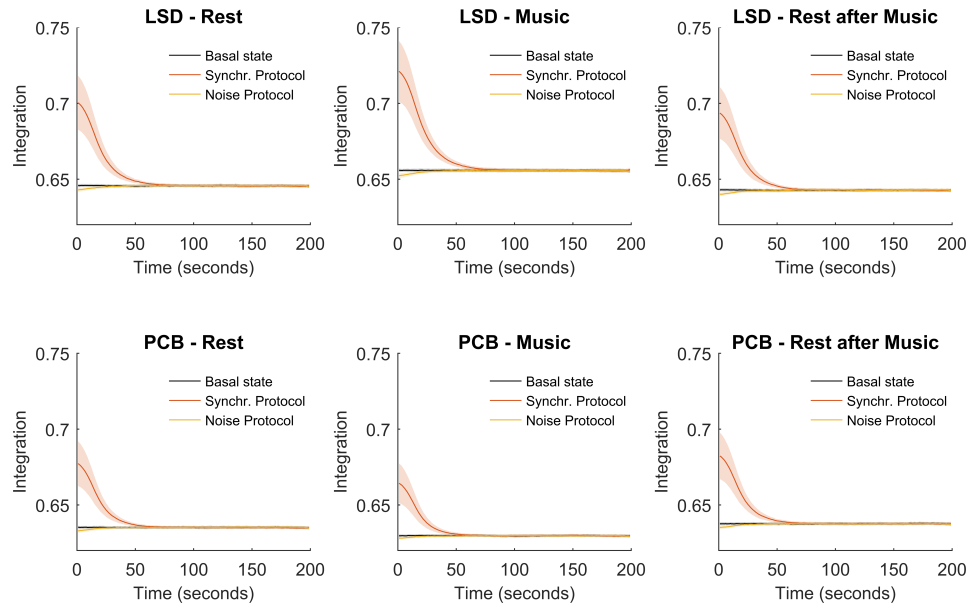


Figure 4.3: **Mean integration.** Here the integration averaged over trials and nodes and the standard deviation of the integration over nodes is shown as a function of time for each of the 6 conditions. In black the mean and standard deviation of the integration of the basal state are shown. In red and yellow the mean and standard deviation of the integration for the synchronization protocol and the noise protocol, respectively, are represented.

(Carhart-Harris et al., 2016b).

4.3.3 Global and local differences in Perturbative Integration Latency Index

In order to formally characterize the above observed phenomena of changes in the integration strength and duration of the return of the brain dynamics to its basal state after a model perturbation, we computed the Perturbative Integration Latency Index (PILI). We here defined the PILI as the area under the integration curve until it reaches the basal state. This way the PILI captures both strength of deviation from the basal state and duration of the recovery. The PILI was calculated for each node by only perturbing this specific node and leaving the other ones at their basal dynamics for 3000 trials, which were finally averaged in order to obtain one single PILI value for each brain area (see Section 4.2.8).

In Figure 4.4 we show the mean PILI for the synchronization protocol for

each condition for all 90 brain areas. We found consistently higher PILI values for the LSD induced brain state than for PCB in all 3 conditions, where the effect was strongest for the Music condition. Again, the effect was diminished in the Rest after Music condition, which is most likely due to the vanishing drug effect, as explained above. Most importantly, we demonstrate here, that the LSD and PCB brain states show very different dynamical responses to a model perturbation, being that the responses to the same perturbation are stronger and longer lasting under the influence of LSD with respect to PCB.

Similar results can be observed for the noise protocol (see Fig. C.1 in Appendix C). Also here we found a global increase in PILIs for LSD when compared to PCB for all 3 conditions.

Next, we looked at the PILI values on a node-to-node basis. We checked for statistical significance of the difference in the mean PILI value between LSD and PCB for each condition for each node applying a Mann-Whitney U test with Bonferroni multiple comparison correction to correct for the number of brain nodes. The results for the synchronization protocol are shown in Table 4.1, where the 20 brain areas with the highest PILI differences are shown in order from smallest to largest p-value. The ordering of the rest of the brain regions and the results for the noise protocol can be found in Tables C.1 and C.2 in Appendix C.

By ordering the brain regions by p-values for each condition, we can observe that globally p-values were much lower for the Music condition with respect to the other resting conditions, which confirms again the amplified effect of LSD while listening to music. The brain regions which were dominant in all 3 conditions, were the cingulate cortex areas, the precuneus, the gyrus rectus and the supplementary motor area. Other regions where high differences between LSD and PCB could be observed, were the calcarine sulcus, the olfactory sulcus, the superior frontal gyrus and the medial frontal gyrus, thalamus and hippocampus.

4.3.4 Relationship of PILI to resting-state networks

We were then interested in differences in the PILI values between LSD and PCB brain states on an RSN level. We assessed the differences in PILI values based on the synchronization protocol in seven reference RSNs – default mode, executive control, dorsal attention, ventral attention, visual, limbic and somato-motor network – by computing Cohen’s d-values, a standard-

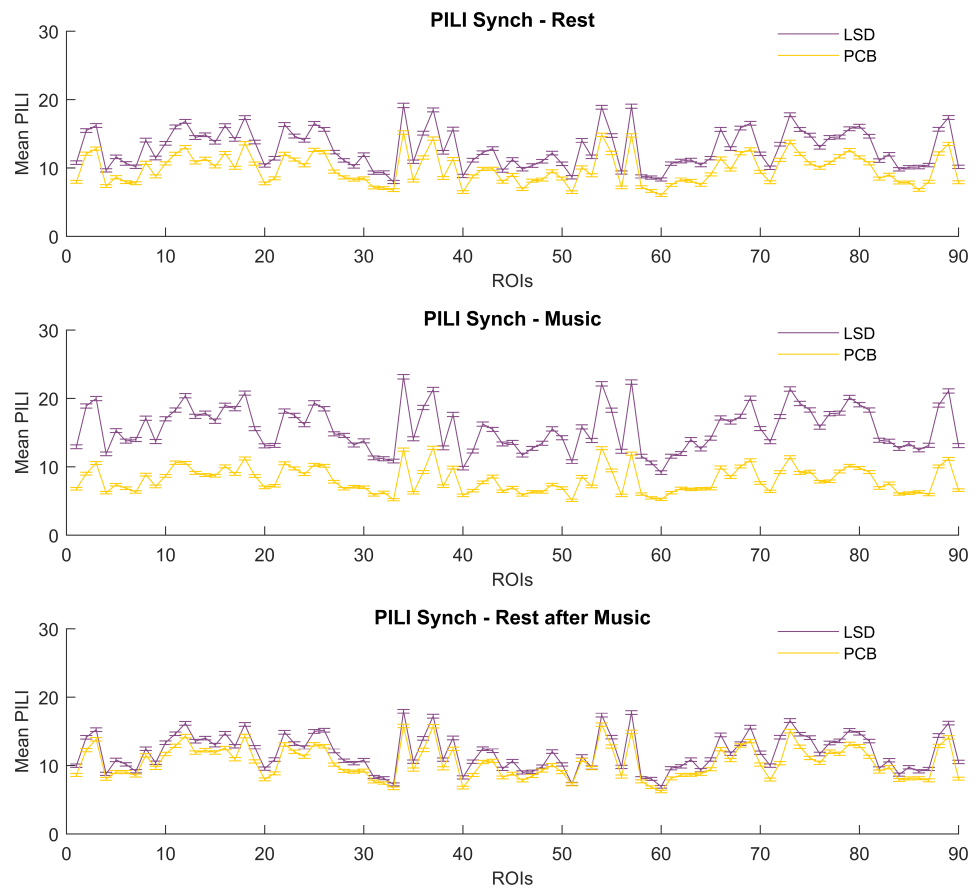


Figure 4.4: **PILI – Node level analysis.** Here the mean and the standard error of the mean of the PILI values over trials are shown for the synchronization protocol for each of the 3 conditions for the LSD and the PCB state for all 90 brain regions. We found that the global differences between the LSD and PCB induced brain states were amplified in the Music condition. Node-by-node analysis with corresponding p-values can be found in Table 4.1 and Table C.1 in Appendix C.

Table 4.1: Node level PILI differences.

Rest		Music		Rest after Music	
Brain region	p-value	Brain region	p-value	Brain region	p-value
Olfactory R	2,986e-37*	Cingulum Mid R	1,235e-172*	Hippocampus R	1,632e-34*
Thalamus L	2,695-36*	Precuneus L	2,205e-166*	Cingulum Ant R	2,200e-21*
Supp Motor Area R	4,742e-35*	Rectus R	2,930e-166*	Precuneus R	4,968e-18*
Cingulum Mid L	3,338e-33*	Frontal Sup Medial R	1,317e-159*	Precentral R	4,119e-15*
Calcarine L	1,413e-32*	Frontal Sup Medial L	3,682e-158*	Hippocampus L	7,243e-12*
Cingulum Ant R	1,803e-31*	Frontal Sup R	9,976e-157*	Supp Motor Area R	9,001e-12*
Occipital Sup R	9,135e-30*	Frontal Sup L	1,237e-156*	Occipital Mid L	3,359e-11*
Cingulum Post R	1,030e-29*	Precuneus R	1,676e-154*	Frontal Sup Medial R	5,164e-11*
Precuneus L	2,193e-29*	Cingulum Post L	5,073e-151*	Cingulum Mid L	6,657e-11*
Rectus L	3,739e-29*	Cingulum Mid L	4,485e-149*	ParaHippocampal R	7,575e-11*
Putamen L	4,219e-29*	Cingulum Post R	6,785e-149*	Rectus L	2,798e-10*
Thalamus R	8,444e-29*	Rectus L	2,748e-147*	Cingulum Ant L	9,305e-10*
Calcarine R	2,847e-28*	Caudate L	2,643e-144*	Frontal Sup R	3,584e-09*
Putamen R	2,857e-28*	Olfactory R	1,631e-139*	Fusiform R	3,615e-09*
Lingual L	3,515e-28*	Frontal Sup Orb L	1,256e-136*	Cingulum Mid R	4,108e-09*
Olfactory L	1,103e-27*	Frontal Med Orb R	1,221e-132*	Calcarine R	4,543e-09*
Precuneus R	1,119e-26*	Cingulum Ant R	5,574e-132*	Temporal Pole Sup L	1,097e-08*
Cingulum Post L	1,584e-26*	Supp Motor Area R	5,637e-131*	Frontal Mid Orb L	1,550e-08*
Frontal Sup Medial L	2,995e-26*	Cingulum Ant L	1,028e-130*	Precuneus L	2,142e-08*
Cingulum Ant L	3,867e-26*	Frontal Sup Orb R	5,134e-130*	Temporal Inf L	3,254e-08*

In this table brain nodes are ordered for each condition by p-values – from smallest to largest –, based on the PILI differences between LSD and PCB by perturbing each specific node at a time. Here the 20 regions with the smallest p-values are shown. The asterisk indicates statistically significant differences after Bonferroni correction.

ized difference measure, between LSD and PCB PILI values for each RSN. The results are shown in Figure 4.5, where the RSNs were ordered for each of the 3 conditions by Cohen’s d-values, showing in black-red the highest differences and in light-orange the lowest differences.

The most noticeable result is that in all 3 conditions the 3 RSNs with the highest PILI differences between the LSD and PCB state were the limbic, the visual and the default mode network, where the limbic network showed the highest differences in all 3 cases. In both resting-state conditions the visual network took the second most important position and the default mode network the third, where this order was switched in the Music condition. In both resting conditions the somato-motor network went to the fourth position, followed by executive control, ventral attention and dorsal attention networks in the first resting-state and ventral attention, executive control and dorsal attention networks in the second resting condition, respectively. In the Music condition the ventral attention network gained more importance in PILI differences between LSD and PCB and went up to position 4,

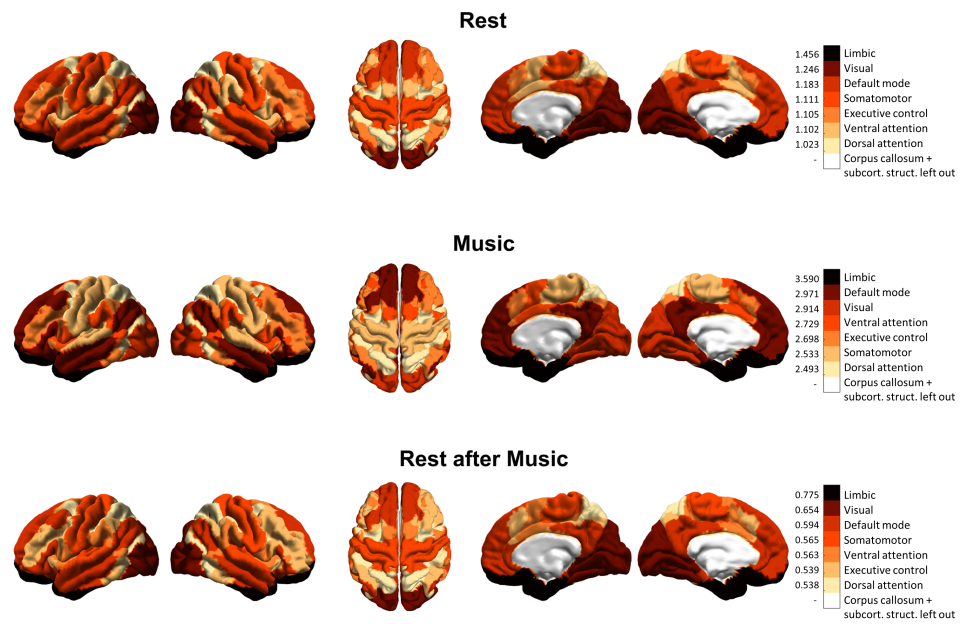


Figure 4.5: **PILI – RSN analysis.** Here the differences between the PILIs in LSD and PCB are shown on an RSN level for the synchronization protocol. For all the nodes forming part of one RSN the Cohen's d-value was calculated based on the mean and standard deviation over nodes in each state, indicating the standardized mean difference between the PILIs of each RSN in LSD and PCB. This was done for each of the 7 RSNs. The RSNs were ordered for each condition (Rest, Music, Rest after Music) by Cohen's d-values, showing in black-red the highest differences and in light-orange the lowest differences. The white area is to be discarded. Thus, the color-coding is in each condition a mere representation of the size of the Cohen's d-value with respect to the Cohen's d-values of the other RSNs in the same condition. This indicates that the darker the color representation of one RSN in one condition, the higher the PILI differences between LSD and PCB in the regarding RSN.

followed by executive control, somato-motor and dorsal attention networks.

4.3.5 Increased hierarchy in LSD condition

Ultimately, we introduced an index for the hierarchy of information processing in the brain by calculating the standard deviation of the PILI values over brain nodes, where higher variability over nodes means stronger hier-

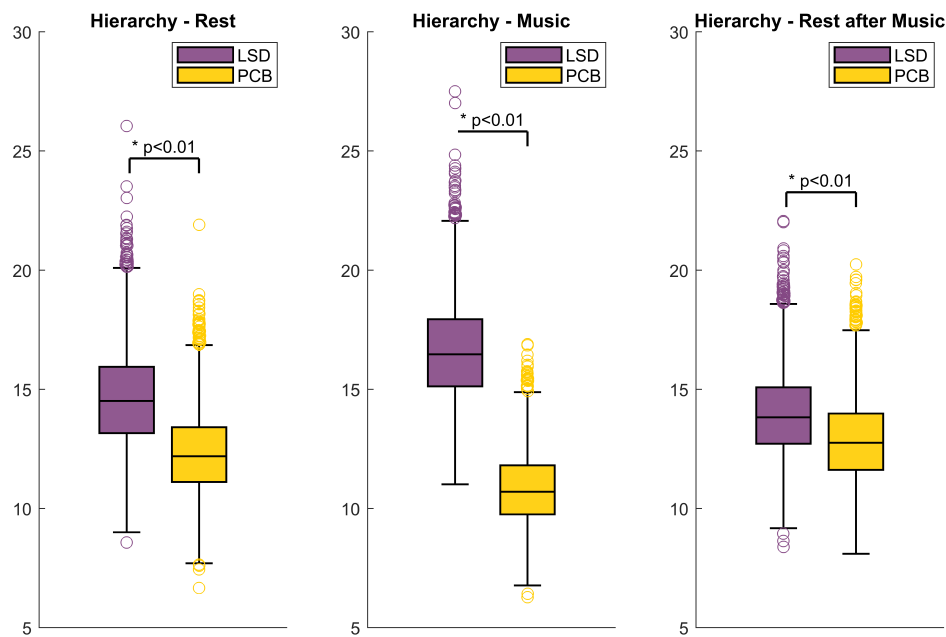


Figure 4.6: **Hierarchy**. Here the distribution over trials of the hierarchy indices is shown for the 3 different conditions for LSD and PCB. Statistical differences between LSD and PCB brain states were evaluated with a two-sided t-test resulting in highly significant differences in all 3 conditions with significantly higher hierarchical organization in the LSD state with respect to PCB. Especially in the Music condition under the influence of LSD a considerably stronger hierarchical organization can be observed.

archy. In Figure 4.6 we show the distribution over the 3000 trials of the hierarchy indices for all 3 conditions and both drug states for the synchronization protocol. We can see that the differences between LSD and PCB were highly significant ($p < 0.01$) in all 3 conditions, with higher hierarchical organization under the influence of LSD than for PCB. This effect was strongest in the Music condition and again less apparent in the Rest after Music condition, which, as already mentioned above, most likely depends on the vanishing effect of the drug during the experiments.

4.4 Discussion

We applied a novel *in silico* model-based perturbational approach to analyze the perturbation-elicited changes in global and local brain activity under the influence of LSD compared to Placebo (PCB) in three consecutive behavioral conditions, namely a resting-state followed by resting while listening to music and finally another resting-state. Besides finding global functional connectivity changes and a shift of the brain's global working point to higher connectivity for the LSD state, we showed that under the influence of LSD the system takes longer to regain baseline activity after a strong model perturbation compared to the PCB state. We found that this was globally the case but underlined that certain brain regions and networks, such as the limbic network, the visual network and the default mode network highlighted these differences on a local level. Finally, we analyzed the differences between LSD and PCB with regards to hierarchical brain organization and found a stronger hierarchy of information processing under the influence of LSD.

In the data-driven part of our analyses, we found that the functional connectivity was higher on average in the LSD state than in the PCB state, which was especially emphasized in the Music condition (Fig. 4.2A), where the effects of LSD seem to be amplified as already shown in previous publications (Kaelen et al., 2015, 2016; Preller et al., 2017a). This finding confirms the results of previous studies, where it was shown that high-level association cortices and the thalamus showed increased functional connectivity under the influence of LSD (Tagliazucchi et al., 2016c), thalamic functional connectivity to various cortical regions was significantly increased (Müller et al., 2017) and that the functional connectivity of the primary visual cortex to other cortical areas was significantly higher under the drug (Carhart-Harris et al., 2016b). Similar results have been found with other psychedelic drugs such as psilocybin (the main hallucinogenic component of “magic mushrooms”) (Carhart-Harris et al., 2012, 2013; Roseman et al., 2014; Tagliazucchi et al., 2014) and ayahuasca, a psychedelic beverage traditionally used by Amazonian Amerindians (Palhano-Fontes et al., 2015).

In order to study the whole-brain dynamics underlying the psychedelic state, first, we applied a whole-brain model based on the normal form of a supercritical Hopf bifurcation simulating directly the fMRI BOLD response. We demonstrated that the optimal global working region of the

system shifted to higher global coupling parameters in the LSD state when compared to PCB. Yet again, statistical significance was only reached in the Music condition (Fig. 4.2B). This means that in the LSD state the brain shows higher connectedness on a global level, agreeing with the previously discussed increase in functional connectivity, suggesting enhanced propagation of activity and better communication between distinct brain regions. This finding is in agreement with previous studies, where it was shown that the dynamical repertoire of the brain increases in the psychedelic state (Tagliazucchi et al., 2014), implying that the brain operates in a different dynamic working region under the influence of hallucinogenic drugs. This result has again been demonstrated by Atasoy et al. (2017b), where it was shown that LSD tunes brain dynamics closer towards criticality, entailing an increase in the diversity of the repertoire of brain states.

With the optimal working point representative of each condition, we studied the responses to strong offline model perturbations in each state. This novel methodology has recently been described by Deco et al. (2018), where it was successfully applied to two distinct datasets containing human fMRI BOLD data from two vigilance conditions: awake and slow-wave sleep. There we could dissociate the two distinct brain states based only on the perturbation-elicited responses (see Chapter 3). The importance of this new methodology lies in the fact that perturbations are exclusively applied *in silico* to a whole-brain computational model, allowing for stronger, longer lasting and brain node-specific perturbations in ways not possible experimentally. Another important difference to previously described perturbation procedures (Massimini et al., 2005; Ferrarelli et al., 2010; Casali et al., 2013) is the fact that with this new approach we measure the recovery characteristics of the system after the offset of the perturbation, not the dynamical reaction to the perturbation itself.

The return to the basal brain activity is characterized by the Perturbative Integration Latency Index (PILI), which takes into account the time it takes for the system to return to the baseline as well as how strong it deviates from the basal activity after the perturbation. The PILI is calculated from the global level of integration across all different brain areas based on the instantaneous signal phases. Interestingly, we found differences in the global integration even without applying any perturbation, where the basal integration was shown to be increased under LSD in contrast to PCB, where this effect was again amplified in the Music condition (Fig. 4.3). This means that the communication and interaction between

distinct brain areas are enhanced under the influence of LSD, agreeing with the previous study of Tagliazucchi et al. (2016c), where, amongst other things, they show that LSD enhances the between-module integration of highly coupled nodes. The interesting observation that in the Music condition under LSD the basal integration increases while during PCB it slightly decreases could be due to the fact, that as already described before, music is known to enhance the psychedelic experience and therefore brings out the LSD specific brain changes even more, whilst under PCB listening to music represents a distraction from the resting-state, a kind of task, which as a consequence diminishes the brain-wide integration and the general repertoire of activity (He, 2013; Ponce-Alvarez et al., 2015b). The fact that the differences between the LSD and PCB states decreased in the Rest after Music condition, is, as already mentioned above, most likely due to the vanishing effect of the drug in the course of the experiment.

When looking at the differences in the PILI values between the LSD and PCB states, it is evident that the responses after a model perturbation to each specific brain node at a time were very different for the two drugs in all 3 conditions (Rest, Music, Rest after Music), with highest differences observed in the Music condition (Fig. 4.4). PILI values were significantly higher in almost each node (exact information with corresponding p-values in Tables C.1 and C.2 in Appendix C) under the influence of LSD, meaning that the underlying dynamical complexity is significantly enhanced in this brain state. A higher PILI value indicates that the perturbed node shows increased sensitivity to a model perturbation, it reacts stronger to it and it takes more time for it to turn back to normal baseline activity. This indicates that the brain is working further away from a stable equilibrium point under the influence of LSD than under normal conditions. Interestingly, the response to a synchronous offline perturbation was much higher in LSD than to a perturbation into the noisy regime (Fig. 4.3). Also the noise perturbations yield slightly increased responses under the influence of LSD, but the differences are almost negligible (Fig. 4.3). A possible explanation for this observation could be the fact that the amplitude of the perturbation is higher when the bifurcation parameter a increases, which is the case in the synchronization protocol in comparison to the noise protocol and thus leading to longer relaxation times after a perturbation in the synchronous regime. For this reason we focused our analyses on the synchronous model perturbations. Another interesting observation is the fact that the PILI decreased on a global level during the Music condition in the PCB state

(Figures 4.3 and 4.4). Yet again, this result could be due to the fact that listening to music compared to the "normal" resting-state represents a kind of task, a distraction from being at rest, generating a reduced response to an external model perturbation and thus a reduction of the dynamical repertoire of brain states (He, 2013; Ponce-Alvarez et al., 2015b).

Analyzing the perturbation-elicited differences on a local node level (Fig. 4.4 and Table 4.1), we found that some brain regions were more dominant regarding differences in PILI in all 3 conditions than others. The cingulate cortex areas reached very low p-values in all 3 conditions. The cingulate cortex is an integral part of the limbic system, which is mainly responsible for emotional formation and processing (Hadland et al., 2003), which plays an important role in the psychedelic experience. Another dominant node with large PILI differences was the precuneus, where the activity is known to correlate with processes involved in self-consciousness and self-reflection (Johnson, 2002). Next, the gyrus rectus showed low p-values in all 3 conditions, which is part of the inferior frontal lobe. Its function is not yet completely clear, but it may be involved in higher cognitive function (Orrison, 2008). Finally, the supplementary motor area displayed high differences between the two brain states, which is known to be involved in self-referential cognition and self-relevant processing (Northoff et al., 2006; Schneider et al., 2008; Preller et al., 2017a).

With the local node information, we then investigated the differences in PILI values on a resting-state network level, where the results were quite consistent across behavioral conditions (Fig. 4.5). In all 3 conditions the limbic network yielded the highest perturbation-elicited differences between the LSD and the PCB state. One of the main responsibilities of the limbic network is, amongst other things, the processing of emotions like fear, rage and placidity (Morgane et al., 2005; RajMohan and Mohandas, 2007). This result confirms the well known effect of LSD to produce emotional arousal and lability (Carhart-Harris et al., 2016a). Yet again, the highest difference was reached in the Music condition, agreeing with previous experimental results, that LSD enhances the emotional response to music (Kaelen et al., 2015). Interestingly, the limbic network has also been previously associated with depression. Both structural and functional abnormalities, such as decreased activity, have been found in limbic areas in major depressive disorder (MDD) patients (Bennett, 2011; Pandya et al., 2012). This connection supports the already studied

positive effects of LSD and other psychedelic drugs as a possible therapy base in MDD patients (Carhart-Harris and Goodwin, 2017; Carhart-Harris et al., 2017). Another resting-state network presenting high differences compared to the PCB state was the visual network. This result is not surprising, since the effects and hallucinations are mainly visual during the LSD experience and furthermore visual areas have previously been shown to change significantly under the influence of the drug (Carhart-Harris et al., 2016b). Next, the DMN displayed high PILI differences in the LSD state. The DMN has recently been associated to the LSD experience, where it was shown that functional connectivity from the DMN to other networks increased and within network connectivity decreased under the influence of the drug, which are both traits of psychedelic drug effects on brain networks. Furthermore DMN activity correlates with various typical characteristics of the psychedelic experience, such as self-reflection processes, out-of-body experiences and internal awareness which could set the ground for the experience of ego dissolution associated with LSD (Tagliazucchi et al., 2016c). Importantly, all resting-state networks become more sensitive to external model perturbations in the LSD state compared to PCB, which, yet again, indicates a general shift in global brain dynamics.

Finally, we introduced a measure for determining the hierarchical organization of the brain by simply looking at the variance over nodes of the perturbation-elicited responses. Larger variance over brain nodes means higher heterogeneity and thus can be interpreted as a stronger hierarchical organization, with leading and following nodes. We found that in the LSD state the hierarchical organization of the brain was significantly higher in all 3 conditions than in PCB (Fig. 4.6). Thus, under the influence of LSD each brain node becomes more individual after a strong model perturbation, certain areas react more sensitive to an offline perturbation than others. This result also agrees with the before discussed finding that some particular nodes or networks show higher recovery times after perturbation than others. It also concurs with a recent study where it was shown that the brain is operating closer to criticality in the psychedelic state which implies a higher hierarchical organization of cortical networks (Moretti and Muñoz, 2013; Atasoy et al., 2017b). Furthermore, disrupted hierarchical organization has previously been associated with different neuropathological disorders such as schizophrenia or depression, with changes in the multimodal network organization (Bassett et al., 2008), a shift toward randomization in the brain networks (Zhang et al., 2011) and attenuated top-down cognitive

control (Disner et al., 2011), once again setting the base for possible clinical applications of psychedelic drugs.

4.5 Conclusion

In this chapter we have presented a novel offline perturbational method applied on Lysergic acid diethylamide (LSD) data. We have shown that the brain's global working point shifts to more complex dynamics after LSD intake when compared to Placebo intake, suggesting fundamental changes in brain dynamics and complexity under the influence of psychedelic drugs. By exploring the underlying mechanistic properties of the whole-brain dynamics in the LSD state by perturbing the whole-brain computational model one node at a time, we have found a consistently higher recovery time under LSD influence implying enhanced dynamical complexity in this brain state. We have shown that this was globally the case, but have added that certain brain regions and resting-state networks highlighted these differences on a local level, being that especially the limbic network, the visual network and the default mode network. Furthermore we have found a higher hierarchical brain organization under LSD influence as compared to Placebo, suggesting an enhanced repertoire of brain dynamical states and closeness to criticality in this brain state.

The here applied perturbational approach based on whole-brain modeling gave us the possibility to explore characteristic changes in whole-brain dynamics of the psychedelic state in ways not possible experimentally. Additionally, the results presented in this study add further evidence to possible future clinical applications of psychedelic drugs in specific psychiatric and neurological disorders.

General Discussion

The overall goal of this thesis was to elucidate the underlying mechanisms and dynamical processes governing different brain states. In the first chapter, we provided an introduction to the features and characteristics of distinct brain states, which included the resting-state, sleep and anesthesia and the psychedelic state of the brain. We have seen how the field of resting-state brain research has evolved over the past two decades and have described the main tools to investigate the features of resting-state brain activity, such as functional connectivity, and also the main discovery in this field: resting-state networks (Raichle et al., 2001; Fox et al., 2005; Damoiseaux et al., 2006; Mantini et al., 2007; Van Den Heuvel et al., 2009; Brookes et al., 2011).

We have then reviewed the experimental evidences of global and local changes in brain activity and connectivity during human NREM-sleep and anesthesia. It was shown that on the one hand FC decreases on a global level during a state of reduced vigilance and that it becomes more similar to the underlying structural connectivity, and that on the other hand RSNs are generally preserved during deeper stages of sleep or anesthesia, while the within- and between-network connectivity strength is altered (Boly et al., 2008; Horovitz et al., 2009; Larson-Prior et al., 2009; Sämann et al., 2011; Boly et al., 2012; Tagliazucchi et al., 2013). We have furthermore seen that the effective connectivity in terms of causal interactions between different brain regions is lowered (Massimini et al., 2005, 2009; Ferrarelli et al., 2010; Tononi, 2012; Casali et al., 2013).

Another brain state we were interested in was the brain under psychedelic substances, such as LSD or psilocybin, where we pointed out that within the last few years an increasing number of neuroimaging studies (Carhart-Harris et al., 2012; Muthukumaraswamy et al., 2013; Tagliazucchi et al., 2014; Palhano-Fontes et al., 2015; Carhart-Harris et al., 2016b; Tagliazucchi et al., 2016c; Preller et al., 2017a,b) have reported different types of brain alterations under these types of drugs, such as increased visual cortex blood flow and functional connectivity, a reduction of the integrity of functional brain networks, a global increase in connectivity between networks and an enhanced repertoire of dynamical brain states.

All these distinct types of altered brain states, as different they may be, have some traits in common. All of the cited studies, which were mainly performed with whole-brain neuroimaging, found changes in neuronal activity in distinct areas of the brain or on a global level, alterations in functional connectivity, differences in RSN within- or between-network connectivity or integrity, changes in effective causal connectivity or in the repertory of dynamical brain states. Even though these brain states have little in common at first sight, when looking deeper into whole-brain functioning, they seem to be similar regarding the features and characteristics which change under these altered conditions, even if *how* they change is different. This reasoning calls for a common method when trying to find a mechanistic explanation for the experimentally observed changes which are characteristic for each different state.

As explained in Chapter 1, the obvious approach for elucidating the underlying dynamics governing these distinct brain states, is to build a computational model which simulates the activity we are interested in, based on more or less biologically realistic assumptions. The main advantage of this approach is that we have total control over the parameters and underlying dynamical properties of the model, which makes it possible to deduce possible explanations of “real” brain dynamics, once we have found a good fit with the model. The model which we applied in all three studies elaborated in this thesis was the Hopf whole-brain model, a quite novel approach applied in combination with whole-brain neuroimaging data, which can simulate both oscillatory and noisy behavior and with which the fMRI BOLD signals can be simulated directly (Deco et al., 2017b; Jobst et al., 2017; Saenger et al., 2017; Deco et al., 2018).

The characteristic of the Hopf model to be able to shift between oscillatory and noisy behavior is the basis of the *in silico* model perturbation approach introduced in Chapter 1, where we also put this novel approach into a perspective of pre-existing literature on the topic of brain perturbation and stimulation methods. We explained that the novel model-based perturbational approach introduced by Deco et al. (2018) complements the existing perturbational studies performed by Massimini and colleagues (Massimini et al., 2005; Ferrarelli et al., 2010; Casali et al., 2013).

In the second chapter of this thesis we analyzed fMRI BOLD signals recorded in healthy subjects during wakefulness and slow-wave sleep, which represents the deepest of the 3 NREM sleep stages (Iber et al., 2007). We compared the two states by looking into differences between the mean FC matrices, where we found significantly higher functional connectivity on a global level during wakefulness. Furthermore we looked into a dynamical measure, the metastability, which was lowered during sleep, indicating a reduced repertoire of brain dynamical states in this condition. These results coincide with various results from the literature, where it was shown, that functional connectivity is lowered during sleep (Kaufmann et al., 2005; Horovitz et al., 2009; Sämann et al., 2011; Spoormaker et al., 2012; Tagliazucchi et al., 2012a). Tagliazucchi et al. (2016a) showed additionally that the repertoire of transient network states was decreased during propofol-induced anesthesia, supporting our finding of diminished metastability in a state of reduced vigilance. In another very recent article by Atasoy et al. (2017a) sleep was linked to a reduction of the repertoire of connectome harmonics – a framework of extracting harmonic brain modes, i.e. fundamental building blocks of spatio-temporal neural activity patterns, from the structural connectivity data – yet again affirming our finding of lowered metastability during sleep.

We then applied the Hopf whole-brain model to the data after fitting it to the mean FC in each of the two vigilance states. What we found, was that on a global level, the dynamic working region where the model fitted the data best, was shifted significantly away from the bifurcation point to a noisy oscillatory state. This is a very important finding, which is able to explain the experimentally observed changes in sleep compared to wakefulness from a mechanistic point of view. The proximity of the underlying dynamics of the whole system to the bifurcation, i.e. the critical regime, allows for a better exploration of different dynamical states in the brain and helps to process incoming stimuli in a faster and more

efficient way (Deco et al., 2011; Deco and Jirsa, 2012; Deco et al., 2013a, 2017b). During sleep, on the other hand, incoming stimuli need to be stronger in order to be “recognized” by the system, which is exactly what we experience during sleep.

We wanted to go even deeper to find the actual level of interaction and connectivity between different brain nodes by calculating the effective connectivity between all brain regions. Effective connectivity was here based on the anatomical connections, of which the connection weights were optimized based on the similarity between the simulated and the empirical FC. This model optimization stabilized after a certain amount of iterations and can such be interpreted as the “real” effective interaction between distinct brain areas. We found a global decrease in effective connectivity in the sleep state, meaning that the communication between different brain regions is limited. Even though this approach is completely different from the well-known method introduced by Massimini and colleagues (Massimini et al., 2005; Ferrarelli et al., 2010; Casali et al., 2013), where effective connectivity is understood as causal interactions between different brain regions, our approach still reflects a similar result, namely that the distinct brain nodes communicate less with each other and that the propagation of interactions is decreased during sleep, which in the original approach manifests itself with a local perturbation dying out on the perturbation site and not being propagated to other brain areas.

The approach explained in this chapter brings us one step closer to understanding the dynamical basis of the neural and functional processes underlying a reduced vigilance or “unconscious” state. This quite simple, yet powerful model is able to capture important features of the mechanisms governing different brain states and also effective connections in the brain can be extracted in a quite simple way. With this work we contribute significantly to an enhanced understanding of the fundamental principles governing different states of consciousness, which is still an ongoing field of research.

In the third chapter we continued elaborating on the state of reduced vigilance during deep sleep by repeatedly analyzing fMRI BOLD data recorded during wakefulness and deep sleep taken from two independent datasets. We introduced a novel *in silico* perturbational approach, where one node or a group of nodes of a whole-brain model were perturbed by shifting its dynamics away from its basal state after which the latency the system takes to recover its normal dynamics was calculated. This method

is based on the Hopf whole-brain model, where we take advantage of the bifurcation parameter, which regulates in which dynamical regime – oscillatory or noisy – the model is in. After adjusting the model to each brain state by fitting the global coupling parameter such that the mean degree of synchronization between simulated and empirical BOLD signals was most similar, the bifurcation parameter of single brain nodes was shifted for a certain amount of time away from the bifurcation, either in positive or negative direction. This procedure simulates an external perturbation to a particular brain node. After perturbation offset we measured the latency the system took to recover its baseline activity, which we called Perturbative Integration Latency Index (PILI). Applying this approach we found that for the awake model the recovery was significantly slower on a global level than for the sleep model, indicating higher complexity during wakefulness and less stable dynamics, a phenomenon which has also been called “critical slowing down” in the literature (Wissel, 1984; van Nes and Scheffer, 2007; Meisel et al., 2015). This refers to a system’s tendency to take longer to recover from a perturbation the closer it gets to a transition point (Meisel et al., 2015), which is exactly what we can observe in an awake resting-state.

The presented perturbation method is a completely new concept of studying whole-brain dynamics underlying different brain states, which complements the previously performed experimental perturbation studies by Massimini et al. (2005), Ferrarelli et al. (2010) and Casali et al. (2013). The here presented results are conform with the findings by Massimini and colleagues, since they also indicate reduced communication and lower dynamical complexity during sleep. Additionally this novel approach gives us insights into the dynamical processes occurring *after* a model perturbation, while previously only the direct response was analyzed (Casali et al., 2013). Further advantages are of course the model nature of the method, meaning that on the one hand no costly and expensive experimental and ethical protocols need to be followed, and on the other hand there are no limitations in perturbation duration, number of nodes perturbed at the same time and number of trials. Especially the number of trials is an important point to take into consideration, because as discussed in Chapter 1, it is known that resting-state brain activity can not be taken simply as a trivial baseline state without any structure or dynamics. Therefore it is important to be able to average over a large number of trials when calculating the return to the original dynamics, since the original dynamics, the baseline state itself, changes with each trial.

In the last of the 3 main chapters of this thesis, Chapter 4, we applied this very perturbational approach to a completely different kind of data, namely fMRI BOLD signals recorded in healthy participants under the influence of LSD, a hallucinogenic drug. We first analyzed possible changes in functional connectivity on a global level, where we found elevated FC in the LSD state, especially in the condition where the subjects were listening to music, which is known to amplify the psychedelic experience (Kaelen et al., 2015, 2016; Preller et al., 2017a). When fitting the Hopf whole-brain model to the data, we found that the global working point was shifted compared to the Placebo state, namely to higher connectivity, the exact opposite of what we found for the sleep state. By applying the perturbative method, we demonstrated that under LSD the system took significantly longer to regain baseline activity as compared to Placebo, which was valid almost uniformly for all brain nodes implying an enhanced underlying dynamical complexity in the psychedelic state. While during slow-wave sleep we could observe a reduced complexity with regards to resting wakefulness, under the influence of psychedelic drugs we could detect even higher dynamical complexity than during “normal” rest. As such, the perturbational method in combination with the Hopf whole-brain model can be seen as a unifying concept of uncovering the underlying dynamical mechanisms governing different brain states.

In this study we went deeper and also looked at regional changes, especially regarding different resting-state networks. Thus, we analyzed the latencies after model perturbations to each brain node representative of each of 7 analyzed resting-state networks. Here we found some very intriguing results, which revealed that the most affected resting-state networks by a simulated perturbation, meaning those which showed the highest latencies in the LSD state as compared to the Placebo state, were those networks which were either expected or already known to play an important role for the psychedelic experience, being that the limbic, the visual and the default mode network (Carhart-Harris et al., 2016b; Tagliazucchi et al., 2016c). This result contributes significantly to the quite recently newly discovered field of research of human neuroimaging with LSD or other psychoactive drugs, since it shows the importance of these networks for the first time from a computational neuroscience view.

Subsequently we analyzed differences in the hierarchical brain organization by applying a simple method leaning on a previous publication by Deco and Kringelbach (2017), where we looked at the variability of the PILI values over brain nodes. Higher variance over brain nodes implies higher heterogeneity and can therefore be interpreted as a stronger hierarchical

organization. We found that after LSD intake the variability of PILI values over brain nodes was significantly higher than after Placebo intake, which suggests a stronger hierarchy among brain nodes, where some nodes react more sensitive to an external model perturbation than others. The resting-state of the brain has been linked before to possess a hierarchical modular functional organization (Zhou et al., 2006; Meunier et al., 2010; Doucet et al., 2011). A hierarchical organization of the brain has been previously related to high dynamic complexity (Sporns, 2000; Meunier et al., 2010) and closeness to criticality (Moretti and Muñoz, 2013; Atasoy et al., 2017b), indicating that under LSD the brain possesses these properties in an enhanced way compared to the “normal” resting-state.

The results presented in this study make some significant contributions to the very recent field of neuroimaging applied on the psychedelic brain state. We show important new insights into the underlying dynamics governing the psychedelic experience, along with – to our knowledge – only two other preceding studies on the dynamical mechanisms underlying this state: on the one hand a study by Carhart-Harris et al. (2014), where the authors suggest that changes in brain dynamics which manifest themselves in elevated entropy, are a fundamental mechanism producing the elevated consciousness during the psychedelic experience, and on the other hand a very recent study by Atasoy et al. (2017b), which shows that, by applying their novel methodology of “connectome-harmonic decomposition”, where fMRI data is decomposed into a set of independent, frequency-specific brain states, the repertoire of active brain states is increased after LSD intake, suggesting a general re-organization of brain dynamics in this state. Additionally the here presented results provide further theoretical insights into possible future applications of psychedelic drugs in certain psychiatric and neurological disorders as schizophrenia or depression, since some of the traits and characteristics which we showed affected by LSD in an enhancing way, have been previously associated with these disorders to manifest the opposite effect (Bassett et al., 2008; Bennett, 2011; Disner et al., 2011; Zhang et al., 2011; Pandya et al., 2012).

5.1 Study limitations and general research contributions

As every research study, the here presented work has some limitations, partly due to technical reasons, partly due to simplicity reasons. In the first study presented in Chapter 2 we almost explicitly focused on

|

|

global changes of the dynamical working regime the brain is operating in in different states. We shifted the two free model parameters homogeneously for all brain nodes when searching for the optimal parameter region which fitted the data best. Especially the bifurcation parameter could have been adapted for each node by using the spectral information of the fMRI BOLD signal in each brain region, as previously shown in Deco et al. (2017b). On the other hand we analyzed the effective connectivity between all brain nodes, which does represent a node-wise measure. We did not dig very deep though into node-wise differences, we only looked at the 10 regions with the highest effective connectivity strengths among the whole 90. Our reasoning for not going deeper into the analysis of local dynamical changes was the fact that with the global analysis we had already found a good model description of the data. Usually, when simulating data with computational models, one attempts to chose the simplest possible model to sufficiently explain the features or observations in question. Furthermore, when looking at the effective connectivity for each node, we found that almost all nodes manifested higher effective connections (84 out of 90), indicating that most probably the effects of sleep on brain dynamics are of global nature. Nevertheless, an exhaustive investigation would be needed to confirm this hypothesis.

Another limitation, which is applicable on all three main studies presented in this thesis, is the fact that we only employed one type of model, rather of phenomenological nature, to study the underlying dynamical processes of different brain states. The here presented methods and results are however not exclusive to the Hopf model used herein, other more realistic models based on biophysical mechanisms can be used to study the brain mechanisms governing these distinct states, such as neural field models or also more realistic models of effective connectivity, which could possibly provide a more detailed characterization of the underlying dynamical processes. On the other hand, as discussed above, we always seek to explain the mechanisms producing the experimental results we are questioning in the most simple way possible, while maintaining a realistic and complex enough set-up, to be still able to reproduce certain features of the experimental data (such as for example group-averaged functional connectivity). The here applied Hopf whole-brain model represents a very simple way of introducing different dynamical regimes by only adapting one model parameter. Additionally it has been previously shown to be able to give a good representation of the resting-state as measured

with fMRI (Deco et al., 2017b), and moreover it has the advantage of simulating directly the fMRI BOLD signal, without having to apply an extra hemodynamic model based on the main model. Notwithstanding, it would still be desirable to test the here presented results with other types of models and compare the outcomes, in order to obtain yet another confirmation of the results shown in this thesis.

Coming back to more localized analysis methods, in the second study presented in Chapter 3 it would have also been interesting to look at the perturbative latency indices based on a node-wise adapted bifurcation parameter as starting value for the perturbation instead of setting all bifurcation parameters to 0 before and after each perturbation. We performed this analysis in Deco et al. (2018), but there we did not analyze very profoundly the differences in latencies between distinct nodes. Instead we focused our investigation on the correlations between PILI values and other node-wise metrics, since the general focus of this work, was – as the previous study in Chapter 2 – a more global one. This is still a possible future analysis step though, which can be performed quite easily.

In the last study presented in this thesis in Chapter 4, the just explained limitation is valid as well. Even though here we based our analysis on node-wise perturbations, the bifurcation parameter was not adapted specifically to each node, but set to 0 before and after perturbations. Also in this study, this expansion of the method could be implemented quite easily.

Despite of these limitations inherent to the studies presented in this thesis, we made some important contributions to the investigation of the dynamical mechanisms underlying different brain states with our work. First of all, we employed a whole-brain model of phenomenological nature to fMRI BOLD data recorded in different brain states and were able to provide a good description of the underlying dynamical processes, mainly on a global level, in these states, even though the model is not directly based on biophysical brain mechanisms. Based on this model we found a possible mechanism explaining the experimentally observed differences between wakefulness and sleep. To expand the model analysis, we introduced a novel perturbative approach, which was able to successfully classify different brain states of completely distinct nature, namely wakefulness and sleep and the psychedelic

state from normal rest. We furthermore added a major contribution to the newly rediscovered field of research on psychedelic drugs, where up to now basically no studies were available which provide information on the dynamical mechanisms underlying the psychedelic state, with only very few exceptions (Carhart-Harris et al., 2014; Atasoy et al., 2017b).

5.2 Conclusion

The collection of studies presented in this thesis provides novel insights into the brain mechanisms and dynamical processes underlying different brain states by using whole-brain computational modeling. It was demonstrated that a global shift of the dynamical working region to a noisy oscillatory state could represent a possible mechanistic explanation of the empirical functional changes observed during deep sleep when compared to resting wakefulness. Additionally it was shown that the effective connections between different brain areas decreased globally during sleep suggesting a lower level of integration and excitability during sleep on a whole-brain level (Jobst et al., 2017). Next, we introduced a novel perturbative approach to study brain dynamics by characterizing the latency of the system's recovery after an *in silico* model perturbation, indicating the dynamical stability of different brain states. We found that globally the system took more time to regain baseline activity after a model perturbation during resting wakefulness as compared to deep sleep, suggesting that the global shift of the dynamical working point causes the brain to be less affected by external perturbations during sleep (Deco et al., 2018). Lastly we applied the herein presented perturbational approach to data recorded under the influence of LSD and showed that the recovery time after a model perturbation was consistently higher under LSD, suggesting enhanced dynamical complexity in this brain state. We furthermore demonstrated that this result was especially pronounced in resting-state networks which are assumed to play an important role in the psychedelic experience. Finally we showed that under LSD the brain presented a higher hierarchical organization, indicating an augmented repertory of brain dynamical states and closeness to criticality.

The here presented methods and results contribute significantly to the ongoing investigation of the dynamical mechanisms underlying different brain states and pave the way for the possible application of computational models in future clinical contexts.

Appendix Chapter 2

This chapter contains published work which can be found in: 'Electronic Supplementary Material' of *Increased stability and breakdown of brain effective connectivity during slow-wave sleep: mechanistic insights from whole-brain computational modelling* published in *Scientific Reports* in 2017. Link: https://static-content.springer.com/esm/art%3A10.1038%2Fs41598-017-04522-x/MediaObjects/41598_2017_4522_MOESM1_ESM.pdf.

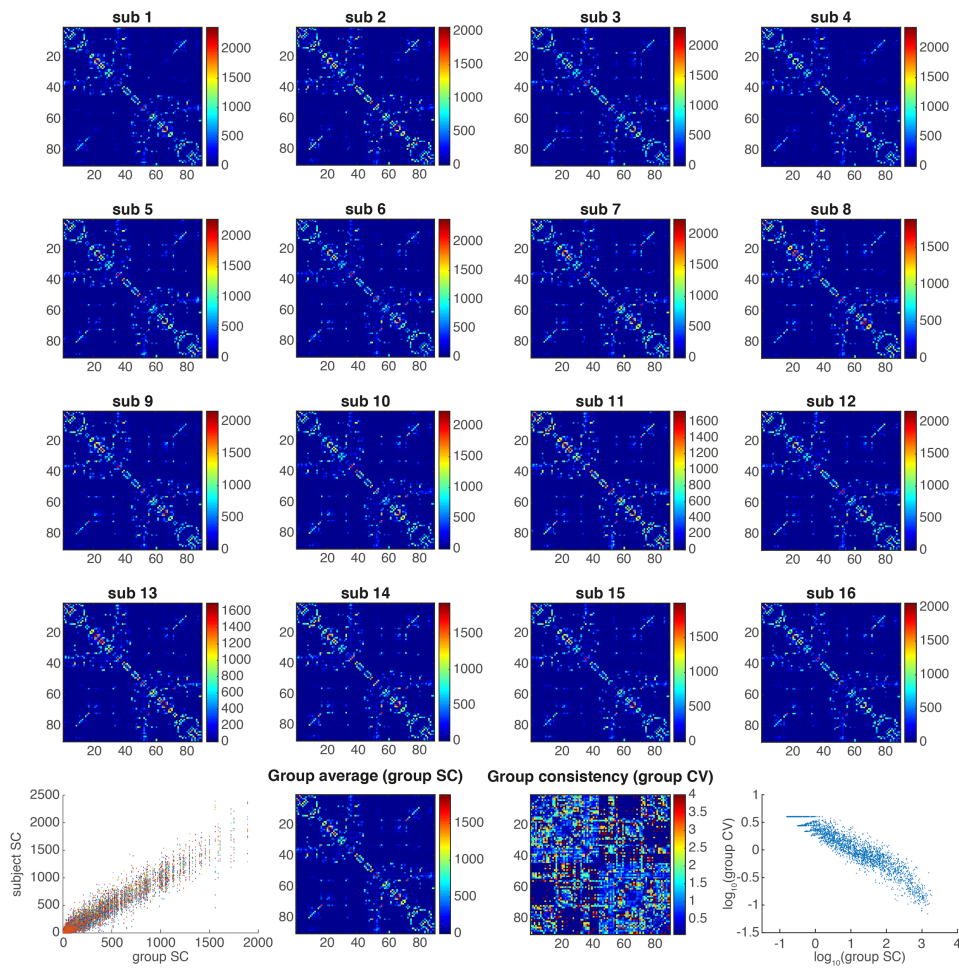


Figure A.1: **Subject-specific SC analysis.** In the first four rows the subject-specific SC matrices are shown. In the bottom row we show (from left to right) the subject-specific SC weights as a function of the group-averaged SC matrix, which clearly shows the consistency of the group, the group-averaged SC matrix, the group consistency matrix (std/mean; as per Roberts et al. (2017)) and the group consistency as a function of group SC weights, which correspond to Fig. 1 in Roberts et al. (2017). These representations demonstrate that the use of a group level SC matrix is justified.

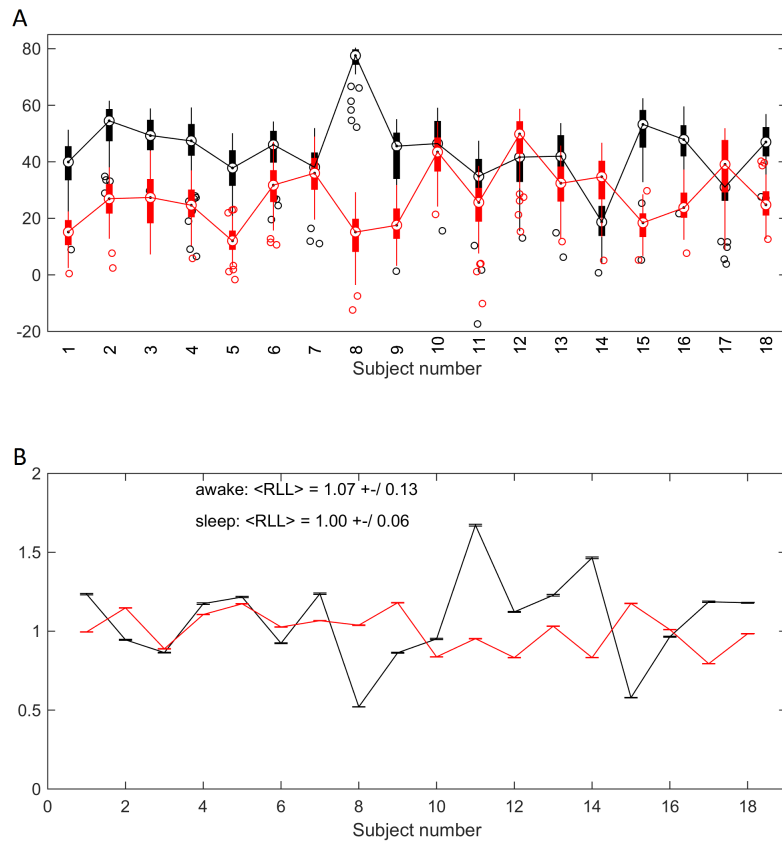


Figure A.2: **Subject level data analysis.** In A a boxplot of the node strength of individual subject-specific FC matrices is shown for awake (black) and sleep (red). It can be observed that almost all subjects (83%) exhibited higher node strength in awake than in sleep. In B the average log-likelihood ratio $r_i = L(X^{(i)}|\Sigma_{\text{train}})/L(X_{\text{pseudo}}|\Sigma_{\text{train}})$ over 5000 random samples is shown for each subject used as testset (see Section 2.2.5), where wakefulness is represented by the black line and sleep by the red line. $\langle r_i \rangle$ is expected to be approximately 1 if the time series of the i -th subject are indistinguishable from a random sample taken from the time series of the remaining subjects.

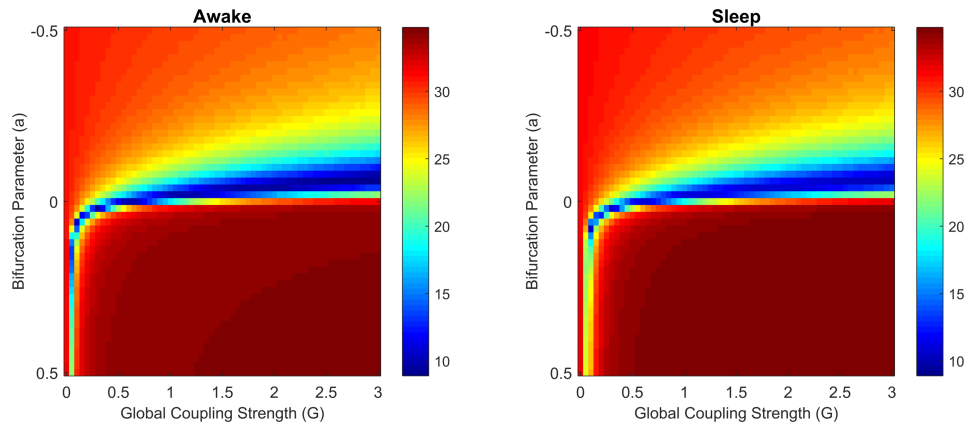


Figure A.3: **Global FC fitting with same node strength.** In this figure we show the Euclidean distance between FC_{model} and FC_{emp} for different values of the global coupling strength G and the bifurcation parameter a in awake and sleep as in Figure 2.3A i.+ii. with the difference that here the empirical FC matrix in sleep has been adapted such that the mean node strength was equal to the empirical FC matrix in awake. This was achieved by adding weight uniformly to all connections of the sleep FC matrix, leaving the maximum possible value at 1, until it reached the same mean node strength as the awake matrix. We can observe that there were no significant differences between the two states.

Appendix Chapter 3

This chapter contains published work which can be found in: ‘Supplementary Information’ of *Perturbation of whole-brain dynamics in silico reveals mechanistic differences between brain states* published in *NeuroImage* in 2018. Link: <https://www.sciencedirect.com/science/article/pii/S1053811917310236>.

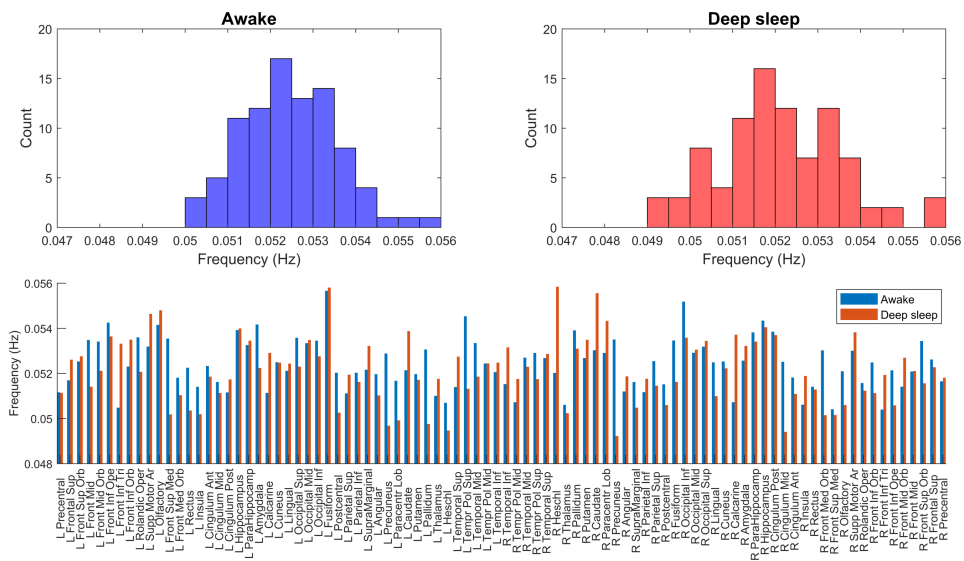


Figure B.1: **Distribution of peak frequencies in the band-passed BOLD signals in all brain areas during wakefulness and deep sleep.** In each AAL brain area, we detected the peak frequency of the band-pass filtered (0.04-0.07Hz) BOLD signals and averaged across subjects in each condition. Top: Distribution of peak frequencies during wakefulness (left) and deep sleep (right). Bottom: Peak BOLD frequency averaged across subjects for each AAL brain area, in each condition. Results from the Frankfurt dataset.

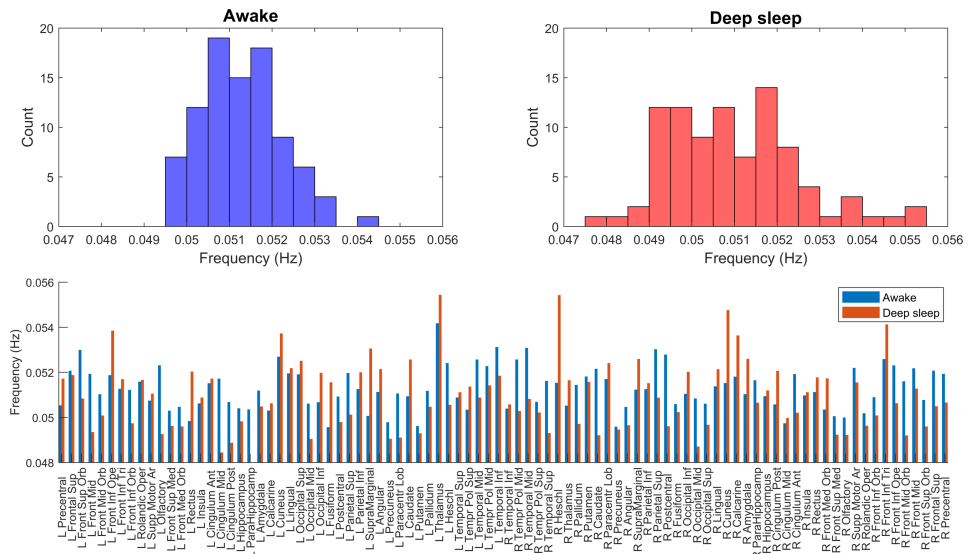


Figure B.2: Distribution of peak frequencies in the band-passed BOLD signals in all brain areas during wakefulness and deep sleep. Same as above but with the Liège dataset.



Appendix Chapter 4

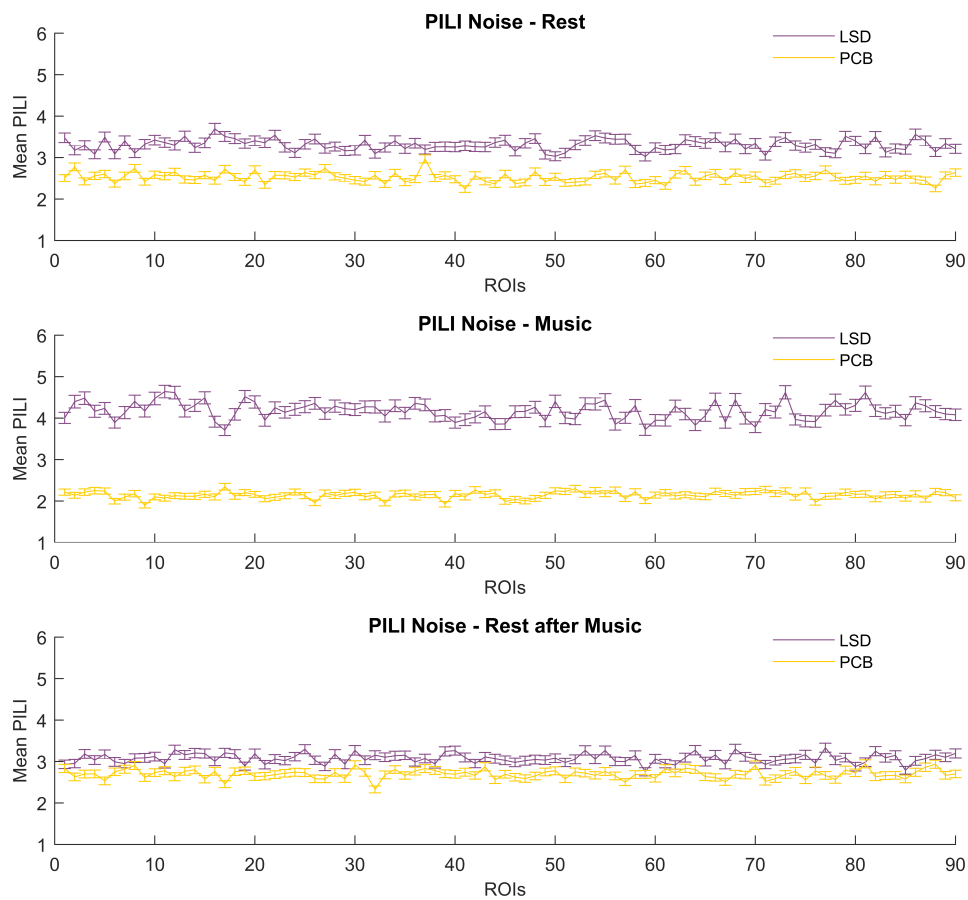


Figure C.1: **PILI – Node level analysis for noise protocol.** Here the mean and the standard error of the mean of the PILI values over trials for the noise protocol are shown for each of the 3 conditions for the LSD and the PCB state for all 90 brain regions. Also in the noise protocol, the global differences between the LSD and PCB induced brain states were amplified in the Music condition. Node-by-node analysis with corresponding p-values can be found in Table C.2.

Table C.1: Node level PILI differences – synchronization protocol.

Rest		Music		Rest after Music	
Brain region	p-value	Brain region	p-value	Brain region	p-value
Cuneus R	5,682e-26*	Putamen R	8,759e-127*	Frontal Inf Oper R	3,282e-08*
Occipital Sup L	1,575e-25*	Caudate R	2,258e-125*	Temporal Sup L	3,939e-08*
Rectus R	2,618e-25*	Calcarine R	1,803e-124*	Amygdala L	4,118e-08*
Frontal Sup R	7,958e-25*	Supp Motor Area L	3,142e-120*	Frontal Sup L	4,439e-08*
Pallidum L	1,567e-24*	Occipital Sup L	1,113e-119*	Amygdala R	5,172e-08*
Frontal Sup Orb R	7,943e-24*	Paracentral Lobule L	1,121e-118*	Frontal Mid R	8,056e-08*
Frontal Mid Orb R	8,771e-24*	Temporal Pole Sup L	1,904e-118*	Occipital Inf L	8,302e-08*
Frontal Med Orb L	1,422e-23*	Hippocampus R	4,807e-118*	Frontal Sup Medial L	8,313e-08*
Caudate L	3,397e-23*	Frontal Med Orb L	1,513e-117*	Cingulum Post L	1,806e-07*
Cingulum Mid R	3,965e-23*	Amygdala R	4,546e-116*	Frontal Med Orb R	1,842e-07*
Insula L	4,348e-22*	Putamen L	3,462e-110*	Parietal Sup R	2,048e-07*
Parietal Sup R	7,266e-22*	Frontal Mid Orb L	1,259e-109*	ParaHippocampal L	2,226e-07*
Parietal Sup L	5,427e-21*	Frontal Inf Orb L	3,358e-108*	Occipital Sup R	2,965e-07*
Amygdala L	9,792e-21*	Lingual R	2,201e-107*	Occipital Sup L	3,358e-07*
Hippocampus L	1,018e-20*	Insula R	5,816e-105*	Caudate L	3,645e-07*
Occipital Inf L	1,561e-20*	Temporal Pole Sup R	9,940e-105*	Supp Motor Area L	4,385e-07*
Occipital Mid L	1,805e-20*	Fusiform L	1,117e-104*	Olfactory R	1,081e-06*
Paracentral Lobule L	2,707e-20*	Occipital Mid L	1,816e-103*	Pallidum L	1,438e-06*
Frontal Sup L	3,553e-20*	Olfactory L	1,004e-96*	Calcarine L	1,488e-06*
Frontal Mid Orb L	4,835e-20*	Frontal Inf Tri	5,333e-95*	Olfactory L	1,670e-06*
Frontal Inf Orb L	6,598e-20*	Occipital Mid R	5,398e-92*	Paracentral Lobule R	3,013e-06*
Frontal Inf Orb R	2,662e-19*	Insula L	1,958e-91*	Temporal Pole Sup R	3,321e-06*
Fusiform R	2,688e-19*	Thalamus L	7,819e-91*	Frontal Med Orb L	6,157e-06*
Frontal Sup Orb L	2,809e-19*	Temporal Sup R	1,282e-90*	Frontal Sup Orb L	6,741e-06*
Frontal Sup Medial R	8,699e-19*	Frontal Inf Oper R	7,427e-88*	Parietal Sup L	8,315e-06*
Cuneus L	1,623e-18*	Cuneus L	5,525e-87*	Cingulum Post R	1,269e-05*
Lingual R	3,428e-18*	Fusiform R	4,084e-86*	Temporal Mid L	2,866e-05*
Frontal Med Orb R	7,240e-18*	Frontal Mid R	7,931e-86*	Temporal Sup R	3,463e-05*
Temporal Inf R	1,713e-17*	ParaHippocampal R	9,089e-86*	Occipital Mid R	4,490e-05*
Insula R	2,565e-17*	Occipital Sup R	3,390e-84*	Caudate R	5,663e-05*
Supp Motor Area L	2,821e-16*	Calcarine L	6,622e-84*	Thalamus L	7,069e-05*
Pallidum R	2,851e-16*	Temporal Mid R	5,225e-83*	Putamen R	7,504e-05*
ParaHippocampal L	1,190e-15*	Temporal Pole Mid L	5,463e-83*	SupraMarginal R	9,255e-05*
Temporal Mid R	1,522e-15*	Hippocampus L	6,030e-83*	Fusiform L	1,098e-04*
Temporal Mid L	1,549e-15*	Occipital Inf L	1,083e-82*	Precentral L	1,145e-04*
Occipital Inf R	1,922e-15*	Cuneus R	1,689e-82*	Insula R	1,271e-04*
Occipital Mid R	8,098e-15*	Frontal Inf Tri R	2,955e-82*	Postcentral L	1,459e-04*
Precentral R	8,855e-15*	Thalamus R	3,190e-82*	Lingual L	1,915e-04*
Caudate R	9,012e-15*	Lingual L	4,210e-81*	Paracentral Lobule L	2,464e-04*
Frontal Mid L	9,245e-15*	Parietal Sup L	5,660e-81*	Heschl L	3,117e-04*
Temporal Pole Sup R	3,257e-14*	Temporal Mid L	1,002e-80*	Rectus R	3,465e-04*
Paracentral Lobule R	5,423e-14*	Rolandic Oper R	7,337e-79*	Insula L	4,097e-04*
Frontal Inf Oper L	5,634e-14*	Precentral R	1,095e-77*	Frontal Sup Orb R	4,259e-04*
Frontal Mid R	9,484e-14*	Paracentral Lobule R	3,432e-77*	Temporal Pole Mid L	5,099e-04*
Amygdala R	1,081e-13*	Frontal Mid Orb R	6,078e-77*	Frontal Inf Orb R	6,210e-04
Parietal Inf R	2,141e-13*	Frontal Inf Oper L	2,928e-72*	Postcentral R	9,3136e-04
Rolandic Oper L	2,969e-13*	Temporal Inf L	2,077e-69*	Temporal Inf R	9,509e-04
Precentral L	4,101e-13*	Postcentral L	1,175e-65*	Putamen L	1,300e-03
Fusiform L	4,906e-13*	Rolandic Oper L	2,712e-65*	Frontal Inf Orb L	1,302e-03
Rolandic Oper R	7,263e-13*	Precentral L	6,352e-65*	Frontal Inf Oper L	4,398e-03

table continues on next page

Rest		Music		Rest after Music	
Brain region	p-value	Brain region	p-value	Brain region	p-value
Frontal Inf Oper R	7,833e-13*	Temporal Pole Mid R	1,525e-63*	SupraMarginal L	4,527e-03
Temporal Sup L	1,237e-12*	Frontal Mid L	5,591e-62*	Frontal Mid Orb R	4,888e-03
Postcentral R	2,691e-12*	Temporal Inf R	1,160e-61*	Cuneus L	0,0115
Heschl L	7,004e-12*	Amygdala L	3,583e-61*	Temporal Mid R	0,0215
Temporal Pole Sup L	1,460e-11*	Pallidum R	6,180e-61*	Frontal Mid L	0,0226
Temporal Pole Mid R	3,435e-11*	ParaHippocampal L	1,174e-60*	Rolandic Oper L	0,0515
Frontal Inf Tri L	3,671e-11*	Temporal Sup L	1,638e-60*	Lingual R	0,0934
ParaHippocampal R	1,094e-10*	Parietal Inf L	4,867e-55*	Temporal Pole Mid R	0,0959
Parietal Inf L	1,197e-10*	Frontal Inf Orb R	9,744e-54*	Angular L	0,1096
Heschl R	1,417e-09*	Heschl R	2,998e-53*	Parietal Inf L	0,1774
SupraMarginal L	2,645e-09*	Angular L	6,762e-53*	Rolandic Oper R	0,1922
Temporal Sup R	3,781e-09*	Pallidum L	1,503e-47*	Heschl R	0,2095
Temporal Inf L	7,903e-09*	Occipital Inf R	6,197e-47*	Occipital Inf R	0,2366
Hippocampus R	1,428e-08*	Angular R	2,879e-44*	Frontal Inf Tri R	0,2367
SupraMarginal R	1,443e-07*	SupraMarginal R	2,602e-42*	Cuneus R	0,2503
Frontal Inf Tri R	3,893e-07*	Postcentral R	3,336e-37*	Frontal Inf Tri L	0,3585
Postcentral L	3,482e-06*	Parietal Sup R	2,097e-36*	Parietal Inf R	0,5429
Temporal Pole Mid L	1,434e-05*	SupraMarginal L	7,921e-35*	Pallidum R	0,5851
Angular L	1,575e-04*	Heschl L	1,281e-25*	Thalamus R	0,6176
Angular R	4,713e-04*	Parietal Inf R	8,347e-20*	Angular R	0,6980

In this table brain nodes are ordered for each condition by p-values – from smallest to largest –, based on the PILI differences for the synchronization protocol between LSD and PCB by perturbing each specific node at a time. This table represents a continuation of Table 4.1, where here the regions 21 up to 90 are shown ordered by the size of their p-value. The asterisk indicates statistically significant differences after Bonferroni correction.

Table C.2: Node level PILI differences – noise protocol.

Rest		Music		Rest after Music	
Brain region	p-value	Brain region	p-value	Brain region	p-value
Frontal Sup Orb R	1,141e-07*	Occipital Mid L	1,990e-23*	Rectus R	5,074e-05*
Rolandic Oper R	9,382e-07*	Cuneus R	6,621e-21*	Frontal Mid Orb L	5,564e-05*
Frontal Sup Medial R	1,848e-06*	Frontal Mid R	4,533e-20*	Frontal Sup Medial L	7,032e-05*
Frontal Sup Orb L	3,051e-06*	Olfactory L	1,285e-19*	Rolandic Oper R	1,689e-04*
Temporal Sup L	5,841e-06*	Caudate L	4,971e-19*	SupraMarginal L	4,202e-04*
Olfactory L	7,000e-06*	Supp Motor Area R	1,789e-18*	Insula L	8,278e-04*
Hippocampus L	7,357e-06*	Rolandic Oper L	3,440e-18*	Cingulum Mid L	9,256e-04*
Cingulum Ant L	8,290e-06*	Thalamus L	1,130e-17*	Cingulum Ant R	1,247e-03
Calcarine L	1,262e-05*	Frontal Med Orb R	2,398e-17*	Caudate R	1,430e-03
Amygdala L	1,366e-05*	Temporal Mid R	2,416e-17*	Cuneus R	1,743e-03
Frontal Med Orb L	1,407e-05*	Parietal Inf L	4,327e-17*	Cingulum Post L	2,128e-03
Putamen R	2,635e-05*	Insula L	5,802e-17*	Occipital Mid L	3,455e-03
Occipital Sup R	2,879e-05*	Hippocampus L	1,533e-16*	Precuneus R	4,819e-03
Temporal Pole Mid L	4,325e-05*	Frontal Sup Medial L	2,896e-16*	Occipital Sup R	6,104e-03
Frontal Mid R	4,408e-05*	Precuneus L	9,739e-16*	Lingual L	8,390e-03
Paracentral Lobule R	5,383e-05*	Calcarine L	1,874e-15*	Thalamus L	0,0111
Pallidum R	5,800e-05*	Frontal Sup Orb L	1,924e-15*	Frontal Inf Orb R	0,0126
Rectus L	6,627e-05*	Putamen R	4,060e-15*	Heschl R	0,0186
Rolandic Oper L	7,135e-05*	Frontal Sup R	4,388e-15*	Angular L	0,0193
Thalamus R	7,235e-05*	Frontal Inf Orb L	4,485e-15*	Heschl L	0,0214
Olfactory R	7,921e-05*	Putamen L	7,363e-15*	Frontal Inf Tri R	0,0227
Angular L	1,104e-04*	Rectus R	9,119e-15*	Frontal Sup Orb L	0,0315
Occipital Inf R	1,137e-04*	Cingulum Post R	1,035e-14*	Paracentral Lobule L	0,0337
Cingulum Post R	1,247e-04*	Rectus L	1,202e-14*	Fusiform L	0,0386
Temporal Mid L	1,423e-04*	Frontal Inf Orb R	1,951e-14*	Occipital Sup L	0,0412
Frontal Mid Orb R	1,430e-04*	Frontal Mid Orb R	2,588e-14*	Temporal Pole Mid L	0,0423
Parietal Sup R	2,659e-04*	Angular L	2,855e-14*	Frontal Med Orb L	0,0428
Caudate L	4,006e-04*	Frontal Med Orb L	3,198e-14*	Calcarine R	0,0519
Supp Motor Area L	4,308e-04*	Precentral R	5,219e-14*	Cingulum Mid R	0,0526
Hippocampus R	4,723e-04*	SupraMarginal L	6,477e-14*	ParaHippocampal R	0,0636
Occipital Mid L	8,332e-04	Supp Motor Area L	1,201e-13*	Rolandic Oper L	0,0669
Fusiform L	9,387e-04	Frontal Sup L	2,409e-13*	ParaHippocampal L	0,0725
Angular R	1,579e-03	Cuneus L	3,049e-13*	Frontal Med Orb R	0,0776
Precentral L	1,717e-03	Rolandic Oper R	3,572e-13*	Supp Motor Area L	0,0792
Cingulum Mid R	1,753e-03	Temporal Inf R	3,599e-13*	Frontal Sup R	0,0931
Parietal Inf L	1,970e-03	Occipital Sup L	3,785e-13*	Hippocampus R	0,0948
Occipital Mid R	2,118e-03	ParaHippocampal L	4,792e-13*	Temporal Sup L	0,0959
Temporal Pole Mid R	2,368e-03	Postcentral R	5,278e-13*	Pallidum R	0,0961
Frontal Inf Tri L	2,398e-03	Temporal Pole Mid R	6,556e-13*	Frontal Mid L	0,1017
Insula R	2,512e-03	Temporal Mid L	1,641e-12*	Frontal Inf Oper R	0,1051
Frontal Mid Orb L	2,759e-03	Fusiform L	2,278e-12*	Angular R	0,1130
Temporal Pole Sup R	2,871e-03	Occipital Sup R	2,754e-12*	Amygdala R	0,1200
ParaHippocampal R	2,879e-03	Insula R	2,920e-12*	Olfactory R	0,1363
Calcarine R	3,475e-03	Pallidum R	5,956e-12*	Precentral R	0,1395
Paracentral Lobule L	3,537e-03	Occipital Inf L	6,387e-12*	Temporal Sup R	0,1486
Cuneus R	3,759e-03	Precuneus R	7,048e-12*	Frontal Mid Orb R	0,1623
Temporal Pole Sup L	3,898e-03	Paracentral Lobule L	9,117e-12*	Paracentral Lobule R	0,1725
Frontal Inf Tri R	4,392e-03	Cingulum Post L	9,351e-12*	Amygdala L	0,1805
Temporal Mid R	4,403e-03	Olfactory R	1,481e-11*	Temporal Mid R	0,1867
Pallidum L	4,490e-03	Parietal Sup L	3,028e-11*	Cingulum Post R	0,1931

table continues on next page

Rest		Music		Rest after Music	
Brain region	p-value	Brain region	p-value	Brain region	p-value
Frontal Sup Medial L	4,537e-03	Fusiform R	3,032e-11*	Lingual R	0,2009
Cingulum Ant R	4,735e-03	Postcentral L	3,455e-11*	Occipital Mid R	0,2144
Parietal Inf R	5,090e-03	Frontal Sup Medial R	9,003e-11*	Frontal Sup L	0,2219
Heschl R	6,402e-03	Occipital Mid R	1,357e-10*	Caudate L	0,2519
Insula L	6,468e-03	Temporal Pole Sup R	3,478e-10*	Putamen R	0,2609
Thalamus L	7,711e-03	Temporal Sup R	4,732e-10*	Temporal Pole Sup L	0,2859
Frontal Inf Oper R	7,739e-03	Angular R	6,500e-10*	Temporal Inf R	0,3542
Heschl L	7,753e-03	Frontal Inf Oper R	8,633e-10*	Frontal Sup Medial R	0,3673
Temporal Inf L	8,001e-03	Caudate R	1,084e-09*	Temporal Inf L	0,3710
Fusiform R	0,0142	Cingulum Ant L	1,371e-09*	Parietal Inf R	0,3952
SupraMarginal L	0,0156	Cingulum Mid R	1,447e-09*	Occipital Inf R	0,4173
Precuneus L	0,0218	Pallidum L	1,467e-09*	Frontal Inf Tri L	0,4246
Caudate R	0,0233	Parietal Inf R	1,760e-09*	Temporal Pole Mid R	0,4391
Temporal Inf R	0,0238	Frontal Sup Orb R	1,841e-09*	Olfactory L	0,4414
Precentral R	0,0291	Frontal Inf Oper L	3,730e-09*	Thalamus R	0,4476
Parietal Sup L	0,0311	Frontal Mid Orb L	4,092e-09*	Parietal Inf L	0,4802
SupraMarginal R	0,0320	ParaHippocampal R	7,536e-09*	Temporal Mid L	0,4876
Cingulum Post L	0,0349	Temporal Inf L	7,702e-09*	Rectus L	0,5142
ParaHippocampal L	0,0352	Lingual L	9,415e-09*	Precuneus L	0,5507
Precentral R	0,0395	Frontal Inf Tri L	9,772e-09*	Supp Motor Area R	0,5602
Postcentral L	0,0430	Precentral L	1,240e-08*	Postcentral R	0,5875
Frontal Sup R	0,0449	Calcarine R	1,720e-08*	Occipital Inf L	0,5922
Cuneus L	0,0468	Frontal Mid L	1,953e-08*	Cuneus L	0,6004
Cingulum Mid L	0,0524	Hippocampus R	3,322e-08*	Hippocampus L	0,6549
Supp Motor Area R	0,0557	Heschl L	4,125e-08*	Cingulum Ant L	0,6577
Amygdala R	0,0673	Thalamus R	5,118e-08*	Fusiform R	0,6867
Lingual L	0,0713	Occipital Inf R	8,976e-08*	Parietal Sup L	0,7053
Precuneus R	0,0937	Temporal Sup L	9,158e-08*	Calcarine L	0,7337
Lingual R	0,0959	Frontal Inf Tri R	1,399e-07*	Frontal Mid R	0,7376
Rectus R	0,0986	SupraMarginal R	2,082e-07*	Frontal Inf Orb L	0,7534
Frontal Med Orb R	0,1183	Temporal Pole Sup L	2,298e-07*	Parietal Sup R	0,7690
Frontal Inf Oper L	0,1258	Parietal Sup R	2,418e-07*	Precentral L	0,7990
Occipital Sup L	0,1570	Amygdala L	2,843e-07*	Postcentral L	0,8191
Frontal Inf Orb L	0,2958	Paracentral Lobule R	3,901e-07*	Frontal Sup Orb R	0,8227
Occipital Inf L	0,3441	Amygdala R	5,595e-07*	Pallidum L	0,8611
Frontal Inf Orb R	0,3918	Heschl R	2,493e-06*	SupraMarginal R	0,8670
Temporal Sup R	0,5114	Lingual R	3,960e-06*	Insula R	0,8711
Frontal Sup L	0,5557	Cingulum Ant R	8,993e-06*	Temporal Pole Sup R	0,8868
Frontal Mid L	0,5865	Temporal Pole Mid L	1,538e-05*	Frontal Inf Oper L	0,9952
Putamen L	0,6693	Cingulum Mid L	4,389e-03	Putamen L	0,9969

In this table brain nodes are ordered for each condition by p-values – from smallest to largest –, based on the PILI differences for the noise protocol between LSD and PCB by perturbing each specific node at a time. All 90 brain regions are shown in order by the size of their p-value. The asterisk indicates statistically significant differences after Bonferroni correction.

Bibliography

At the end of each reference the pages of its appearance in the text are indicated.

- S. Achard, R. Salvador, B. Whitcher, J. Suckling, and E. Bullmore. A resilient, low-frequency, small-world human brain functional network with highly connected association cortical hubs. *The Journal of neuroscience : the official journal of the Society for Neuroscience*, 26(1):63–72, 2006. 40, 92
- H. Aerts, W. Fias, K. Caeyenberghs, and D. Marinazzo. Brain networks under attack: robustness properties and the impact of lesions. *Brain*, 139(12):3063–3083, 2016. 82
- M. T. Alkire and J. Miller. General anesthesia and the neural correlates of consciousness. *Progress in Brain Research*, 150:229–244, 2005. 1, 12
- M. T. Alkire, R. J. Haier, S. J. Barker, N. K. Shah, J. C. Wu, and Y. J. Kao. Cerebral metabolism during propofol anesthesia in humans studied with positron emission tomography. *Anesthesiology*, 82(2):393–403, 1995. 12
- M. T. Alkire, A. G. Hudetz, and G. Tononi. Consciousness and Anesthesia. *Science*, 322(5903):876–880, 2008. 12, 61, 67
- E. A. Allen, E. Damaraju, S. M. Plis, E. B. Erhardt, T. Eichele, and V. D. Calhoun. Tracking whole-brain connectivity dynamics in the resting state. *Cerebral Cortex*, 24(3):663–676, 2014. 58
- P. J. Allen, G. Polizzi, K. Krakow, D. R. Fish, and L. Lemieux. Identification of EEG events in the MR scanner: The problem of pulse artifact and a method for its subtraction. *NeuroImage*, 8(3):229–239, 1998. 37
- F. Amzica and M. Steriade. Electrophysiological correlates of sleep delta waves. *Electroencephalography and Clinical Neurophysiology*, 107(2):69–83, 1998. 62
- A. Arieli, A. Sterkin, A. Grinvald, and A. Aertsen. Dynamics of ongoing activity: Explanation of the large variability in evoked cortical responses. *Science*, 273(5283):1868–1871, 1996. 1
- S. Atasoy, I. Donnelly, and J. Pearson. Human brain networks function in connectome-specific harmonic waves. *Nature Communications*, 7:10340, 2016. 97
- S. Atasoy, G. Deco, M. L. Kringelbach, and J. Pearson. Harmonic Brain Modes: A Uni-

- fying Framework for Linking Space and Time in Brain Dynamics. *The Neuroscientist*, page 107385841772803, 2017a. 115
- S. Atasoy, L. Roseman, M. Kaelen, M. L. Kringelbach, G. Deco, and R. L. Carhart-Harris. Connectome-harmonic decomposition of human brain activity reveals dynamical repertoire re-organization under LSD. *Scientific Reports*, 7(1):17661, 2017b. 2, 90, 108, 111, 119, 122
- D. Attwell and C. Iadecola. The neural basis of functional brain imaging signals. *Trends in Neurosciences*, 25(12):621–625, 2002. 3, 6
- S. Baillet and L. Garnero. A Bayesian approach to introducing anatomo-functional priors in the EEG/MEG inverse problem. *IEEE Transactions on Biomedical Engineering*, 44(5):374–385, 1997. 3
- A. T. Barker, R. Jalinous, and I. L. Freeston. Non-invasive magnetic stimulation of human motor cortex. *The Lancet*, 325(8437):1106–1107, 1985. 28
- A. Barrat, M. Barthelemy, R. Pastor-Satorras, and A. Vespignani. The architecture of complex weighted networks. *Proceedings of the National Academy of Sciences of the United States of America*, 101(11):3747–3752, 2003. 46
- P. Barttfeld, L. Uhrig, J. D. Sitt, M. Sigman, B. Jarraya, and S. Dehaene. Signature of consciousness in the dynamics of resting-state brain activity. *Proceedings of the National Academy of Sciences*, 112(3):887–892, 2015. 1, 12, 13, 35
- P. J. Basser, J. Mattiello, and D. LeBihan. MR diffusion tensor spectroscopy and imaging. *Biophysical Journal*, 66(1):259–267, 1994. 21
- D. S. Bassett, E. Bullmore, B. A. Verchinski, V. S. Mattay, D. R. Weinberger, and A. Meyer-Lindenberg. Hierarchical Organization of Human Cortical Networks in Health and Schizophrenia. *Journal of Neuroscience*, 28(37):9239–9248, 2008. 111, 119
- C. F. Beckmann and S. M. Smith. Probabilistic Independent Component Analysis for Functional Magnetic Resonance Imaging. *IEEE Transactions on Medical Imaging*, 23(2):137–152, 2004. 72
- C. F. Beckmann, M. DeLuca, J. T. Devlin, and S. M. Smith. Investigations into resting-state connectivity using independent component analysis. *Philosophical Transactions of the Royal Society B: Biological Sciences*, 360(1457):1001–1013, 2005. 5
- M. R. Bennett. The prefrontal-limbic network in depression: Modulation by hypothalamus, basal ganglia and midbrain. *Progress in Neurobiology*, 93(4):468–487, 2011. 110, 119
- R. G. Bettinardi, N. Tort-Colet, M. Ruiz-Mejias, M. V. Sanchez-Vives, and G. Deco. Gradual emergence of spontaneous correlated brain activity during fading of general anesthesia in rats: Evidences from fMRI and local field potentials. *NeuroImage*, 114:185–198, 2015. 5
- R. F. Betzel, S. Gu, J. D. Medaglia, F. Pasqualetti, and D. S. Bassett. Optimally controlling the human connectome: The role of network topology. *Scientific Reports*, 6(1):30770, 2016. 85
- B. Biswal, F. Z. Yetkin, V. M. Haughton, and J. S. Hyde. Functional connectivity in the motor cortex of resting human brain using echo-planar MRI. *Magnetic resonance in medicine : official journal of the Society of Magnetic Resonance in Medicine / Society of Magnetic Resonance in Medicine*, 34(4):537–41, 1995. 1, 2, 3, 34, 40, 66, 92
- R. G. Bittar, S. C. Burn, P. G. Bain, S. L. Owen, C. Joint, D. Shlugman, and T. Z. Aziz. Deep brain stimulation for movement disorders and pain. *Journal of Clinical*

- Neuroscience*, 12(4):457–463, 2005. 28
- M. Boly. Measuring the fading consciousness in the human brain. *Current Opinion in Neurology*, 24(4):394–400, 2011. 30
- M. Boly, C. Phillips, L. Tshibanda, A. Vanhaudenhuyse, M. Schabus, T. T. Dang-Vu, G. Moonen, R. Hustinx, P. Maquet, and S. Laureys. Intrinsic brain activity in altered states of consciousness: How conscious is the default mode of brain function? *Annals of the New York Academy of Sciences*, 1129:119–129, 2008. 9, 34, 113
- M. Boly, V. Perlbarg, G. Marrelec, M. Schabus, S. Laureys, J. Doyon, M. Péligrini-Issac, P. Maquet, and H. Benali. Hierarchical clustering of brain activity during human nonrapid eye movement sleep. *Proceedings of the National Academy of Sciences of the United States of America*, 109(15):5856–61, 2012. 1, 8, 9, 34, 69, 71, 113
- V. Bonhomme, P. Boveroux, P. Hans, J. F. Brichant, A. Vanhaudenhuyse, M. Boly, and S. Laureys. Influence of anesthesia on cerebral blood flow, cerebral metabolic rate, and brain functional connectivity. *Current Opinion in Anaesthesiology*, 24(5):474–479, 2011. 12
- P. Boveroux, A. Vanhaudenhuyse, M. A. Bruno, Q. Noirhomme, S. Lauwick, A. Luxen, C. Degueldre, A. Plenevaux, C. Schnakers, C. Phillips, J. F. Brichant, V. Bonhomme, P. Maquet, M. D. Greicius, S. Laureys, and M. Boly. Breakdown of within- and between-network resting state functional magnetic resonance imaging connectivity during propofol-induced loss of consciousness. *Anesthesiology*, 113(5):1038–1053, 2010. 14
- A. R. Braun, T. J. Balkin, N. J. Wesensten, R. E. Carson, M. Varga, P. Baldwin, S. Selbie, G. Belenky, and P. Herscovitch. Regional cerebral blood flow throughout the sleep-wake cycle. An H215O PET study. *Brain*, 120(7):1173–1197, 1997. 8
- M. Breakspear. Dynamic models of large-scale brain activity, 2017. 21, 22
- M. J. Brookes, M. Woolrich, H. Luckhoo, D. Price, J. R. Hale, M. C. Stephenson, G. R. Barnes, S. M. Smith, and P. G. Morris. Investigating the electrophysiological basis of resting state networks using magnetoencephalography. *Proceedings of the National Academy of Sciences*, 108(40):16783–16788, 2011. 1, 2, 3, 4, 5, 113
- R. L. Buckner and D. C. Carroll. Self-projection and the brain. *Trends in Cognitive Sciences*, 11(2):49–57, 2007. 13
- R. L. Buckner, J. R. Andrews-Hanna, and D. L. Schacter. The brain’s default network: Anatomy, function, and relevance to disease. *Annals of the New York Academy of Sciences*, 1124(1):1–38, 2008. 6, 13
- R. L. Buckner, J. Sepulcre, T. Talukdar, F. M. Krienen, H. Liu, T. Hedden, J. R. Andrews-Hanna, R. A. Sperling, and K. A. Johnson. Cortical hubs revealed by intrinsic functional connectivity: mapping, assessment of stability, and relation to Alzheimer’s disease. *The Journal of neuroscience : the official journal of the Society for Neuroscience*, 29(6):1860–73, 2009. 40, 92
- E. Bullmore and O. Sporns. Complex brain networks: Graph theoretical analysis of structural and functional systems. *Nature Reviews Neuroscience*, 10(3):186–198, 2009. 4
- R. Cabeza and L. Nyberg. Imaging Cognition II: An Empirical Review of 275 PET and fMRI Studies. *Journal of Cognitive Neuroscience*, 12(1):1–47, 2000. 2
- R. Cabeza, F. Dolcos, R. Graham, and L. Nyberg. Similarities and differences in the neural correlates of episodic memory retrieval and working memory. *NeuroImage*, 16(2):317–330, 2002. 6

- J. Cabral, E. Hugues, O. Sporns, and G. Deco. Role of local network oscillations in resting-state functional connectivity. *NeuroImage*, 57(1):130–139, 2011. 21, 22, 23
- J. Cabral, E. Hugues, M. L. Kringelbach, and G. Deco. Modeling the outcome of structural disconnection on resting-state functional connectivity. *NeuroImage*, 62(3):1342–1353, 2012. 82
- J. Cabral, M. L. Kringelbach, and G. Deco. Exploring the network dynamics underlying brain activity during rest. *Progress in Neurobiology*, 114:102–131, 2014a. 1, 66
- J. Cabral, H. Luckhoo, M. Woolrich, M. Joensson, H. Mohseni, A. Baker, M. L. Kringelbach, and G. Deco. Exploring mechanisms of spontaneous functional connectivity in MEG: How delayed network interactions lead to structured amplitude envelopes of band-pass filtered oscillations. *NeuroImage*, 90:423–435, 2014b. 21
- J. Cabral, M. L. Kringelbach, and G. Deco. Functional connectivity dynamically evolves on multiple time-scales over a static structural connectome: Models and mechanisms. *NeuroImage*, 160:84–96, 2017. 27, 83
- S. Camalet, F. Jülicher, and J. Prost. Self-Organized Beating and Swimming of Internally Driven Filaments. *Physical Review Letters*, 82(7):1590–1593, 1999. 56, 61
- R. L. Carhart-Harris and G. M. Goodwin. The Therapeutic Potential of Psychedelic Drugs: Past, Present, and Future. *Neuropsychopharmacology*, 42(11):2105–2113, 2017. 111
- R. L. Carhart-Harris, D. Erritzoe, T. Williams, J. M. Stone, L. J. Reed, A. Colasanti, R. J. Tyacke, R. Leech, A. L. Malizia, K. Murphy, P. Hobden, J. Evans, A. Feilding, R. G. Wise, and D. J. Nutt. Neural correlates of the psychedelic state as determined by fMRI studies with psilocybin. *Proceedings of the National Academy of Sciences*, 109(6):2138–2143, 2012. 1, 15, 88, 107, 114
- R. L. Carhart-Harris, R. Leech, D. Erritzoe, T. M. Williams, J. M. Stone, J. Evans, D. J. Sharp, A. Feilding, R. G. Wise, and D. J. Nutt. Functional connectivity measures after psilocybin inform a novel hypothesis of early psychosis. *Schizophrenia Bulletin*, 39(6):1343–1351, 2013. 6, 15, 18, 107
- R. L. Carhart-Harris, R. Leech, P. J. Hellyer, M. Shanahan, A. Feilding, E. Tagliazucchi, D. R. Chialvo, D. Nutt, N. Axmacher, S. J. Brooks, K. Maclean, and J. Hopkins. The entropic brain: a theory of conscious states informed by neuroimaging research with psychedelic drugs. *Frontiers in human neuroscience*, 8:20, 2014. 1, 15, 85, 119, 122
- R. L. Carhart-Harris, M. Kaelen, M. Bolstridge, T. M. Williams, L. T. Williams, R. Underwood, A. Feilding, and D. J. Nutt. The paradoxical psychological effects of lysergic acid diethylamide (LSD). *Psychological Medicine*, 46(7):1379–1390, 2016a. 1, 15, 110
- R. L. Carhart-Harris, S. Muthukumaraswamy, L. Roseman, M. Kaelen, W. Droog, K. Murphy, E. Tagliazucchi, E. E. Schenber, T. Nest, C. Orban, R. Leech, L. T. Williams, T. M. Williams, M. Bolstridge, B. Sessa, J. McGonigle, M. I. Sereno, D. Nichols, P. J. Hellyer, P. Hobden, J. Evans, K. D. Singh, R. G. Wise, H. V. Curran, A. Feilding, and D. J. Nutt. Neural correlates of the LSD experience revealed by multimodal neuroimaging. *Proceedings of the National Academy of Sciences*, 113(17):4853–4858, 2016b. 1, 6, 15, 16, 17, 88, 89, 91, 101, 107, 111, 114, 118
- R. L. Carhart-Harris, L. Roseman, M. Bolstridge, L. Demetriou, J. N. Pannekoek, M. B. Wall, M. Tanner, M. Kaelen, J. McGonigle, K. Murphy, R. Leech, H. V. Curran, and D. J. Nutt. Psilocybin for treatment-resistant depression: FMRI-measured brain mechanisms. *Scientific Reports*, 7(1):13187, 2017. 15, 111

- M. A. Carskadon and W. C. Dement. Normal Human Sleep: An Overview. *Principles and Practice of Sleep Medicine*, pages 13–23, 2005. 7
- A. G. Casali, O. Gosseries, M. Rosanova, M. Boly, S. Sarasso, K. R. Casali, S. Casarotto, M. A. Bruno, S. Laureys, G. Tononi, and M. Massimini. A theoretically based index of consciousness independent of sensory processing and behavior. *Science Translational Medicine*, 5(198):198ra105, 2013. 10, 28, 29, 30, 35, 61, 62, 67, 68, 83, 85, 89, 108, 113, 115, 116, 117
- S. S. Cash, E. Halgren, N. Dehghani, A. O. Rossetti, T. Thesen, C. M. Wang, O. Devinsky, R. Kuzniecky, W. Doyle, J. R. Madsen, E. Bromfield, L. Eross, P. Halász, G. Karmos, R. Csercsa, L. Wittner, and I. Ulbert. The human K-complex represents an isolated cortical down-state. *Science*, 324(5930):1084–1087, 2009. 8
- C. Chang and G. H. Glover. Time-frequency dynamics of resting-state brain connectivity measured with fMRI. *NeuroImage*, 50(1):81–98, 2010. 58
- S. Ching and E. N. Brown. Modeling the dynamical effects of anesthesia on brain circuits. *Current Opinion in Neurobiology*, 25:116–122, 2014. 2
- C. Cirelli and G. Tononi. Is sleep essential? *PLoS Biology*, 6(8):1605–1611, 2008. 7, 34
- J. Clausen. Ethical brain stimulation - neuroethics of deep brain stimulation in research and clinical practice. *European Journal of Neuroscience*, 32(7):1152–1162, 2010. 30, 66, 82, 89
- L. Cocchi, M. V. Sale, A. Lord, A. Zalesky, M. Breakspear, and J. B. Mattingley. Dissociable effects of local inhibitory and excitatory theta-burst stimulation on large-scale brain dynamics. *Journal of Neurophysiology*, 113(9):3375–3385, 2015. 83
- J. Cohen. *Statistical Power Analysis for the Behavioral Sciences*. Routledge, 1988. 97
- M. W. Cole, D. S. Bassett, J. D. Power, T. S. Braver, and S. E. Petersen. Intrinsic and task-evoked network architectures of the human brain. *Neuron*, 83(1):238–251, 2014. 4, 66
- D. L. Collins, P. Neelin, T. M. Peters, and A. C. Evans. Automatic 3D intersubject registration of MR volumetric data in standardized Talairach space. *Journal of Computer Assisted Tomography*, 18(2):192–205, 1994. 39
- J. S. Damoiseaux, S. A. R. B. Rombouts, F. Barkhof, P. Scheltens, C. J. Stam, S. M. Smith, and C. F. Beckmann. Consistent resting-state networks across healthy subjects. *Proceedings of the National Academy of Sciences*, 103(37):13848–13853, 2006. 2, 4, 5, 66, 113
- T. T. Dang-Vu, M. Desseilles, S. Laureys, C. Degueldre, F. Perrin, C. Phillips, P. Maquet, and P. Peigneux. Cerebral correlates of delta waves during non-REM sleep revisited. *NeuroImage*, 28(1):14–21, 2005. 38, 63, 91
- M. De Luca, S. Smith, N. De Stefano, A. Federico, and P. M. Matthews. Blood oxygenation level dependent contrast resting state networks are relevant to functional activity in the neocortical sensorimotor system. *Experimental Brain Research*, 167(4):587–594, 2005. 4
- M. De Luca, C. F. Beckmann, N. De Stefano, P. M. Matthews, and S. M. Smith. fMRI resting state networks define distinct modes of long-distance interactions in the human brain. *NeuroImage*, 29(4):1359–1367, 2006. 4, 5
- F. de Pasquale, S. Della Penna, A. Z. Snyder, C. Lewis, D. Mantini, L. Marzetti, P. Belardinelli, L. Ciancetta, V. Pizzella, G. L. Romani, and M. Corbetta. Temporal dynamics of spontaneous MEG activity in brain networks. *Proceedings of the National Academy*

- of Sciences*, 107(13):6040–6045, 2010. 1, 4
- G. Deco and V. K. Jirsa. Ongoing Cortical Activity at Rest: Criticality, Multistability, and Ghost Attractors. *Journal of Neuroscience*, 32(10):3366–3375, 2012. 21, 22, 116
- G. Deco and M. L. Kringelbach. Great Expectations: Using Whole-Brain Computational Connectomics for Understanding Neuropsychiatric Disorders. *Neuron*, 84(5):892–905, 2014. 85
- G. Deco and M. L. Kringelbach. Metastability and Coherence: Extending the Communication through Coherence Hypothesis Using A Whole-Brain Computational Perspective. *Trends in Neurosciences*, 39(3):125–135, 2016. 35, 42, 60, 66
- G. Deco and M. L. Kringelbach. Hierarchy of Information Processing in the Brain: A Novel 'Intrinsic Ignition' Framework. *Neuron*, 94(5):961–968, 2017. 97, 118
- G. Deco, V. K. Jirsa, P. A. Robinson, M. Breakspear, and K. Friston. The dynamic brain: From spiking neurons to neural masses and cortical fields, 2008. 21
- G. Deco, V. Jirsa, A. R. McIntosh, O. Sporns, and R. Kotter. Key role of coupling, delay, and noise in resting brain fluctuations. *Proceedings of the National Academy of Sciences*, 106(25):10302–10307, 2009. 21, 22, 23
- G. Deco, V. K. Jirsa, and A. R. McIntosh. Emerging concepts for the dynamical organization of resting-state activity in the brain. *Nature Reviews Neuroscience*, 12(1):43–56, 2011. 1, 3, 22, 66, 116
- G. Deco, V. K. Jirsa, and A. R. McIntosh. Resting brains never rest: Computational insights into potential cognitive architectures. *Trends in Neurosciences*, 36(5):268–274, 2013a. 116
- G. Deco, A. Ponce-Alvarez, D. Mantini, G. L. Romani, P. Hagmann, and M. Corbetta. Resting-State Functional Connectivity Emerges from Structurally and Dynamically Shaped Slow Linear Fluctuations. *Journal of Neuroscience*, 33(27):11239–11252, 2013b. 22
- G. Deco, P. Hagmann, A. G. Hudetz, and G. Tononi. Modeling resting-state functional networks when the cortex falls asleep: Local and global changes. *Cerebral Cortex*, 24(12):3180–3194, 2014. 82
- G. Deco, G. Tononi, M. Boly, and M. L. Kringelbach. Rethinking segregation and integration: contributions of whole-brain modelling. *Nature Reviews Neuroscience*, 16(7):430–439, 2015. 76, 77, 80, 83, 94
- G. Deco, J. Cabral, M. W. Woolrich, A. B. Stevner, T. J. van Hartevelt, and M. L. Kringelbach. Single or multiple frequency generators in on-going brain activity: A mechanistic whole-brain model of empirical MEG data. *NeuroImage*, 152:538–550, 2017a. 25, 72, 83, 92
- G. Deco, M. L. Kringelbach, V. K. Jirsa, and P. Ritter. The dynamics of resting fluctuations in the brain: Metastability and its dynamical cortical core. *Scientific Reports*, 7(1):3095, 2017b. 22, 24, 25, 26, 27, 43, 73, 74, 89, 98, 114, 116, 120, 121
- G. Deco, T. J. Van Hartevelt, H. M. Fernandes, A. Stevner, and M. L. Kringelbach. The most relevant human brain regions for functional connectivity: Evidence for a dynamical workspace of binding nodes from whole-brain computational modelling. *NeuroImage*, 146:197–210, 2017c. 82
- G. Deco, J. Cabral, V. M. Saenger, M. Boly, E. Tagliazucchi, H. Laufs, E. Van Someren, B. Jobst, A. Stevner, and M. L. Kringelbach. Perturbation of whole-brain dynamics in silico reveals mechanistic differences between brain states. *NeuroImage*, 169:46–56,

2018. 24, 25, 27, 89, 92, 93, 94, 95, 98, 108, 114, 115, 121, 122
- S. Dehaene and J. P. Changeux. Ongoing spontaneous activity controls access to consciousness: A neuronal model for inattentive blindness. *PLoS Biology*, 3(5):0910–0927, 2005. 59
- S. Dehaene, M. Kerszberg, and J.-P. Changeux. A neuronal model of a global workspace in effortful cognitive tasks. *Proceedings of the National Academy of Sciences*, 95(24):14529–14534, 1998. 12, 59, 67
- S. Dehaene, L. Charles, J. R. King, and S. Marti. Toward a computational theory of conscious processing. *Current Opinion in Neurobiology*, 25:76–84, 2014. 12, 13, 59, 61, 67
- F. Dell’Acqua and M. Catani. Structural human brain networks: Hot topics in diffusion tractography. *Current Opinion in Neurology*, 25(4):375–383, 2012. 21
- B. Desgranges, J. C. Baron, and F. Eustache. The functional neuroanatomy of episodic memory: The role of the frontal lobes, the hippocampal formation, and other areas. *NeuroImage*, 8(2):198–213, 1998. 6
- G. Deshpande, C. Kerssens, P. S. Sebel, and X. Hu. Altered local coherence in the default mode network due to sevoflurane anesthesia. *Brain Research*, 1318:110–121, 2010. 14
- S. G. Disner, C. G. Beevers, E. A. P. Haigh, and A. T. Beck. Neural mechanisms of the cognitive model of depression. *Nature Reviews Neuroscience*, 12(8):467–477, 2011. 112, 119
- R. G. dos Santos, F. L. Osório, J. A. S. Crippa, and J. E. Hallak. Classical hallucinogens and neuroimaging: A systematic review of human studies: Hallucinogens and neuroimaging. *Neuroscience and Biobehavioral Reviews*, 71:715–728, 2016. 14
- G. Doucet, M. Naveau, L. Petit, N. Delcroix, L. Zago, F. Crivello, G. Jobard, N. Tzourio-Mazoyer, B. Mazoyer, E. Mellet, and M. Joliot. Brain activity at rest: a multiscale hierarchical functional organization. *Journal of Neurophysiology*, 105(6):2753–2763, 2011. 119
- S. K. Esser, S. Hill, and G. Tononi. Breakdown of Effective Connectivity During Slow Wave Sleep: Investigating the Mechanism Underlying a Cortical Gate Using Large-Scale Modeling. *Journal of Neurophysiology*, 102(4):2096–2111, 2009. 1
- D. Fernández-Espejo, A. Soddu, D. Cruse, E. M. Palacios, C. Junque, A. Vanhau-den-huyse, E. Rivas, V. Newcombe, D. K. Menon, J. D. Pickard, S. Laureys, and A. M. Owen. A role for the default mode network in the bases of disorders of consciousness. *Annals of Neurology*, 72(3):335–343, 2012. 5, 13
- F. Ferrarelli, M. Massimini, S. Sarasso, A. Casali, B. A. Riedner, G. Angelini, G. Tononi, and R. A. Pearce. Breakdown in cortical effective connectivity during midazolam-induced loss of consciousness. *Proceedings of the National Academy of Sciences*, 107(6):2681–2686, 2010. 10, 28, 29, 61, 67, 68, 83, 108, 113, 115, 116, 117
- P. Fillard, M. Descoteaux, A. Goh, S. Gouttard, B. Jeurissen, J. Malcolm, A. Ramirez-Manzanares, M. Reisert, K. Sakaie, F. Tensaouti, T. Yo, J. F. Mangin, and C. Poupon. Quantitative evaluation of 10 tractography algorithms on a realistic diffusion MR phantom. *NeuroImage*, 56(1):220–234, 2011. 21
- P. Fiset, T. Daloz, G. Plourde, P. Meuret, V. Bonhomme, N. Hajj-ali, S. B. Backman, and A. C. Evans. Brain Mechanisms of Propofol-Induced Loss of Consciousness in Humans: a Positron Emission Tomographic Study. *The Journal of Neuroscience*, 19(13):5506–5513, 1999. 12

- M. D. Fox and M. E. Raichle. Spontaneous fluctuations in brain activity observed with functional magnetic resonance imaging. *Nature reviews. Neuroscience*, 8(9):700–11, 2007. 2, 34
- M. D. Fox, A. Z. Snyder, J. L. Vincent, M. Corbetta, D. C. Van Essen, and M. E. Raichle. The human brain is intrinsically organized into dynamic, anticorrelated functional networks. *Proceedings of the National Academy of Sciences*, 102(27):9673–9678, 2005. 2, 3, 4, 5, 113
- M. D. Fox, R. L. Buckner, H. Liu, M. M. Chakravarty, A. M. Lozano, and A. Pascual-Leone. Resting-state networks link invasive and noninvasive brain stimulation across diverse psychiatric and neurological diseases. *Proceedings of the National Academy of Sciences*, 111(41):E4367–E4375, 2014. 67
- P. Fransson. Spontaneous low-frequency BOLD signal fluctuations: An fMRI investigation of the resting-state default mode of brain function hypothesis. *Human Brain Mapping*, 26(1):15–29, 2005. 5, 34
- F. Freyer, J. A. Roberts, R. Becker, P. A. Robinson, P. Ritter, and M. Breakspear. Biophysical Mechanisms of Multistability in Resting-State Cortical Rhythms. *Journal of Neuroscience*, 31(17):6353–6361, 2011. 24, 25
- F. Freyer, J. A. Roberts, P. Ritter, and M. Breakspear. A Canonical Model of Multistability and Scale-Invariance in Biological Systems. *PLoS Computational Biology*, 8(8): e1002634, 2012. 24, 25
- K. J. Friston, C. D. Frith, P. F. Liddle, and R. S. J. Frackowiak. Functional Connectivity: The Principal-Component Analysis of Large (PET) Data Sets. *Journal of Cerebral Blood Flow & Metabolism*, 13(1):5–14, 1993. 4
- K. J. Friston, P. Fletcher, O. Josephs, A. Holmes, M. D. Rugg, and R. Turner. Event-related fMRI: Characterizing differential responses. *NeuroImage*, 7(1):30–40, 1998. 2
- K. J. Friston, L. Harrison, and W. Penny. Dynamic causal modelling. *NeuroImage*, 19(4):1273–1302, 2003. 61
- A. Ghosh, Y. Rho, A. R. McIntosh, R. Kötter, and V. K. Jirsa. Cortical network dynamics with time delays reveals functional connectivity in the resting brain. *Cognitive Neurodynamics*, 2(2):115–120, 2008. 21
- M. F. Glasser, T. S. Coalson, E. C. Robinson, C. D. Hacker, J. Harwell, E. Yacoub, K. Ugurbil, J. Andersson, C. F. Beckmann, M. Jenkinson, S. M. Smith, and D. C. Van Essen. A multi-modal parcellation of human cerebral cortex. *Nature*, 536(7615): 171–178, 2016. 4
- E. Glerean, J. Salmi, J. M. Lahnakoski, I. P. Jääskeläinen, and M. Sams. Functional magnetic resonance imaging phase synchronization as a measure of dynamic functional connectivity. *Brain connectivity*, 2(2):91–101, 2012. 40, 42, 74, 83, 92
- G. H. Glover, T. Q. Li, and D. Ress. Image-based method for retrospective correction of physiological motion effects in fMRI: RETROICOR. *Magnetic Resonance in Medicine*, 44(1):162–167, 2000. 37
- L. L. Gollo, J. A. Roberts, and L. Cocchi. Mapping how local perturbations influence systems-level brain dynamics. *NeuroImage*, 160:97–112, 2017. 83
- R. Grech, T. Cassar, J. Muscat, K. P. Camilleri, S. G. Fabri, M. Zervakis, P. Xanthopoulos, V. Sakkalis, and B. Vanrumste. Review on solving the inverse problem in EEG source analysis. *Journal of NeuroEngineering and Rehabilitation*, 5(1):25, 2008. 3
- M. D. Greicius, B. Krasnow, A. L. Reiss, and V. Menon. Functional connectivity in the

- resting brain: a network analysis of the default mode hypothesis. *Proceedings of the National Academy of Sciences of the United States of America*, 100(1):253–8, 2003. 2
- M. D. Greicius, V. Kiviniemi, O. Tervonen, V. Vainionpää, S. Alahuhta, A. L. Reiss, and V. Menon. Persistent default-mode network connectivity during light sedation. *Human Brain Mapping*, 29(7):839–847, 2008. 14
- M. D. Greicius, K. Supekar, V. Menon, and R. F. Dougherty. Resting-state functional connectivity reflects structural connectivity in the default mode network. *Cerebral Cortex*, 19(1):72–78, 2009. 2, 3, 34
- L. Grinspoon and J. B. Bakalar. *Psychedelic drugs reconsidered*. Basic Books, New York, 1979. 14, 15
- S. Gu, F. Pasqualetti, M. Cieslak, Q. K. Telesford, A. B. Yu, A. E. Kahn, J. D. Medaglia, J. M. Vettel, M. B. Miller, S. T. Grafton, and D. S. Bassett. Controllability of structural brain networks. *Nature Communications*, 6(1):8414, 2015. 85
- P. Guldenmund, A. Demertzi, P. Boveroux, M. Boly, A. Vanhauzenhuyse, M.-A. Bruno, O. Gosseries, Q. Noirhomme, J.-F. Brichant, V. Bonhomme, S. Laureys, and A. Soddu. Thalamus, Brainstem and Salience Network Connectivity Changes During Propofol-Induced Sedation and Unconsciousness. *Brain Connectivity*, 3(3):273–285, 2013. 14
- L. F. Haas. Hans Berger (1873-1941), Richard Caton (1842-1926), and electroencephalography. *Journal of Neurology, Neurosurgery & Psychiatry*, 74(1):9–9, 2003. 1
- K. A. Hadland, M. F. Rushworth, D. Gaffan, and R. E. Passingham. The effect of cingulate lesions on social behaviour and emotion. *Neuropsychologia*, 41(8):919–931, 2003. 110
- P. Hagmann, L. Jonasson, P. Maeder, J.-P. Thiran, V. J. Wedeen, and R. Meuli. Understanding Diffusion MR Imaging Techniques: From Scalar Diffusion-weighted Imaging to Diffusion Tensor Imaging and Beyond. *RadioGraphics*, 26(suppl.1):S205–S223, 2006. 21
- M. Hallett. Transcranial magnetic stimulation and the human brain. *Nature*, 406(6792):147–150, 2000. 28
- B. J. He. Spontaneous and Task-Evoked Brain Activity Negatively Interact. *Journal of Neuroscience*, 33(11):4672–4682, 2013. 109, 110
- B. J. He, A. Z. Snyder, J. M. Zempel, M. D. Smyth, and M. E. Raichle. Electrophysiological correlates of the brain’s intrinsic large-scale functional architecture. *Proceedings of the National Academy of Sciences*, 105(41):16039–16044, 2008. 59
- S. Hill and G. Tononi. Modeling Sleep and Wakefulness in the Thalamocortical System. *Journal of Neurophysiology*, 93(3):1671–1698, 2005. 1
- T. Hiltunen, J. Kantola, A. Abou Elseoud, P. Lepola, K. Suominen, T. Starck, J. Nikkinen, J. Remes, O. Tervonen, S. Palva, V. Kiviniemi, and J. M. Palva. Infra-Slow EEG Fluctuations Are Correlated with Resting-State Network Dynamics in fMRI. *Journal of Neuroscience*, 34(2):356–362, 2014. 59
- R. Hindriks, M. J. van Putten, and G. Deco. Intra-cortical propagation of EEG alpha oscillations. *NeuroImage*, 103:444–453, 2014. 21
- R. Hindriks, M. H. Adhikari, Y. Murayama, M. Ganzetti, D. Mantini, N. K. Logothetis, and G. Deco. Can sliding-window correlations reveal dynamic functional connectivity in resting-state fMRI? *NeuroImage*, 127:242–256, 2016. 58
- A. Hofmann. *LSD My problem child*. McGraw-Hill, New York, New York, 1980. 15, 88

- C. J. Honey, R. Kötter, M. Breakspear, and O. Sporns. Network structure of cerebral cortex shapes functional connectivity on multiple time scales. *Proceedings of the National Academy of Sciences*, 104(24):10240–10245, 2007. 22
- C. J. Honey, O. Sporns, L. Cammoun, X. Gigandet, J. P. Thiran, R. Meuli, and P. Hagmann. Predicting human resting-state functional connectivity from structural connectivity. *Proceedings of the National Academy of Sciences*, 106(6):2035–2040, 2009. 2, 21, 22, 24
- F. C. Hoppensteadt and E. M. Izhikevich. *Weakly Connected Neural Networks*, volume 126 of *Applied Mathematical Sciences*. Springer New York, New York, NY, 1997. 23
- S. G. Horowitz, A. R. Braun, W. S. Carr, D. Picchioni, T. J. Balkin, M. Fukunaga, and J. H. Duyn. Decoupling of the brain’s default mode network during deep sleep. *Proceedings of the National Academy of Sciences of the United States of America*, 106(27):11376–81, 2009. 1, 6, 8, 9, 34, 58, 113, 115
- R. Huber, H. Mäki, M. Rosanova, S. Casarotto, P. Canali, A. G. Casali, G. Tononi, and M. Massimini. Human cortical excitability increases with time awake. *Cerebral Cortex*, 23(2):332–338, 2013. 62
- A. G. Hudetz. General Anesthesia and Human Brain Connectivity. *Brain Connectivity*, 2(6):291–302, 2012. 12
- R. M. Hutchison, T. Womelsdorf, J. S. Gati, S. Everling, and R. S. Menon. Resting-state networks show dynamic functional connectivity in awake humans and anesthetized macaques. *Human Brain Mapping*, 34(9):2154–2177, 2013. 58
- C. Iber, S. Ancoli-Israel, A. Chesson, and S. Quan. The AASM Manual for the Scoring of Sleep and Associates Events: Rules, Terminology and Technical Specifications. *Sleep (Rochester)*, page 59, 2007. 7, 8, 34, 36, 37, 115
- R. J. Ilmoniemi, J. Virtanen, J. Ruohonen, J. Karhu, H. J. Aronen, R. Näätänen, and T. Katila. Neuronal responses to magnetic stimulation reveal cortical reactivity and connectivity. *NeuroReport*, 8(16):3537–3540, 1997. 67
- K. Jahnke, F. von Wegner, A. Morzelewski, S. Borisov, M. Maischein, H. Steinmetz, and H. Laufs. To wake or not to wake? The two-sided nature of the human K-complex. *NeuroImage*, 59(2):1631–1638, 2012. 37
- M. Jenkinson, P. Bannister, M. Brady, and S. Smith. Improved optimization for the robust and accurate linear registration and motion correction of brain images. *NeuroImage*, 17(2):825–841, 2002. 38, 72
- V. K. Jirsa and J. A. S. Kelso. Spatiotemporal pattern formation in neural systems with heterogeneous connection topologies. *Physical Review E - Statistical Physics, Plasmas, Fluids, and Related Interdisciplinary Topics*, 62(6 B):8462–8465, 2000. 4
- B. M. Jobst, R. Hindriks, H. Laufs, E. Tagliazucchi, G. Hahn, A. Ponce-Alvarez, A. B. Stevner, M. L. Kringelbach, and G. Deco. Increased Stability and Breakdown of Brain Effective Connectivity during Slow-Wave Sleep: Mechanistic Insights from Whole-Brain Computational Modelling. *Scientific Reports*, 7(1):4634, 2017. 24, 25, 27, 68, 72, 73, 75, 79, 82, 84, 89, 92, 98, 114, 122
- S. C. Johnson. Neural correlates of self-reflection. *Brain*, 125(8):1808–1814, 2002. 110
- M. Kaelen, F. S. Barrett, L. Roseman, R. Lorenz, N. Family, M. Bolstridge, H. V. Curran, A. Feilding, D. J. Nutt, and R. L. Carhart-Harris. LSD enhances the emotional response to music. *Psychopharmacology*, 232(19):3607–3614, 2015. 15, 16, 18, 89, 107, 110, 118
- M. Kaelen, L. Roseman, J. Kahan, A. Santos-Ribeiro, C. Orban, R. Lorenz, F. S. Bar-

- rett, M. Bolstridge, T. Williams, L. Williams, M. B. Wall, A. Feilding, S. Muthukumaraswamy, D. J. Nutt, and R. Carhart-Harris. LSD modulates music-induced imagery via changes in parahippocampal connectivity. *European Neuropsychopharmacology*, 26(7):1099–1109, 2016. 15, 16, 89, 107, 118
- C. Kaufmann, R. Wehrle, T. C. Wetter, F. Holsboer, D. P. Auer, T. Pollmächer, and M. Czisch. Brain activation and hypothalamic functional connectivity during human non-rapid eye movement sleep: An EEG/fMRI study. *Brain*, 129(3):655–667, 2005. 8, 34, 58, 115
- S. A. Knock, A. R. McIntosh, O. Sporns, R. Kötter, P. Hagmann, and V. K. Jirsa. The effects of physiologically plausible connectivity structure on local and global dynamics in large scale brain models. *Journal of Neuroscience Methods*, 183(1):86–94, 2009. 22
- W. C. Koller, K. E. Lyons, S. B. Wilkinson, and R. Pahwa. Efficacy of unilateral deep brain stimulation of the VIM nucleus of the thalamus for essential head tremor. *Movement Disorders*, 14(5):847–850, 1999. 28
- P. Krack, A. Batir, N. Van Blercom, S. Chabardes, V. Fraix, C. Ardouin, A. Koudsie, P. D. Limousin, A. Benazzouz, J. F. LeBas, A.-L. Benabid, and P. Pollak. Five-Year Follow-up of Bilateral Stimulation of the Subthalamic Nucleus in Advanced Parkinson's Disease. *New England Journal of Medicine*, 349(20):1925–1934, 2003. 28
- M. L. Kringelbach and T. Z. Aziz. Neuroethical principles of deep-brain stimulation. *World Neurosurgery*, 76(6):518–519, 2011. 30, 66, 82, 89
- M. L. Kringelbach, N. Jenkinson, A. L. Green, S. L. Owen, P. C. Hansen, P. L. Cornelissen, I. E. Holliday, J. Stein, and T. Z. Aziz. Deep brain stimulation for chronic pain investigated with magnetoencephalography. *NeuroReport*, 18(3):223–228, 2007a. 28, 67, 89
- M. L. Kringelbach, N. Jenkinson, S. L. Owen, and T. Z. Aziz. Translational principles of deep brain stimulation. *Nature Reviews Neuroscience*, 8(8):623–635, 2007b. 28, 66
- M. L. Kringelbach, A. L. Green, and T. Z. Aziz. Balancing the Brain: Resting State Networks and Deep Brain Stimulation. *Frontiers in Integrative Neuroscience*, 5:8, 2011. 86
- M. L. Kringelbach, A. R. McIntosh, P. Ritter, V. K. Jirsa, and G. Deco. The Rediscovery of Slowness: Exploring the Timing of Cognition. *Trends in cognitive sciences*, 19(10):616–28, 2015. 25, 74, 98
- Y. Kuramoto. *Chemical Oscillations, Waves, and Turbulence*, volume 19 of *Springer Series in Synergetics*. Springer Berlin Heidelberg, Berlin, Heidelberg, 1984. 23, 42
- Y. A. Kuznetsov. *Elements of Applied Bifurcation Theory*. Springer: New York, 1998. 25
- B. C. Labate and C. Cavnar. The expansion of the field of research on ayahuasca: Some reflections about the ayahuasca track at the 2010 MAPS " Psychedelic Science in the 21st Century" conference. *International Journal of Drug Policy*, 22(2):174–178, 2011. 14
- B. C. Labate and C. Cavnar. *The therapeutic use of Ayahuasca*. Springer Berlin Heidelberg, Berlin, Heidelberg, 2014. 14
- B. C. Labate and H. Jungaberle. *The internationalization of ayahuasca*. Lit, 2011. 14
- L. J. Larson-Prior, J. M. Zempel, T. S. Nolan, F. W. Prior, A. Z. Snyder, and M. E. Raichle. Cortical network functional connectivity in the descent to sleep. *Proceedings of the National Academy of Sciences*, 106(11):4489–4494, 2009. 9, 34, 113

- H. Laufs, K. Krakow, P. Sterzer, E. Eger, A. Beyerle, A. Salek-Haddadi, and A. Kleinschmidt. Electroencephalographic signatures of attentional and cognitive default modes in spontaneous brain activity fluctuations at rest. *Proceedings of the National Academy of Sciences*, 100(19):11053–11058, 2003. 1, 4
- D. Le Bihan and M. Iima. Diffusion magnetic resonance imaging: What water tells us about biological tissues. *PLoS Biology*, 13(7):e1002203, 2015. 21
- M. H. Lee, C. D. Hacker, A. Z. Snyder, M. Corbetta, D. Zhang, E. C. Leuthardt, and J. S. Shimony. Clustering of resting state networks. *PLoS ONE*, 7(7):e40370, 2012. 34
- D. Léger, E. Debellemanniere, A. Rabat, V. Bayon, K. Benchenane, and M. Chennaoui. Slow-wave sleep: From the cell to the clinic. *Sleep Medicine Reviews*, 2018. 7, 8
- J. Lei, E. Tagliazucchi, V. Brodbeck, C. Kell, and H. Laufs. Haemodynamic correlates of fronto-central EEG delta and sigma power during slow wave sleep. *Clinical Neurophysiology*, 125:S279–S280, 2014. 63
- D. A. Leopold, Y. Murayama, and N. K. Logothetis. Very slow activity fluctuations in monkey visual cortex: Implications for functional brain imaging. *Cerebral Cortex*, 13(4):422–433, 2003. 1
- S. Little, A. Pogosyan, S. Neal, B. Zavala, L. Zrinzo, M. Hariz, T. Foltynie, P. Limousin, K. Ashkan, J. FitzGerald, A. L. Green, T. Z. Aziz, and P. Brown. Adaptive deep brain stimulation in advanced Parkinson disease. *Annals of Neurology*, 74(3):449–457, 2013. 28
- V. Litvak, S. Komssi, M. Scherg, K. Hoehstetter, J. Classen, M. Zaaroor, H. Pratt, and S. Kahkonen. Artifact correction and source analysis of early electroencephalographic responses evoked by transcranial magnetic stimulation over primary motor cortex. *NeuroImage*, 37(1):56–70, 2007. 28, 29, 67, 89
- X. Liu, K. K. Lauer, B. D. Ward, S. M. Rao, S. J. Li, and A. G. Hudetz. Propofol disrupts functional interactions between sensory and high-order processing of auditory verbal memory. *Human Brain Mapping*, 33(10):2487–2498, 2012. 14
- N. K. Logothetis, J. Pauls, M. Augath, T. Trinath, and A. Oeltermann. Neurophysiological investigation of the basis of the fMRI signal. *Nature*, 412(6843):150–157, 2001. 3, 6
- L.-D. Lord, A. B. Stevner, G. Deco, and M. L. Kringelbach. Understanding principles of integration and segregation using whole-brain computational connectomics: implications for neuropsychiatric disorders. *Philosophical Transactions of the Royal Society A: Mathematical, Physical and Engineering Sciences*, 375(2096):20160283, 2017. 76, 80
- H. Lu, Q. Zou, H. Gu, M. E. Raichle, E. A. Stein, and Y. Yang. Rat brains also have a default mode network. *Proceedings of the National Academy of Sciences*, 109(10):3979–3984, 2012. 5, 6
- J. Q. M. Ly, G. Gaggioni, S. L. Chellappa, S. Papachilleos, A. Brzozowski, C. Borsu, M. Rosanova, S. Sarasso, B. Middleton, A. Luxen, S. N. Archer, C. Phillips, D.-J. Dijk, P. Maquet, M. Massimini, and G. Vandewalle. Circadian regulation of human cortical excitability. *Nature Communications*, 7:11828, 2016. 62
- E. A. Maguire and C. J. Mummery. Differential modulation of a common memory retrieval network revealed by positron emission tomography. *Hippocampus*, 9(1):54–61, 1999. 6
- D. Mantini, M. G. Perrucci, C. Del Gratta, G. L. Romani, and M. Corbetta. Electrophysiological signatures of resting state networks in the human brain. *Proceedings of*

- the National Academy of Sciences of the United States of America*, 104(32):13170–5, 2007. 2, 3, 4, 5, 113
- S. Marchand, R. C. Kupers, M. C. Bushnell, and G. H. Duncan. Analgesic and placebo effects of thalamic stimulation. *Pain*, 105(3):481–488, 2003. 28
- M. F. Mason, M. I. Norton, J. D. Van Horn, D. M. Wegner, S. T. Grafton, and C. N. Macrae. Wandering minds: The default network and stimulus-independent thought. *Science*, 315(5810):393–395, 2007. 5
- M. Massimini, F. Ferrarelli, R. Huber, S. K. Esser, H. Singh, and G. Tononi. Breakdown of cortical effective connectivity during sleep. *Science*, 309(5744):2228–2232, 2005. 10, 28, 29, 35, 61, 67, 83, 89, 108, 113, 115, 116, 117
- M. Massimini, F. Ferrarelli, S. K. Esser, B. A. Riedner, R. Huber, M. Murphy, M. J. Peterson, and G. Tononi. Triggering sleep slow waves by transcranial magnetic stimulation. *Proceedings of the National Academy of Sciences*, 104(20):8496–8501, 2007. 10, 35
- M. Massimini, M. Boly, A. Casali, M. Rosanova, and G. Tononi. A perturbational approach for evaluating the brain’s capacity for consciousness. *Progress in Brain Research*, 177(C):201–214, 2009. 10, 28, 29, 35, 61, 113
- H. S. Mayberg, A. M. Lozano, V. Voon, H. E. McNeely, D. Seminowicz, C. Hamani, J. M. Schwab, and S. H. Kennedy. Deep brain stimulation for treatment-resistant depression. *Neuron*, 45(5):651–660, 2005. 28
- D. McKenna and J. Riba. New World Tryptamine Hallucinogens and the Neuroscience of Ayahuasca. In *Current topics in behavioral neurosciences*, pages 1–29. Springer, Berlin, Heidelberg, 2016. 14
- C. Meisel, A. Klaus, C. Kuehn, and D. Plenz. Critical Slowing Down Governs the Transition to Neuron Spiking. *PLoS Computational Biology*, 11(2):e1004097, 2015. 117
- A. Messé, D. Rudrauf, H. Benali, and G. Marrelec. Relating Structure and Function in the Human Brain: Relative Contributions of Anatomy, Stationary Dynamics, and Non-stationarities. *PLoS Computational Biology*, 10(3):e1003530, 2014. 45
- D. Meunier, R. Lambiotte, and E. T. Bullmore. Modular and hierarchically modular organization of brain networks. *Frontiers in Neuroscience*, 4(DEC):200, 2010. 119
- H. R. Mohseni, P. P. Smith, C. E. Parsons, K. S. Young, J. A. Hyam, A. Stein, J. F. Stein, A. L. Green, T. Z. Aziz, and M. L. Kringelbach. MEG can map short and long-term changes in brain activity following deep brain stimulation for chronic pain. *PLoS ONE*, 7(6):e37993, 2012. 28, 67, 89
- B. Molaee-Ardekani, L. Senhadji, M. B. Shamsollahi, B. Vosoughi-Vahdat, and E. Wodey. Brain activity modeling in general anesthesia: Enhancing local mean-field models using a slow adaptive firing rate. *Physical Review E - Statistical, Nonlinear, and Soft Matter Physics*, 76(4):041911, 2007. 1
- P. Moretti and M. A. Muñoz. Griffiths phases and the stretching of criticality in brain networks. *Nature Communications*, 4:2521, 2013. 111, 119
- P. J. Morgane, J. R. Galler, and D. J. Mokler. A review of systems and networks of the limbic forebrain/limbic midbrain. *Progress in Neurobiology*, 75(2):143–160, 2005. 110
- S. Mori and P. C. M. van Zijl. Fiber tracking: principles and strategies - a technical review. *NMR in Biomedicine*, 15(7-8):468–480, 2002. 21
- M. N. Moussa, M. R. Steen, P. J. Laurienti, and S. Hayasaka. Consistency of Network

- Modules in Resting-State fMRI Connectome Data. *PLoS ONE*, 7(8):e44428, 2012. 5
- S. F. Muldoon, F. Pasqualetti, S. Gu, M. Cieslak, S. T. Grafton, J. M. Vettel, and D. S. Bassett. Stimulation-Based Control of Dynamic Brain Networks. *PLoS Computational Biology*, 12(9):e1005076, 2016. 85
- F. Müller, C. Lenz, P. Dolder, U. Lang, A. Schmidt, M. Liechti, and S. Borgwardt. Increased thalamic resting-state connectivity as a core driver of LSD-induced hallucinations. *Acta Psychiatrica Scandinavica*, 136(6):648–657, 2017. 107
- S. D. Muthukumaraswamy, R. L. Carhart-Harris, R. J. Moran, M. J. Brookes, T. M. Williams, D. Erntzoe, B. Sessa, A. Papadopoulos, M. Bolstridge, K. D. Singh, A. Feilding, K. J. Friston, and D. J. Nutt. Broadband Cortical Desynchronization Underlies the Human Psychedelic State. *Journal of Neuroscience*, 33(38):15171–15183, 2013. 15, 88, 114
- T. T. Nakagawa, M. Woolrich, H. Luckhoo, M. Joensson, H. Mohseni, M. L. Kringelbach, V. Jirsa, and G. Deco. How delays matter in an oscillatory whole-brain spiking-neuron network model for MEG alpha-rhythms at rest. *NeuroImage*, 87:383–394, 2014. 21
- D. E. Nichols. Psychedelics. *Pharmacological Reviews*, 68(2):264–355, 2016. 88
- Y. Nir, R. J. Staba, T. Andrillon, V. V. Vyazovskiy, C. Cirelli, I. Fried, and G. Tononi. Regional Slow Waves and Spindles in Human Sleep. *Neuron*, 70(1):153–169, 2011. 59
- L. Nobili, L. De Gennaro, P. Proserpio, F. Moroni, S. Sarasso, A. Pigorini, F. De Carli, and M. Ferrara. Local aspects of sleep: observations from intracerebral recordings in humans. *Progress in brain research*, 199:219–32, 2012. 8
- E. A. Nofzinger, D. J. Buysse, J. M. Miewald, C. C. Meltzer, J. C. Price, R. C. Sembrat, H. Ombao, C. F. Reynolds, T. H. Monk, M. Hall, D. J. Kupfer, and R. Y. Moore. Human regional cerebral glucose metabolism during non-rapid eye movement sleep in relation to waking. *Brain : a journal of neurology*, 125(Pt 5):1105–1115, 2002. 8
- G. Northoff, A. Heinzl, M. de Greck, F. Bermpohl, H. Dobrowolny, and J. Panksepp. Self-referential processing in our brain - A meta-analysis of imaging studies on the self. *NeuroImage*, 31(1):440–457, 2006. 110
- W. W. Orrison. *Atlas of brain function*. Thieme, 2008. 110
- S. L. Owen, A. L. Green, J. F. Stein, and T. Z. Aziz. Deep brain stimulation for the alleviation of post-stroke neuropathic pain. *Pain*, 120(1-2):202–206, 2006. 28
- F. Palhano-Fontes, K. C. Andrade, L. F. Tofoli, A. C. Jose, A. S. Crippa, J. E. Hallak, S. Ribeiro, and D. B. De Araujo. The psychedelic state induced by Ayahuasca modulates the activity and connectivity of the Default Mode Network. *PLoS ONE*, 10(2):e0118143, 2015. 88, 107, 114
- M. Pandya, M. Altinay, D. A. Malone, and A. Anand. Where in the brain is depression? *Current Psychiatry Reports*, 14(6):634–642, 2012. 110, 119
- T. Passie, J. H. Halpern, D. O. Stichtenoth, H. M. Emrich, and A. Hintzen. The pharmacology of lysergic acid diethylamide: A review. *CNS Neuroscience and Therapeutics*, 14(4):295–314, 2008. 15, 88
- E. Pereda, A. Gamundi, R. Rial, and J. González. Non-linear behaviour of human EEG: Fractal exponent versus correlation dimension in awake and sleep stages. *Neuroscience Letters*, 250(2):91–94, 1998. 67, 82
- A. Pikovsky, M. Rosenblum, and J. Kurths. *Synchronization: A Universal Concept in Nonlinear Sciences*. Cambridge University Press, Cambridge, 2003. 23

- A. Ponce-Alvarez, G. Deco, P. Hagmann, G. L. Romani, D. Mantini, and M. Corbetta. Resting-state temporal synchronization networks emerge from connectivity topology and heterogeneity. *PLoS computational biology*, 11(2):e1004100, 2015a. 23, 58, 74
- A. Ponce-Alvarez, B. J. He, P. Hagmann, and G. Deco. Task-Driven Activity Reduces the Cortical Activity Space of the Brain: Experiment and Whole-Brain Modeling. *PLoS Computational Biology*, 11(8):e1004445, 2015b. 109, 110
- N. Pradhan and P. Sadasivan. The nature of dominant lyapunov exponent and attractor dimension curves of eeg in sleep. *Computers in Biology and Medicine*, 26(5):419–428, 1996. 67
- K. H. Preller, M. Herdener, T. Pokorny, A. Planzer, R. Kraehenmann, P. Stämpfli, M. E. Liechti, E. Seifritz, and F. X. Vollenweider. The Fabric of Meaning and Subjective Effects in LSD-Induced States Depend on Serotonin 2A Receptor Activation. *Current Biology*, 27(3):451–457, 2017a. 15, 18, 88, 89, 107, 110, 114, 118
- K. H. Preller, C. Schleifer, P. Stämpfli, J. Krystal, F. Vollenweider, and A. Anticevic. 951. Changes in Resting-State Global Brain Connectivity in LSD-Induced Altered States of Consciousness are Attributable to the 5-HT_{2A} Receptor. *Biological Psychiatry*, 81(10):S385, 2017b. 15, 88, 114
- P. Qin and G. Northoff. How is our self related to midline regions and the default-mode network? *NeuroImage*, 57(3):1221–1233, 2011. 6
- M. E. Raichle. A brief history of human brain mapping. *Trends in Neurosciences*, 32(2):118–126, 2009a. 66
- M. E. Raichle. A Paradigm Shift in Functional Brain Imaging. *The Journal of Neuroscience*, 29(41):12729–12734, 2009b. 3
- M. E. Raichle. The Restless Brain. *Brain Connectivity*, 1(1):3–12, 2011. 5, 7
- M. E. Raichle. The Brain's Default Mode Network. *Annual Review of Neuroscience*, 38(1):433–447, 2015. 5
- M. E. Raichle, A. M. MacLeod, A. Z. Snyder, W. J. Powers, D. A. Gusnard, and G. L. Shulman. A default mode of brain function. *Proceedings of the National Academy of Sciences*, 98(2):676–682, 2001. 1, 2, 3, 5, 66, 113
- V. RajMohan and E. Mohandas. The limbic system. *Indian Journal of Psychiatry*, 49(2):132, 2007. 110
- G. Rees, K. Friston, and C. Koch. A direct quantitative relationship between the functional properties of human and macaque V5. *Nature Neuroscience*, 3(7):716–723, 2000. 3, 6
- S. Rehncrona, B. Johnels, H. Widner, A. L. Törnqvist, M. Hariz, and O. Sydow. Long-term efficacy of thalamic deep brain stimulation for tremor: Double-blind assessments. *Movement Disorders*, 18(2):163–170, 2003. 28
- J. Rissman, A. Gazzaley, and M. D'Esposito. Measuring functional connectivity during distinct stages of a cognitive task. *NeuroImage*, 23(2):752–763, 2004. 66
- J. A. Roberts, A. Perry, G. Roberts, P. B. Mitchell, and M. Breakspear. Consistency-based thresholding of the human connectome. *NeuroImage*, 145:118–129, 2017. 39, 124
- M. Rosanova, O. Gosseries, S. Casarotto, M. Boly, A. G. Casali, M. A. Bruno, M. Mariotti, P. Boveroux, G. Tononi, S. Laureys, and M. Massimini. Recovery of cortical effective connectivity and recovery of consciousness in vegetative patients. *Brain*, 135(4):1308–

- 1320, 2012. 68
- L. Roseman, R. Leech, A. Feilding, D. J. Nutt, and R. L. Carhart-Harris. The effects of psilocybin and MDMA on between-network resting state functional connectivity in healthy volunteers. *Frontiers in Human Neuroscience*, 8:204, 2014. 15, 107
- M. Rubinov and O. Sporns. Complex network measures of brain connectivity: Uses and interpretations. *NeuroImage*, 52(3):1059–1069, 2010. 4
- J. Ruohonen and R. J. Ilmoniemi. Modelling of the stimulating field generation in TMS. *Electroencephalogr Clin Neurophysiol Suppl*, 51:30–40, 1999. 29
- V. M. Saenger, J. Kahan, T. Foltynie, K. Friston, T. Z. Aziz, A. L. Green, T. J. Van Hartevelt, J. Cabral, A. B. Stevner, H. M. Fernandes, L. Mancini, J. Thornton, T. Yousry, P. Limousin, L. Zrinzo, M. Hariz, P. Marques, N. Sousa, M. L. Kringelbach, and G. Deco. Uncovering the underlying mechanisms and whole-brain dynamics of deep brain stimulation for Parkinson’s disease. *Scientific Reports*, 7(1):9882, 2017. 24, 25, 28, 67, 86, 89, 114
- P. G. Sämann, R. Wehrle, D. Hoehn, V. I. Spoormaker, H. Peters, C. Tully, F. Holsboer, and M. Czisch. Development of the brain’s default mode network from wakefulness to slow wave sleep. *Cerebral Cortex*, 21(9):2082–93, 2011. 1, 6, 8, 9, 34, 58, 59, 113, 115
- T. E. Schlaepfer, M. X. Cohen, C. Frick, M. Kosel, D. Brodessa, N. Axmacher, A. Y. Joe, M. Kreft, D. Lenartz, and V. Sturm. Deep brain stimulation to reward circuitry alleviates anhedonia in refractory major depression. *Neuropsychopharmacology*, 33(2):368–377, 2008. 28
- F. Schneider, F. Bermpohl, A. Heinzl, M. Rotte, M. Walter, C. Tempelmann, C. Wiebking, H. Dobrowolny, H. J. Heinze, and G. Northoff. The resting brain and our self: Self-relatedness modulates resting state neural activity in cortical midline structures. *Neuroscience*, 157(1):120–131, 2008. 110
- M. L. Schölvinck, A. Maier, F. Q. Ye, J. H. Duyn, and D. A. Leopold. Neural basis of global resting-state fMRI activity. *Proceedings of the National Academy of Sciences*, 107(22):10238–10243, 2010. 3, 6
- R. E. Schultes, A. Hofmann, and C. Rättsch. *Plants of the Gods: Their Sacred, Healing, and Hallucinogenic Powers*. Rochester: Healing Arts Press, 1992. 14
- H. G. Schuster and P. Wagner. A model for neuronal oscillations in the visual cortex - 2. Phase description of the feature dependent synchronization. *Biological Cybernetics*, 64(1):83–85, 1990. 23
- A. K. Seth, Z. Dienes, A. Cleeremans, M. Overgaard, and L. Pessoa. Measuring consciousness: relating behavioural and neurophysiological approaches. *Trends in Cognitive Sciences*, 12(8):314–321, 2008. 30
- M. Shanahan. Metastable chimera states in community-structured oscillator networks. *Chaos*, 20(1):013108, 2010. 42
- A. Shmuel and D. A. Leopold. Neuronal correlates of spontaneous fluctuations in fMRI signals in monkey visual cortex: Implications for functional connectivity at rest. *Human Brain Mapping*, 29(7):751–761, 2008. 3, 6
- H. R. Siebner, T. O. Bergmann, S. Bestmann, M. Massimini, H. Johansen-Berg, H. Mochizuki, D. E. Bohning, E. D. Boorman, S. Groppa, C. Miniussi, A. Pascual-Leone, R. Huber, P. C. Taylor, R. J. Ilmoniemi, L. De Gennaro, A. P. Strafella, S. Kähkönen, S. Klöppel, G. B. Frisoni, M. S. George, M. Hallett, S. A. Brandt, M. F. Rushworth, U. Ziemann, J. C. Rothwell, N. Ward, L. G. Cohen, J. Baudewig, T. Paus,

- Y. Ugawa, and P. M. Rossini. Consensus paper: Combining transcranial stimulation with neuroimaging. *Brain Stimulation*, 2(2):58–80, 2009. 30, 66, 89
- S. M. Smith. Fast robust automated brain extraction. *Human Brain Mapping*, 17(3):143–155, 2002. 72
- S. M. Smith, P. T. Fox, K. L. Miller, D. C. Glahn, P. M. Fox, C. E. Mackay, N. Filippini, K. E. Watkins, R. Toro, A. R. Laird, and C. F. Beckmann. Correspondence of the brain’s functional architecture during activation and rest. *Proceedings of the National Academy of Sciences*, 106(31):13040–13045, 2009. 66
- S. M. Smith, K. L. Miller, S. Moeller, J. Xu, E. J. Auerbach, M. W. Woolrich, C. F. Beckmann, M. Jenkinson, J. Andersson, M. F. Glasser, D. C. Van Essen, D. A. Feinberg, E. S. Yacoub, and K. Ugurbil. Temporally-independent functional modes of spontaneous brain activity. *Proceedings of the National Academy of Sciences*, 109(8):3131–3136, 2012. 34
- G. Solovey, L. M. Alonso, T. Yanagawa, N. Fujii, M. O. Magnasco, G. A. Cecchi, and A. Proekt. Loss of Consciousness Is Associated with Stabilization of Cortical Activity. *Journal of Neuroscience*, 35(30):10866–10877, 2015. 62
- A. Spiegler, E. C. A. Hansen, C. Bernard, A. R. McIntosh, and V. K. Jirsa. Selective Activation of Resting-State Networks following Focal Stimulation in a Connectome-Based Network Model of the Human Brain. *eNeuro*, 3(5), 2016. 83
- V. I. Spoormaker, M. S. Schroter, P. M. Gleiser, K. C. Andrade, M. Dresler, R. Wehrle, P. G. Samann, and M. Czisch. Development of a Large-Scale Functional Brain Network during Human Non-Rapid Eye Movement Sleep. *Journal of Neuroscience*, 30(34):11379–11387, 2010. 34, 59
- V. I. Spoormaker, P. M. Gleiser, and M. Czisch. Frontoparietal Connectivity and Hierarchical Structure of the Brain’s Functional Network during Sleep. *Frontiers in Neurology*, 3:80, 2012. 8, 34, 115
- O. Sporns. Theoretical Neuroanatomy: Relating Anatomical and Functional Connectivity in Graphs and Cortical Connection Matrices. *Cerebral Cortex*, 10(2):127–141, 2000. 4, 119
- O. Sporns. Network attributes for segregation and integration in the human brain. *Current Opinion in Neurobiology*, 23(2):162–171, 2013. 4
- O. Sporns, D. R. Chialvo, M. Kaiser, and C. C. Hilgetag. Organization, development and function of complex brain networks. *Trends in Cognitive Sciences*, 8(9):418–425, 2004. 4
- R. N. Spreng and C. L. Grady. Patterns of Brain Activity Supporting Autobiographical Memory, Propection, and Theory of Mind, and Their Relationship to the Default Mode Network. *Journal of Cognitive Neuroscience*, 22(6):1112–1123, 2010. 6, 13
- C. J. Stam. Nonlinear dynamical analysis of EEG and MEG: Review of an emerging field. *Clinical Neurophysiology*, 116(10):2266–2301, 2005. 67
- K. E. Stephan and K. J. Friston. Analyzing effective connectivity with fMRI. *Wiley interdisciplinary reviews. Cognitive science*, 1(3):446–459, 2010. 61
- M. Steriade and F. Amzica. Slow sleep oscillation, rhythmic K-complexes, and their paroxysmal developments. *Journal of sleep research*, 7 Suppl 1:30–35, 1998. 8
- S. H. Strogatz. From Kuramoto to Crawford: exploring the onset of synchronization in populations of coupled oscillators. *Physica D: Nonlinear Phenomena*, 143(1-4):1–20, 2000. 23

- E. Tagliazucchi and H. Laufs. Decoding Wakefulness Levels from Typical fMRI Resting-State Data Reveals Reliable Drifts between Wakefulness and Sleep. *Neuron*, 82(3):695–708, 2014. 1, 8, 9, 59
- E. Tagliazucchi and E. J. van Someren. The large-scale functional connectivity correlates of consciousness and arousal during the healthy and pathological human sleep cycle. *NeuroImage*, 160:55–72, 2017. 10, 11
- E. Tagliazucchi, F. von Wegner, A. Morzelewski, S. Borisov, K. Jahnke, and H. Laufs. Automatic sleep staging using fMRI functional connectivity data. *NeuroImage*, 63(1):63–72, 2012a. 1, 8, 34, 37, 59, 69, 115
- E. Tagliazucchi, F. von Wegner, A. Morzelewski, V. Brodbeck, and H. Laufs. Dynamic BOLD functional connectivity in humans and its electrophysiological correlates. *Frontiers in Human Neuroscience*, 6:339, 2012b. 58
- E. Tagliazucchi, F. von Wegner, A. Morzelewski, V. Brodbeck, K. Jahnke, and H. Laufs. Breakdown of long-range temporal dependence in default mode and attention networks during deep sleep. *Proceedings of the National Academy of Sciences*, 110(38):15419–15424, 2013. 6, 9, 34, 37, 113
- E. Tagliazucchi, R. Carhart-Harris, R. Leech, D. Nutt, and D. R. Chialvo. Enhanced repertoire of brain dynamical states during the psychedelic experience. *Human Brain Mapping*, 35(11):5442–5456, 2014. 1, 6, 15, 18, 20, 88, 89, 107, 108, 114
- E. Tagliazucchi, D. R. Chialvo, M. Siniatchkin, E. Amico, J.-F. Brichant, V. Bonhomme, Q. Noirhomme, H. Laufs, and S. Laureys. Large-scale signatures of unconsciousness are consistent with a departure from critical dynamics. *Journal of The Royal Society Interface*, 13(114):20151027, 2016a. 62, 115
- E. Tagliazucchi, N. Crossley, E. T. Bullmore, and H. Laufs. Deep sleep divides the cortex into opposite modes of anatomical-functional coupling. *Brain Structure and Function*, 221(8):4221–4234, 2016b. 8, 10, 35, 58
- E. Tagliazucchi, L. Roseman, M. Kaelen, C. Orban, S. D. Muthukumaraswamy, K. Murphy, H. Laufs, R. Leech, J. McGonigle, N. Crossley, E. Bullmore, T. Williams, M. Bolstridge, A. Feilding, D. J. Nutt, and R. Carhart-Harris. Increased Global Functional Connectivity Correlates with LSD-Induced Ego Dissolution. *Current Biology*, 26(8):1043–1050, 2016c. 1, 15, 16, 18, 19, 88, 90, 107, 109, 111, 114, 118
- A. Thielscher and T. Kammer. Linking physics with physiology in TMS: A sphere field model to determine the cortical stimulation site in TMS. *NeuroImage*, 17(3):1117–1130, 2002. 29
- B. T. Thomas Yeo, F. M. Krienen, J. Sepulcre, M. R. Sabuncu, D. Lashkari, M. Hollinshead, J. L. Roffman, J. W. Smoller, L. Zollei, J. R. Polimeni, B. Fischl, H. Liu, and R. L. Buckner. The organization of the human cerebral cortex estimated by intrinsic functional connectivity. *Journal of Neurophysiology*, 106(3):1125–1165, 2011. 95, 97
- G. Tononi. An information integration theory of consciousness. *BMC Neuroscience*, 5(1):42, 2004. 30, 62
- G. Tononi. Integrated information theory of consciousness: an updated account. *Archives italiennes de biologie*, 150(4):293–329, 2012. 10, 61, 113
- G. Tononi and O. Sporns. Measuring information integration. *BMC Neuroscience*, 4(1):31, 2003. 61
- G. Tononi, O. Sporns, and G. M. Edelman. Reentry and the problem of integrating mul-

- multiple cortical areas: Simulation of dynamic integration in the visual system. *Cerebral Cortex*, 2(4):310–335, 1992. 4
- G. Tononi, O. Sporns, and G. M. Edelman. A measure for brain complexity: relating functional segregation and integration in the nervous system. *Proceedings of the National Academy of Sciences*, 91(11):5033–5037, 1994. 4
- G. Tononi, G. M. Edelman, and O. Sporns. Complexity and coherency: Integrating information in the brain. *Trends in Cognitive Sciences*, 2(12):474–484, 1998. 12, 67
- N. Tzourio-Mazoyer, B. Landeau, D. Papathanassiou, F. Crivello, O. Etard, N. Delcroix, B. Mazoyer, and M. Joliot. Automated anatomical labeling of activations in SPM using a macroscopic anatomical parcellation of the MNI MRI single-subject brain. *NeuroImage*, 15(1):273–289, 2002. 38, 39, 72
- M. P. Van Den Heuvel, R. C. Mandl, R. S. Kahn, and H. E. Hulshoff Pol. Functionally linked resting-state networks reflect the underlying structural connectivity architecture of the human brain. *Human Brain Mapping*, 30(10):3127–3141, 2009. 2, 4, 113
- E. H. van Nes and M. Scheffer. Slow Recovery from Perturbations as a Generic Indicator of a Nearby Catastrophic Shift. *The American Naturalist*, 169(6):738–747, 2007. 68, 82, 117
- F. Váša, M. Shanahan, P. J. Hellyer, G. Scott, J. Cabral, and R. Leech. Effects of lesions on synchrony and metastability in cortical networks. *NeuroImage*, 118:456–467, 2015. 82
- R. A. Veselis, V. A. Feshchenko, R. A. Reinsel, A. M. Dnistrian, B. Beattie, and T. J. Akhurst. Thiopental and propofol affect different regions of the brain at similar pharmacologic effects. *Anesthesia and analgesia*, 99(2):399–408, table of contents, 2004. 12
- M. Vidailhet, L. Vercueil, J.-L. Houeto, P. Krystkowiak, A.-L. Benabid, P. Cornu, C. Lagrange, S. Tézenas du Montcel, D. Dormont, S. Grand, S. Blond, O. Detante, B. Pillon, C. Ardouin, Y. Agid, A. Destée, and P. Pollak. Bilateral Deep-Brain Stimulation of the Globus Pallidus in Primary Generalized Dystonia. *New England Journal of Medicine*, 352(5):459–467, 2005. 28
- J. L. Vincent, G. H. Patel, M. D. Fox, A. Z. Snyder, J. T. Baker, D. C. Van Essen, J. M. Zempel, L. H. Snyder, M. Corbetta, and M. E. Raichle. Intrinsic functional architecture in the anaesthetized monkey brain. *Nature*, 447(7140):83–86, 2007. 1, 5, 12, 13
- V. J. Wedeen, P. Hagmann, W. Y. I. Tseng, T. G. Reese, and R. M. Weisskoff. Mapping complex tissue architecture with diffusion spectrum magnetic resonance imaging. *Magnetic Resonance in Medicine*, 54(6):1377–1386, 2005. 21
- E. F. Wijdicks. The Diagnosis of Brain Death. *New England Journal of Medicine*, 344(16):1215–1221, 2001. 12
- H. R. Wilson and J. D. Cowan. Excitatory and Inhibitory Interactions in Localized Populations of Model Neurons. *Biophysical Journal*, 12(1):1–24, 1972. 23
- H. R. Wilson and J. D. Cowan. A mathematical theory of the functional dynamics of cortical and thalamic nervous tissue. *Kybernetik*, 13(2):55–80, 1973. 23
- C. Wissel. A universal law of the characteristic return time near thresholds. *Oecologia*, 65(1):101–107, 1984. 68, 82, 117
- C. H. Wolters, L. Grasedyck, and W. Hackbusch. Efficient computation of lead field bases and influence matrix for the FEM-based EEG and MEG inverse problem. *Inverse*

- Problems*, 20(4):1099–1116, 2004. 3
- T. Yarkoni, R. A. Poldrack, T. E. Nichols, D. C. Van Essen, and T. D. Wager. Large-scale automated synthesis of human functional neuroimaging data. *Nature Methods*, 8(8): 665–670, 2011. 66
- H. Zepelin and A. Rechtschaffen. Mammalian sleep, longevity, and energy metabolism. *Brain, Behavior and Evolution*, 10(6):425–470, 1974. 8
- D. Zhang and M. E. Raichle. Disease and the brain’s dark energy. *Nature Reviews Neurology*, 6(1):15–28, 2010. 66
- J. Zhang, J. Wang, Q. Wu, W. Kuang, X. Huang, Y. He, and Q. Gong. Disrupted brain connectivity networks in drug-naive, first-episode major depressive disorder. *Biological Psychiatry*, 70(4):334–342, 2011. 111, 119
- C. Zhou, L. Zemanová, G. Zamora, C. C. Hilgetag, and J. Kurths. Hierarchical organization unveiled by functional connectivity in complex brain networks. *Physical Review Letters*, 97(23):238103, 2006. 119
-
-
-
-